

**3-DIMENSIONAL GEOMECHANICAL MODELING OF A TIGHT GAS
RESERVOIR, RULISON FIELD, PICEANCE BASIN, COLORADO**

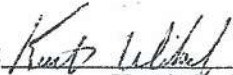
by

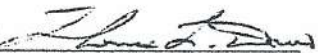
Kurtis R. Wikel

A thesis submitted to the Faculty and Board of Trustees of the Colorado School of Mines in partial fulfillment of the requirements for the degree of Master of Science (Geophysics).

Golden, Colorado

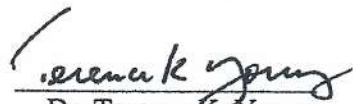
Date 3/7/2008

Signed: 
Kurtis R. Wikel

Approved: 
Dr. Thomas L. Davis
Thesis Advisor

Golden, Colorado

Date March 7, 2008


Dr. Terence K. Young
Department Head
Department of Geophysics

ABSTRACT

An integrated 3-dimensional geomechanical model of a tight gas reservoir at Rulison Field, Colorado has been built to identify and monitor depleted zones. I have used the predictive geomechanical model to compare production and effective stress change with time-lapse seismic. Numerous well data sets including one new zonal pressure test were used to extract information about pore pressures, effective stress magnitudes, relative permeabilities, and levels of depletion. These data sets and pressure tests were used to calibrate my 3-D model with well constrained reservoir properties. A 3-dimensional geomechanical simulation was constructed from a geostatistical model of reservoir properties; this geostatistical model is then used for production modeling of a section of the reservoir. This procedure uses a partially coupled simulator to solve for effective stress change with production over time. The results are then analyzed with time-lapse shear wave data shot in 2003, 2004, and 2006. These results are correlated to seismic data and can be used for better well completions to produce ‘bypassed’ pay and avoid using high cost fracturing into already depleted/producing zones.

Results of the study show a strong correlation between slow shear (S22) time-lapse seismic and modeled areas of pressure and effective stress change. This allows us to show that there are areas of well communication, and completion practices can be optimized to reduce completions into depleted zones and instead drill (or complete) other ‘untapped’ areas through the integration of time-lapse seismic. This work can be used to extract more gas economically from this resource.

TABLE OF CONTENTS

ABSTRACT.....	iii
LIST OF FIGURES	vii
LIST OF TABLES	xv
ACKNOWLEDGEMENTS.....	xvi
CHAPTER 1: GEOLOGY AND STRESS HISTORY.....	1
1.1 Introduction.....	1
1.2 Rulison Introduction	1
1.3 Geologic History.....	3
1.4 Stress History of Rulison	8
1.5 Objectives	11
CHAPTER 2: MINI-FRACTURE TESTING AND ANALYSIS.....	13
2.1 RCP Data Set	13
2.2 Mini-fracture Test Introduction	15
2.3 Mini-fracture Basics.....	15
2.5 Mini Fracture Results.....	22
CHAPTER 3: GEOMECHANICAL MODEL INPUTS	29
3.1 Introduction.....	29
3.2 Previous and Contributing Work	29
3.3 Geostatistical Modeling	32
3.4 Production Modeling	34
CHAPTER 4: GEOMECHANICAL MODELING	39
4.1 Introduction.....	39

4.2 Explanation of Earth Stresses	39
4.3 Workflow	41
4.4 Inputs and Boundary Conditions	43
4.4.1 Soil effective weight	44
4.4.2 Maximum Horizontal Stress Coefficient	45
4.4.3 Minimum Horizontal Stress Coefficient.....	46
4.4.4 Inputs.....	48
4.5 Pressure Related to Effective Stress	49
4.5.1 Stress Equations.....	50
CHAPTER 5: MODELING RESULTS.....	52
5.1 Introduction.....	52
5.2 Well Chronology.....	52
5.3 Results.....	55
5.3.1 Graphical Representation.....	55
5.3.2 3-Dimensional Representation.....	60
5.3.3 2003-2004 Pressure and Effective Stress Change	66
5.3.4 2003-2006 Pressure and Effective Stress Changes	68
5.4 Geomechanical Modeling Compared to Shear Seismic.....	73
5.5 Well Placement.....	80
5.6 Gamma Comparison	81
5.7 Sensitivity Analysis	86
5.8 Conclusions.....	92
CHAPTER 6: RECOMMENDATIONS AND FUTURE WORK.....	94

6.1 Introduction.....	94
6.2 Recommendations.....	94
6.2 Future Work.....	95
REFERENCES	97
APPENDIX A.....	101
APPENDIX B.....	107

LIST OF FIGURES

Figure 1.1: Map showing the location of Rulison field with respect to Rifle and local roads. Image has been modified from Rumon, 2006.	2
Figure 1.2: Location of the RCP and DOE surveys with respect to I-70 and the MWX site within Rulison field. Image has been modified from Keighley, 2006.	2
Figure 1.3: Tectonic map of the Piceance basin, approximate location of Rulison is outlined in red. From Tremain and Tyler, 1997.....	4
Figure 1.4: Generalized stratigraphic section (Cole and Cumella, 2003). Modified by Keighley, 2006.....	5
Figure 1.5: An idealized cross section of the Piceance basin showing the location of Rulison field and the Williams Fork production interval. This also shows the proximity to the Grand Hogback monocline which is responsible for the eastern uplift of the Piceance. From Cumella and Ostby, 2003.....	6
Figure 1.6: Pore pressure gradient as a function of depth from the MWX site. This is indicative of the pressure gradient at Rulison field due to the MWX proximity to the field (approx. 4 miles away). Modified from Rojas, 2005.....	7
Figure 1.7: Location of MWX DOE site with respect to Rifle, CO. Modified from Higgins, 2006.....	8
Figure 1.8: Burial history from MWX site which is analogous to the burial history at Rulison field. Figure is from Lorenz and Finley, 1991.....	9
Figure 1.9: Left side shows stress field from regional view showing generalized stresses for the Rockies. The rose diagram to the right is from image logs taken from a well within the RCP study area at Rulison field. This shows maximum horizontal stress direction. Modified from Higgins, 2006.	10
Figure 2.1: Location of RCP and 1996 DOE survey areas. Also included are locations of specialized well logs and VSP's.....	14
Figure 2.2: Diagram showing location of earlier pressure tests to the location of well RU-5/and RU-6 (two wells from one pad) within the RCP study area. Black dots denote the locations of previous pressure tests that were completed by Williams.	14
Figure 2.3: Generalized diagram of a mini-fracture test. From Higgins, 2006.	16

Figure 2.4: Generalized diagram of a mini-fracture. σ_H denotes maximum horizontal stress direction while σ_h denotes minimum horizontal stress direction. σ_c is closure stress as stated above.....	16
Figure 2.5: Generalized G-function plot (leakoff mechanism one in table one) showing Pressure vs. G(time), G-function (Gdp/dG vs. G(time)) and dp/dG vs. G(time). This is for normal leakoff into the the formation. Departure from the tangent line denotes fracture closure (shown by dashed line 1). From Barree et. al., 2007.....	18
Figure 2.6: Generalized G-function plot showing pressure dependent leak off (denoted by leakoff mechanism two in table one). The characteristic ‘hump’ denotes pressure dependent leakoff (PDL). From Barree et. al., 2007.....	19
Figure 2.7: Generalized G-function plot showing height recession (denoted by leakoff mechanism three in table one). This is shown by the characteristic ‘belly’ of GdP/dG vs. G(time). From Barree et. al., 2007.....	20
Figure 2.8: G-function plot for zone MV-1 showing normal leakoff mechanism. Analysis performed by Halliburton.	21
Figure 2.9: G-function plot for zone MV-5 showing storage caused by natural fractures. Analysis performed by Halliburton.	21
Figure 2.10: G-function plot for zone MV-4 showing height recession caused by unrestricted fracture growth out of zone. Analysis performed by Halliburton.....	22
Figure 2.11: Figure highlighting shear wave splitting phenomenon. Note parallel shear wave (S11) is faster than perpendicular shear wave (S22). From Martin and Davis, 1987.	24
Figure 2.12: Chart showing results of mini-fracture test in RU-5 with the overburden..	25
Figure 2.13: Chart showing pore pressure along with the virgin pore pressure gradient from Williams. The blue window is 8% error that was calculated by Williams. The red window shows partial depletion while the red dashed line denotes 25% depletion. Red dots denote RU-5 while black dots are all other pressure data available in the field.....	25
Figure 2.14: Chart showing pore pressure along with the virgin pore pressure gradient from Williams. The blue window is 8% error that was calculated by Williams. The red window shows partial depletion while the red dashed line denotes 25% depletion.....	26

Figure 2.15: Figure showing pore pressure in RU-5 with the 2003-2004 slow shear (S22) impedance change. Also shown is well RU-6 which is from the same pad and is one (or the only) source of well communication. At these depths these wells are ~200 ft. apart.....	27
Figure 3.1: Stress profile for well 542-20 that shows results of the modeling. From Higgins, 2006.....	31
Figure 3.2: Image log rose diagrams for a well in the RCP study area for depths of 4000 to 7950 feet. In the left image the yellow shows the direction of natural fractures. In the right image the yellow shows the direction of drilling induced fractures (maximum horizontal stress). From Higgins, 2006.	30
Figure 3.3: Figure showing water saturation for geostatistical model in reservoir interval of high fold seismic area. From Casey, 2006.....	33
Figure 3.4: Map showing location of the production/geomechanical model and the wells included within the models.	37
Figure 3.5: Figure showing the scale used for the production/geomechanical models. The property shown is Young's modulus which denotes lithology. Green and higher is sandstone, while the lower values (blues) are shales or sandy shales.	37
Figure 3.6: Figure showing impact of geomechanics on production. The red line shows the simulation without including the geomechanical model. The green line shows the 3-dimensional geomechanics included in the simulation. This chart applies to model. Courtesy Schlumberger DCS.....	38
Figure 4.1: Figure showing 3-dimensional stress state in an infinitely small cube.	40
Figure 4.2: Complete stress tensor showing two notations	41
Figure 4.3: Rotated stress tensor that shows zero shear stresses and only principle components.	41
Figure 4.4: Equation combining two cells porosity in to one. This equation was used as the basis for upscaling the production and therefore, the geomechanical model.	42
Figure 4.5: Figure showing integration of overburden. The density log was not run to the surface; therefore a linear extrapolation was used.....	45
Figure 4.6: Chart showing boundary conditions as input into the mechanical modeling program.....	46
Figure 4.7: Figure showing convention of horizontal stress azimuth and vertical inclination. From VisGen manual.....	48

Figure 5.1: Location of wells with respect to geomechanical model inside high fold seismic area. Red outer box is the RCP survey site. Green X in NE corner of mechanical model is location of data in model compared to RU-5 mini-fracture test.	53
Figure 5.2: Chart highlighting average pressure within the production model with drilling events and time-lapse seismic surveys. The y-axis shows pressure in psia and the x-axis shows the date. Courtesy of Schlumberger DCS Denver.....	54
Figure 5.3: Chart showing stress distribution at well RU-1 in 1981. The stress profile at this time is the initial distribution which is a product of the boundary conditions.	55
Figure 5.4: Pore Pressure and effective stress change through time at 5900 ft. depth at well RU-1. Please note that these are effective stresses, which is why pore pressure is higher than min. horiz. stress in 1981.....	56
Figure 5.5: Pore pressure and effective stress change through time at 6200 ft. depth at well RU-1. Please note that these are effective stresses, which is why pore pressure is higher than min. horiz. stress in 1981.....	56
Figure 5.6: Pore pressure and effective stress change through time at 6500 ft. depth at well RU-1. Please note that these are effective stresses, which is why pore pressure is higher than min. horiz. stress in 1981.....	57
Figure 5.7: Model pressure with depth showing results from mini fracture tests in well RU-5.....	57
Figure 5.8: Model minimum horizontal stress vs. mini fracture tests at RU-5.....	58
Figure 5.9: Chart showing micro-seismic events at well RU-5. This well was also pressure tested before fracturing (Ch.2). It can be seen that micro-seismic events terminate at the interpreted fault (black lines and arrows). This fault system could also cause some of the anomalously high stress values seen in the mini-fracture results at the same depth (fig. 5.8). Figure from Riley, 2007.	60
Figure 5.10: 3-dimensional representation of geomechanical model showing Young's modulus distribution. This is a lithology discriminant, 4.048 e+006 psi and above is sandstones, and below is shales and transition zone (shaly sands).	61
Figure 5.11: Absolute pore pressure in 1981 for entire model. This is a product of the linear gradient used to model pressure.....	62
Figure 5.12: Absolute pore pressure in 2003 for entire model.	62

Figure 5.13: Absolute pore pressure in 2004 for entire model. Please note the far field depletion at depth.....	63
Figure 5.14: Absolute pore pressure in 2006 for entire model. Note location of new wells	63
Figure 5.15: Absolute effective stress in 1981 for entire model. This is a product of boundary conditions as described in Ch.2.	64
Figure 5.16: Absolute effective stress in 2003 for entire model.....	64
Figure 5.17: Absolute effective stress in 2004 for entire model.....	65
Figure 5.18: Absolute effective stress in 2006 for entire model. Note location of new wells and associated stress change.....	65
Figure 5.19: Pressure change from 03-04 compared to the effective overburden stress (σ_v) change at 5900ft. depth in the reservoir. Note the visual similarity and scale.	66
Figure 5.20: Pressure change from 03-04 compared to the effective overburden stress (σ_v) change at 6200ft. depth in the reservoir. Note the visual similarity and scale.	67
Figure 5.21: Pressure change from 03-04 compared to the effective overburden stress (σ_v) change at 6500ft. depth in the reservoir. Note the visual similarity and scale.	67
Figure 5.22: 2003-2006 minimum horizontal effective stress change compared to 03-06 pressure change. Note the direction of the stress anomaly and the direction of input horizontal stress (98 degrees east of north). This is also impacted by lithology and modified permeabilities from modeled hydraulic fractures. Also note stress change from coupling and not pressure change at RU-4	69
Figure 5.23: Maximum horizontal effective stress change from 2003-2006 compared to pressure change from 03-06. Note higher magnitude due to larger pressure changes and direction perpendicular to min.	69
Figure 5.24: Overburden effective stress change from 2003-2006 compared to pressure change from 03-06. Note Pressure change is absent from RU-4 yet present in overburden change. This could be a product of coupling and depletion from above and below not explained by simplified equations shown here.	70
Figure 5.25: Figure showing drainage ellipse concept, this figure is specific to Rulison's minimum horizontal stress direction. This concept is highlighted by the minimum horizontal stress change in all three intervals from 2003-2006. From Higgins, 2006.....	71

Figure 5.26: Figure showing the modeled difference in maximum horizontal stress direction change. On the left is the modeled present day maximum horizontal stress direction (98 degrees) while on the right is the model using the direction of rotated shear seismic, which is 135 east of north or N45W.....	74
Figure 5.27: Pressure compared to slow shear (S22) impedance change from 2003-2006 at 5900 ft. depth. Note no pressure change around well RU-4. This problem could be from scale issues between seismic and the model.	74
Figure 5.28: Effective overburden stress change from 2003-2006 compared to slow shear (S22) impedance change at 5900 ft. depth. Note overburden change with no pressure change at RU-4.	75
Figure 5.29: Effective minimum horizontal stress change from 2003-2006 compared to slow shear (S22) impedance change at 5900 ft. depth. Note effective stress change with no pressure change at RU-4. This is probably due to coupling from above and below.	75
Figure 5.30: Effective maximum horizontal stress change from 2003-2006 compared to slow shear (S22) impedance change at 5900 ft. depth. Note no effective stress change at well RU-4.....	76
Figure 5.31: Pressure compared to slow shear (S22) impedance change from 2003-2006 at 6500 ft. depth.	76
Figure 5.32: Effective overburden stress change from 2003-2006 compared to slow shear (S22) impedance change at 6500 ft. depth.....	77
Figure 5.33: Effective minimum horizontal stress change from 2003-2006 compared to slow shear (S22) impedance change at 6500 ft. depth.....	77
Figure 5.34: Effective maximum horizontal stress change from 2003-2006 compared to slow shear (S22) impedance change at 6500 ft. depth.....	78
Figure 5.35: Cross-section view showing extent of far-field depletion from RU-1. At this point in time RU-1 had been producing for almost 25 years, this was the month before two new wells were drilled only 1000 ft. away at depth.	80
Figure 5.36: Conceptual model of zonal fracturing where all zones have same pore pressure and minimum horizontal stress and are being fractured simultaneously.	83
Figure 5.37: Conceptual model where zone 2 is partially depleted and is causing a larger fracture in the depleted zone. P_{p2} and $\sigma_{h2} < P_{p1}$ and σ_{h1}	84

Figure 5.38: Conceptual model where a greatly depleted zone is diverting zonal hydraulic fracture and leaving virgin zones un-stimulated. P_p2 and $\sigma_{h2} \ll P_p1$ and σ_{h1}	84
Figure 5.39: It can be seen that only when P_p is increased does the circle move toward failure (σ_1 and σ_3 maintain relative distance on x axis as total stress is not changing). Then, after hydraulic fracturing, effective stress is increasing due to lower P_p from production.	91
Figure 6.1: Model production response over time with two scenarios. Red line indicates production without considering geomechanics. While green line shows production with mechanical change over time. Courtesy Schlumberger DCS Denver.	95
Figure A.1: Pressure compared to minimum horizontal effective stress change for 2003-2006 at 6200 ft. depth. Note direction of effective stress change.	101
Figure A.2: Pressure compared to maximum horizontal effective stress change for 2003-2006 at 6200 ft. depth. Note direction is perpendicular to minimum horizontal effective stress change.	102
Figure A.3: Pressure compared to minimum horizontal effective stress change for 2003-2006 at 6500 ft. depth. Note direction of effective stress change.	102
Figure A.4: Pressure compared to maximum horizontal effective stress change for 2003-2006 at 6500 ft. depth. Note direction is perpendicular to minimum horizontal effective stress change.	103
Figure A.5: Pressure compared to minimum horizontal effective stress change for 2003-2006 at 6200 ft. depth. Note direction of stress change.	104
Figure A.6: Pressure compared to maximum horizontal effective stress change for 2003-2006 at 6200 ft. depth. Note direction is perpendicular to minimum horizontal effective stress change.	104
Figure A.7: Pressure compared to overburden effective stress change for 2003-2006 at 6200 ft. depth.	105
Figure A.8: Pressure compared to minimum horizontal effective stress change for 2003-2006 at 6580 ft. depth. Note direction of effective stress change.	105
Figure A.9: Pressure compared to maximum horizontal effective stress change for 2003-2006 at 6580 ft. depth. Note direction is perpendicular to minimum horizontal effective stress change.	106
Figure A.10: Pressure compared to overburden effective stress change for 2003-2006 at 6580 ft. depth.	106

Figure B.1: Pressure change compared to S22 impedance change from 2003-2004 at 5900 ft. depth. Note low percentage changes in seismic data (~2%). Seismic is from Rumon, 2006.....	107
Figure B.2: Overburden stress change compared to S22 seismic impedance change from 2003-2004 at 5900 ft. depth. Seismic is from Rumon, 2006.	108
Figure B.3: Pressure change compared to S22 seismic impedance change from 2003-2004 at 6580 ft. depth. Seismic is from Rumon, 2006.	108
Figure B.4: Overburden stress change compared to S22 seismic impedance change from 2003-2004 at 6580 ft. depth. Seismic is from Rumon, 2006.	109

LIST OF TABLES

Table 2.1: Table showing results from pressure test and related analysis from well RU-5.	17
Table 4.1: Table showing inputs for mechanical modeling and their sources.....	47
Table 5.1: Table showing Gamma calculations from geomechanical modeling.....	82
Table 5.2: Inputs into geomechanical software.....	86

ACKNOWLEDGEMENTS

This work was fully supported and funded by the Reservoir Characterization Project (RCP) at the Colorado School of Mines. First, I must thank and acknowledge Dr. Tom Davis and all of the RCP sponsors, staff, students (past and present), and my committee. Obviously, without their support and assistance, this work would not have been possible. I need to thank Tom Davis for everything he has done for me, including but not limited to all that Canadian wisdom. I also need to acknowledge Tom Bratton, Shannon Higgins, and David Ogbe of Schlumberger DCS Denver. Without their patience, support, insight, friendship, and sense of humor this work would never had been possible. In addition, I would like to thank Mike Batzle for putting up with me constantly trespassing in his lab and Dr. Jennifer Miskimins for her insight and assistance.

I would also like to thank the rest of the Department of Geophysics as they have made my time at CSM both fulfilling and enlightening in many ways. I am leaving with a strong geophysical background and broader view of the world in general from my time here. Also, I would like to thank Matthew Casey for guiding me in statistics and our many conversations about geophysics late into the night.

Finally, and most importantly, I need to thank my family (especially my sister) and my fiancé, Brittany, for constantly being there for me and not letting me forget that there is a life outside of school. I have become a better person during graduate school and that is due in large part to Brittany, my family, and their unfailing patience with me and CSM.

CHAPTER 1

GEOLOGY AND STRESS HISTORY

1.1 Introduction

Previous work at Rulison field has shown that geomechanics can be a powerful tool in reservoir characterization and development (Higgins, 2006). A one dimensional geomechanical model has previously been built for four wells to understand the stress distribution in the subsurface. In addition to this work, there has been a wealth of seismic work completed at Rulison field in the past three years. Analysis has shown that due to the hard rock environment at Rulison, time-lapse response in seismic data is from pressure drawdown and effective stress changes due to production (Ch. 2). A 3-dimensional geomechanical model has been created, using past work and new data, to better understand this complex stress distribution within the RCP study area and how it is affected by production. This model is then compared to time-lapse seismic data in an attempt to validate the results of earlier tests and to gain a better understanding of controls on seismic signature change.

1.2 Rulison Introduction

Rulison field lies in western Colorado in the eastern portion of the Piceance basin near the town of Rifle (fig. 1.1 and 1.2). The Piceance basin has historically contained a high potential for natural gas production from its unconventional tight gas reservoirs. Estimates for recoverable reserves from the Piceance are nearing 10 trillion cubic feet (TCF) (Colorado Interstate Gas, 2006). This figure is substantially higher than the gas that has actually been produced from the basin so far, which highlights the need for further study to tap into unrecovered reserves. Rulison field and the RCP study area is an example of how this is being implemented.

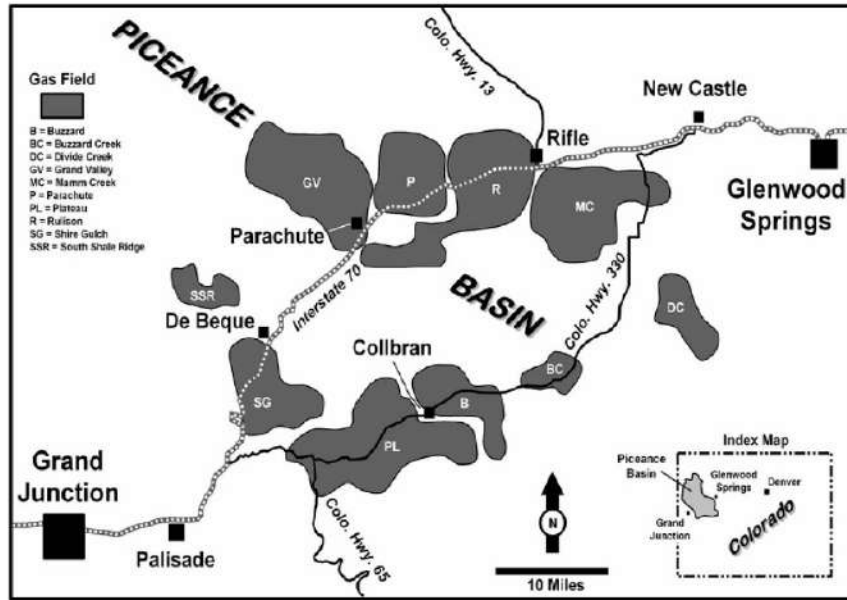


Figure 1.1: Map showing the location of Rulison field with respect to Rifle and local roads. Image has been modified from Rumon, 2006.

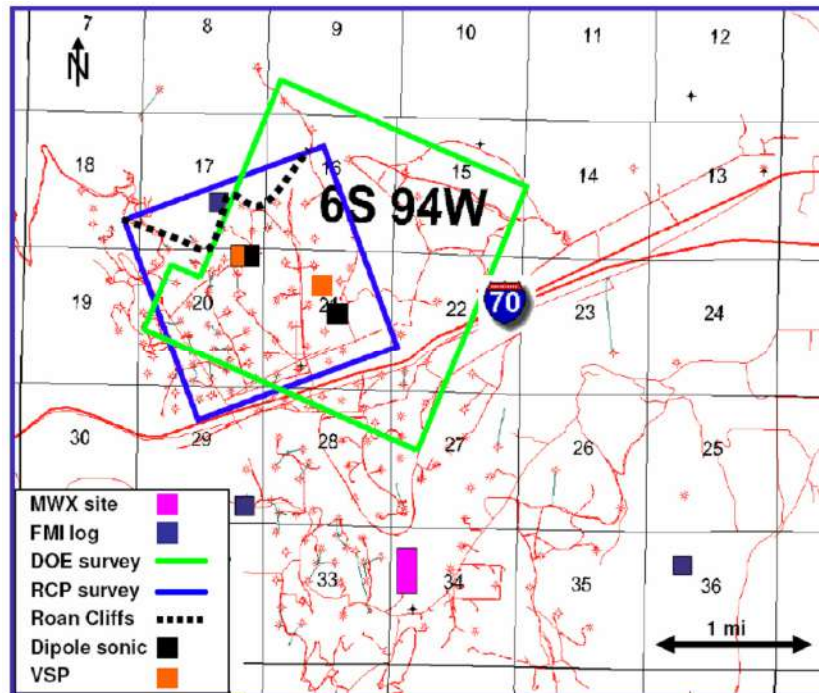


Figure 1.2: Location of the RCP and DOE surveys with respect to I-70 and the MWX site within Rulison field. Image has been modified from Keighley, 2006.

Within the Piceance basin, Rulison field is estimated to contain several TCF of reserves (Kuuskra and Ammer, 2004). The field is approximately 100mi.² and production is mainly from the Williams fork formation from over 550 wells. Williams Production Company is the field operator covering the RCP survey. The producing sandstones are from 1700-2400 ft. thick and are characterized by porosities from 6-12%, microdarcy permeabilities, and irreducible water saturations from 40-65% (Cumella and Ostby, 2003). Rulison is considered an unconventional tight gas field.

Discovered in the 1960's, Rulison's production environment has caused the field to be developed mostly from the early 1980's forward, due to advancements in completion techniques and increases in market gas prices. The field contains laterally discontinuous sandstones where there is little initial well communication even with 10 acre well spacing. These geologic constraints have led to an aggressive completion campaign for every well drilled to increase gas flow and production. Completions are done in every well in this area and it is imperative to not complete into zones that have already been partially depleted by other wells. This research is an attempt to solve that problem through an understanding of stress fields and paths in Rulison field.

1.3 Geologic History

The geologic history of Rulison field starts with the Mesa Verde Groups' deposition in the Piceance basin during the Laramide orogeny from the Late Cretaceous until the Paleocene (McFall et. al., 1986). The Piceance basin is a Rocky Mountain foreland basin that has gently dipping western and southwestern flanks and a sharply upturned eastern flank (Tremain and Tyler, 1997). The basin is bounded in the east by the Grand Hogback which separates the Piceance from the White River uplift.

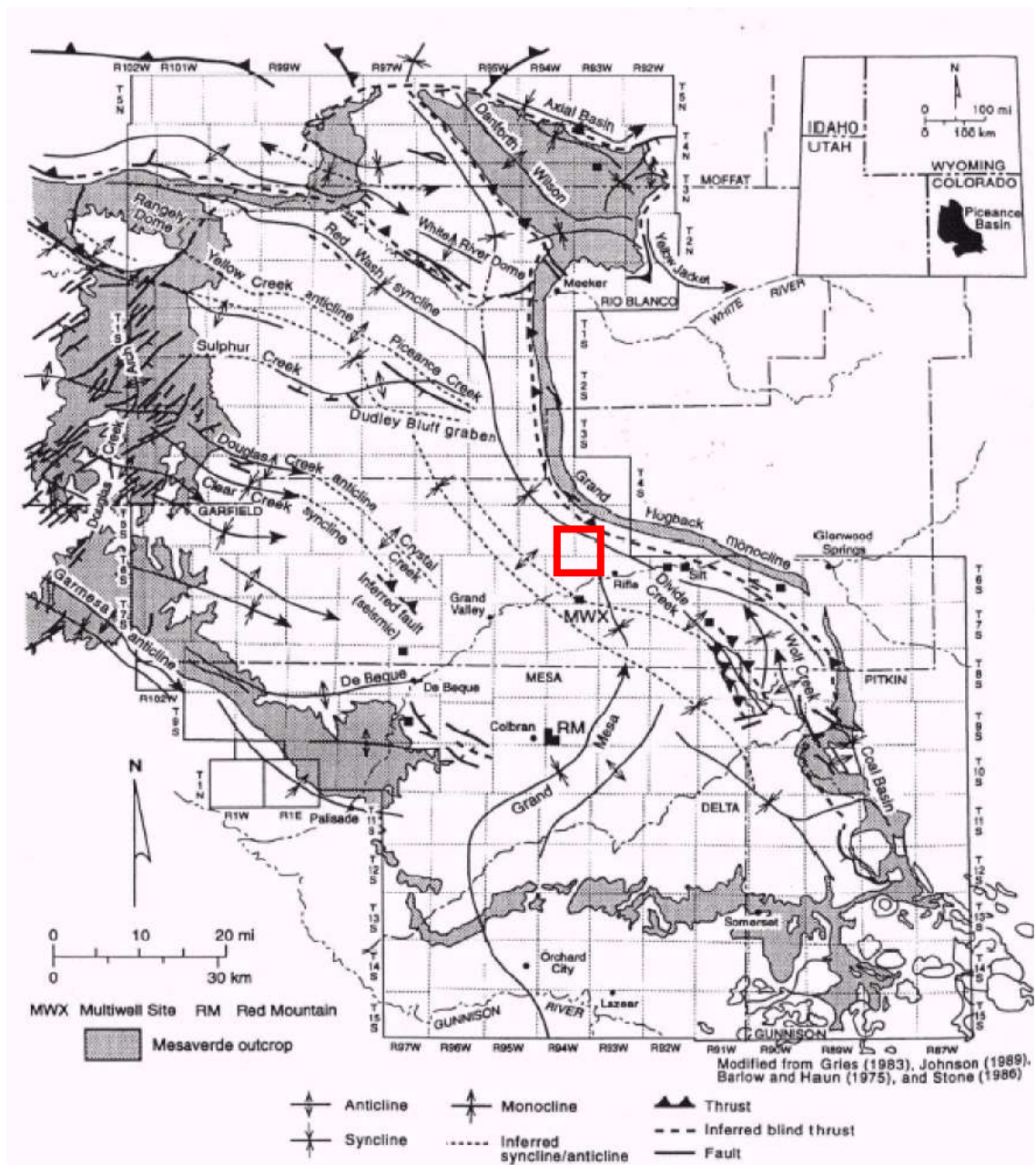


Figure 1.3: Tectonic map of the Piceance basin, approximate location of Rulison is outlined in red. From Tremain and Tyler, 1997.

To the west, the Piceance is separated from the Uinta basin by the Douglas Creek arch (fig. 1.3).

Within the basin itself, the intervals of interest to this work are the main gas bearing zones from the Mesaverde group of Late Cretaceous age (figure 1.4). The Mancos Shale underlies the Mesaverde Group which is regionally a laterally continuous deposit that was deposited in the Cretaceous seaway of the basin (Cumella and Ostby, 2003). The Mesaverde Group is split into two distinct formations: the Iles and the Williams Fork.

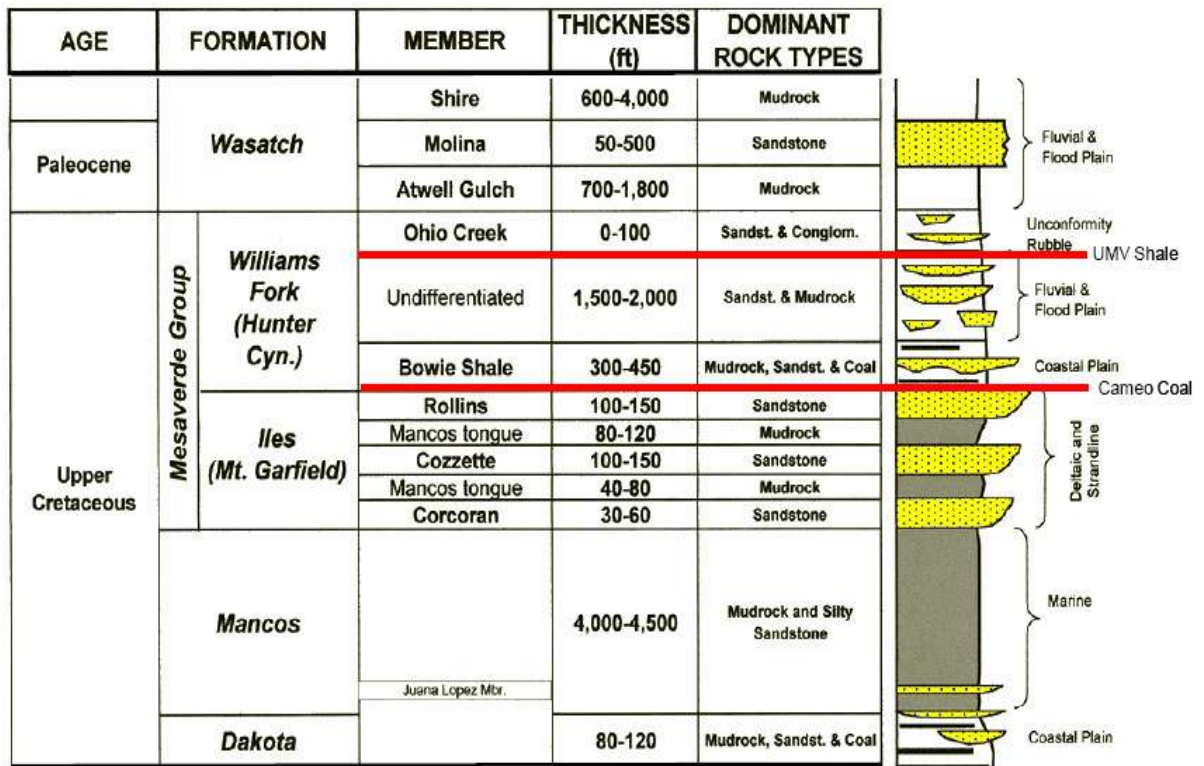


Figure 1.4: Generalized stratigraphic section (Cole and Cumella, 2003). Modified by Keighley, 2006.

Piceance Basin-Centered Gas Model - Present Day

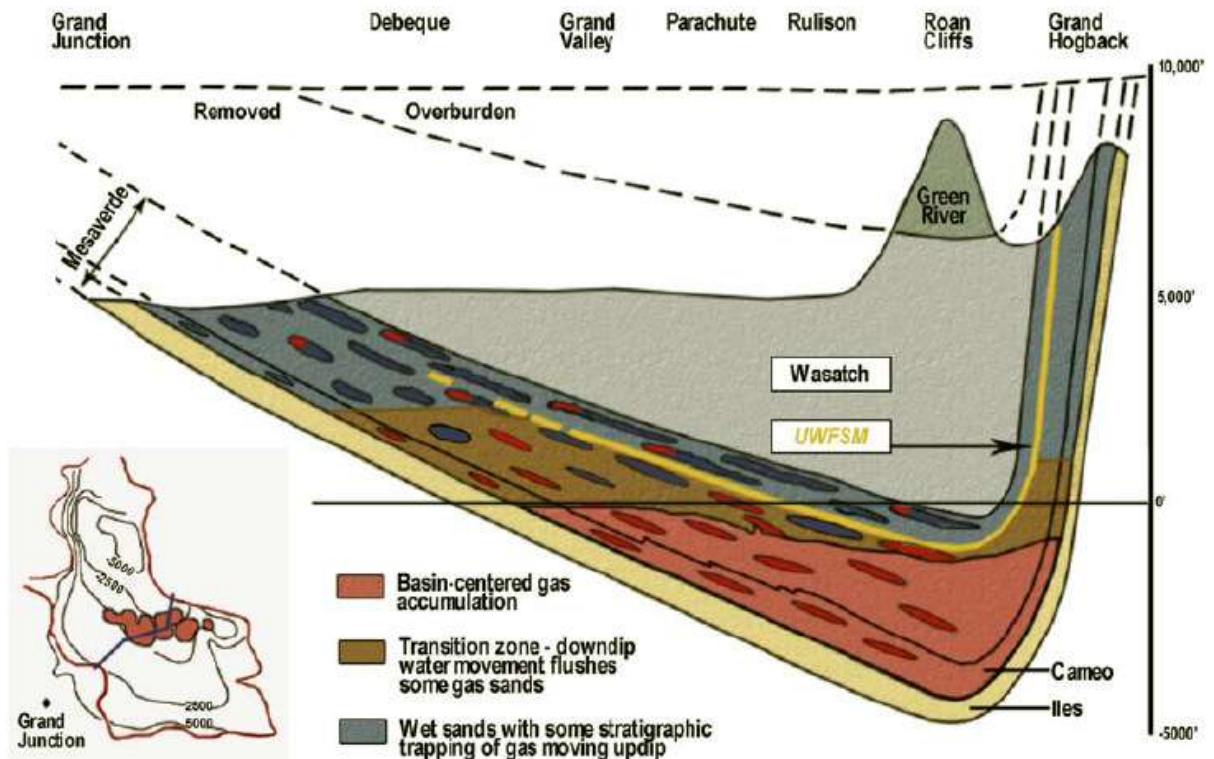


Figure 1.5: An idealized cross section of the Piceance basin showing the location of Rulison field and the Williams Fork production interval. This also shows the proximity to the Grand Hogback monocline which is responsible for the eastern uplift of the Piceance. From Cumella and Ostby, 2003.

Just above the Mancos the Mesaverde Group begins with Iles Formation, which consists of approx. 750 ft. of sandstone that underlies the Cameo coal. The Cameo coal is the beginning of the Williams Fork Formation (see fig. 1.4). The lower Iles Formation is of deltaic and beach origins, while the Cameo and Rollins Formations were deposited in the lower coastal plain environment. The Cameo coal zone is generally a continuous formation that is separated by sandstone and shale deposits from meandering streams. Deposition above the Cameo zone is almost entirely fluvial due to sea level drop. The Williams Fork Formation above the Cameo interval consists of laterally discontinuous stacked channel sands that are fluvial and flood plain deposits from meandering streams

(Cumella and Ostby, 2003). The upper Williams Fork Formation sands are lenticular in nature, and moving up in formation a depositional change from amalgamated channel sands to braided stream deposits is seen. Due to the depositional environment, sands in this area are not considered ‘clean’, meaning that they are mixed with clays. The top of the Williams Fork Formation contains an approximately 20 ft. thick continuous shale marker known as the UMV shale. This provides an excellent reflector for seismic, and also as a cap for gas and pressure in the Williams Fork Formation. The Williams Fork Formation is recognized as an overpressured formation, meaning that pore pressures in the formation are higher than the normal hydrostatic gradient of .433 psi/ft (fig. 1.6). This lends added importance to the changes in pore pressures as they are indicative of production and also to stress changes within the reservoir.

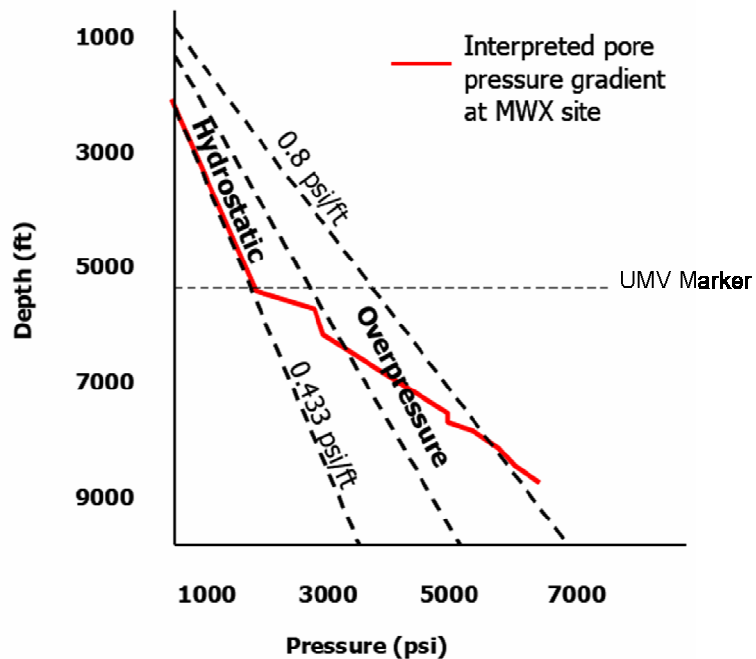


Figure 1.6: Pore pressure gradient as a function of depth from the MWX site. This is indicative of the pressure gradient at Rulison field due to the MWX proximity to the field (approx. 4 miles away). Modified from Rojas, 2005.

1.4 Stress History of Rulison

The initial geomechanical study performed at the RCP Rulison field area by Shannon Higgins showed that an understanding of the stress and burial history is critical to understanding present day stresses. The DOE sponsored tight gas investigations at the MWX site are also excellent analogues for the study of Rulison, due to its proximity and similar geology (fig. 1.7). What follows is an overview of the stress and burial history of Rulison field by several authors (Higgins, 2006; Jansen, 2005; Johnson and Nuccio, 1986; Lorenz, 1985; Lorenz and Finley, 1991; Warpinski, 1989).

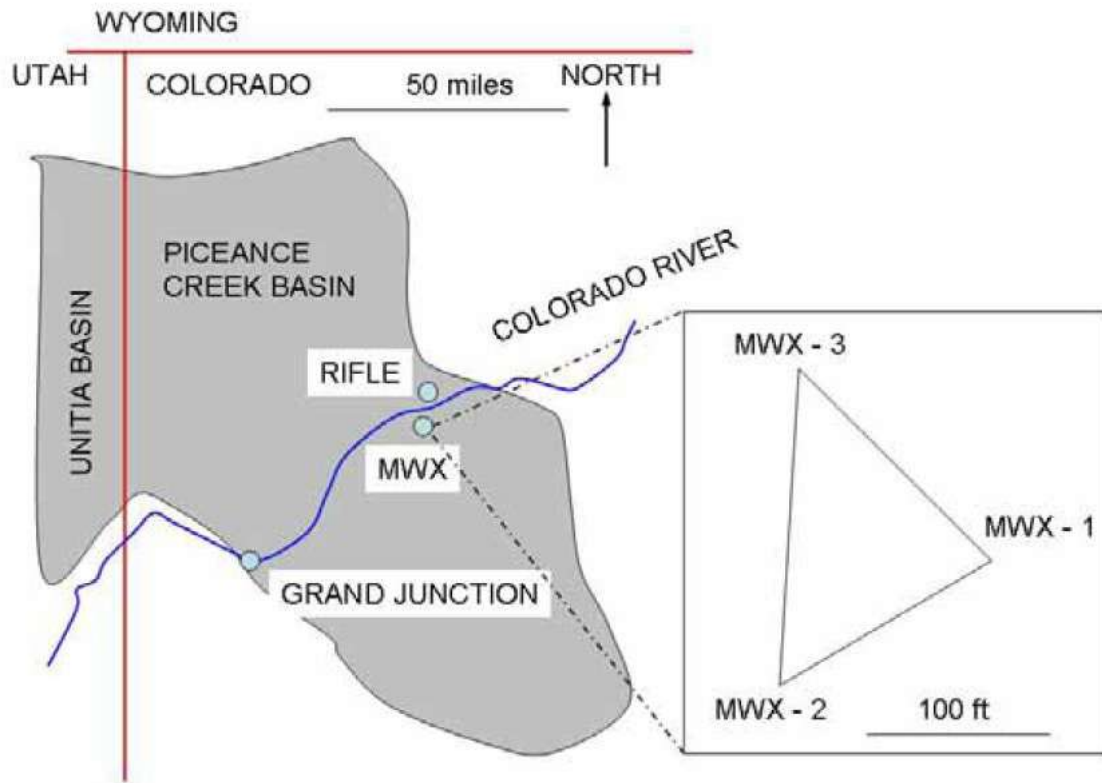


Figure 1.7: Location of MWX DOE site with respect to Rifle, CO. Modified from Higgins, 2006.

Seventy-five million years ago the deposition of the main production interval at Rulison field, the Mesaverde group, began. Deposition was followed by burial until about

37 million years ago when the Mesaverde reached its maximum depth of burial. During this time the producing interval at Rulison became overpressured due to gas generation and migration into the formation (Warpinski, 1989). The natural fracture systems that are present today at Rulison are a result of this time period as well (Lorenz and Finley, 1991). Due to high pore pressures, high temperatures, high overburden stress, and the compressive west-northwest trending stress from the thrust belt during this time; the Mesaverde is considered overpressured, as seals present at the top of the formation maintain this overpressure to this day (Lorenz and Finley, 1991) (fig. 1.8).

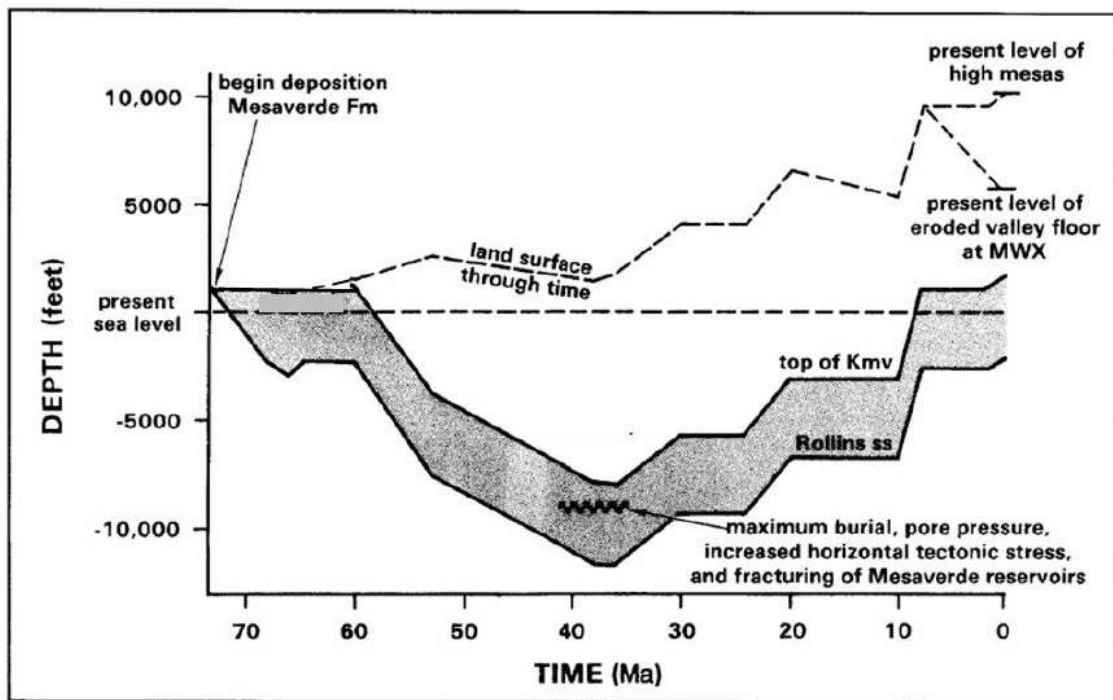


Figure 1.8: Burial history from MWX site which is analogous to the burial history at Rulison field. Figure is from Lorenz and Finley, 1991.

The stress magnitudes and orientations that are present at Rulison today are the product of high tectonic stresses and loading from the Sevier and Laramide orogeny events (fig. 1.9) (Lorenz and Finley, 1991). The Sevier orogeny took place as the North American plate overrode the Pacific plate to the west of the Rocky mountain range. This

orogeny caused the overthrust belt in Utah to form, which also affected the western edge of the Piceance basin and coincidentally Rulison field. The end of the Sevier orogeny suspended change to the west side of the Piceance basin, but the Laramide orogeny caused uplift of the eastern side of the basin.

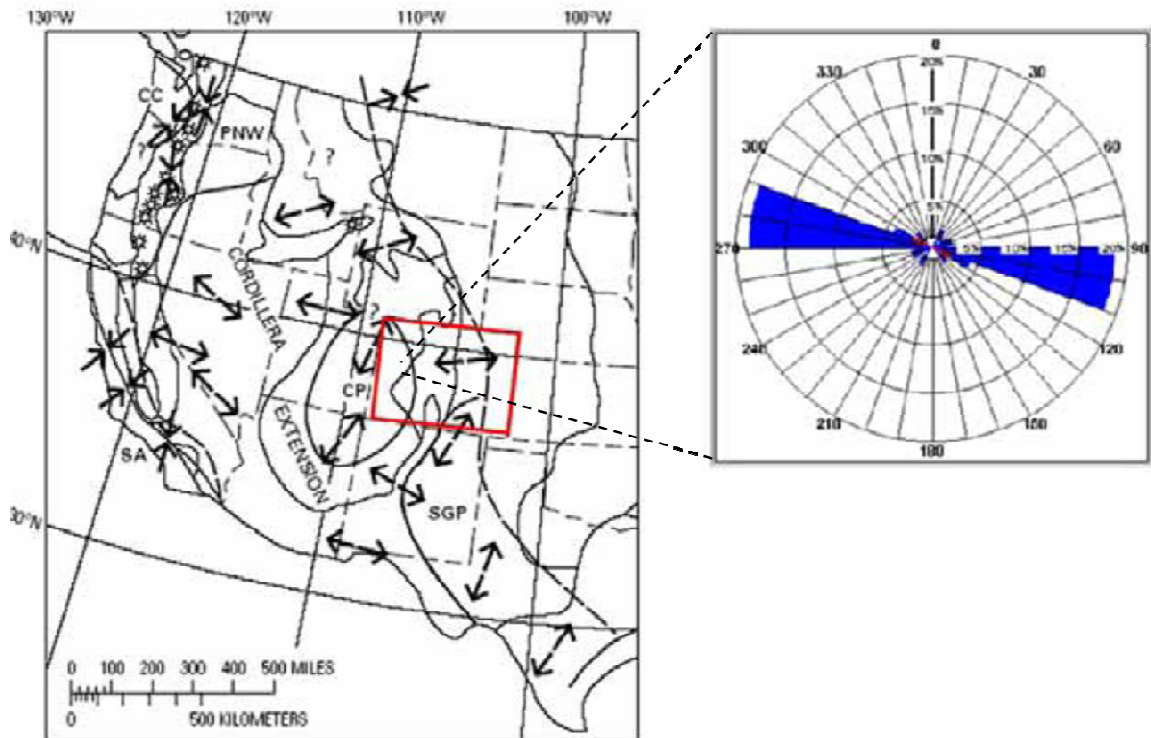


Figure 1.9: Left side shows stress field from regional view showing generalized stresses for the Rockies. The rose diagram to the right is from image logs taken from a well within the RCP study area at Rulison field. This shows maximum horizontal stress direction. Modified from Higgins, 2006.

The uplift of the White River plateau to the east of Rulison field caused further compressive loading to the Rulison area in the same direction as the Sevier orogeny compression (Lorenz and Finley, 1991). The White River uplift marked the end of the deepest burial history of Rulison, and since then the field has been uplifted from tectonics and erosion of overlying materials (see fig. 1.8 above).

Despite the dominant fracture trends within the Piceance basin (west-northwest and east-southeast), there are areas where fracture directions vary greatly from the norm. This phenomenon usually occurs near areas of structure, or where stress reorientation is needed due to large tectonic or structural changes. Examples of this would be the Hogback monocline, the Divide Creek anticline, or areas of regional uplift when not on anticlines (Lorenz and Finley, 1991 and Verbeek and Grout, 1997). Fault interpretations based on seismic and regional structural analysis have suggested that these swarms may also be present in Rulison field, and the RCP study area (Riley, 2007).

The stress history of Rulison is important due to the fact that present day fracture direction and stress magnitudes are a major factor controlling completions. Areas enhanced by natural fractures have one to two orders of magnitude increase in permeability, as shown by the difference in lab measured matrix permeabilities versus well test permeability at the MWX site (Lorenz, 1989). Fracture orientation and stress magnitudes control the effectiveness of completions and therefore are a necessity in understanding how completions are to be properly implemented and their effect on the surrounding formation.

1.5 Objectives

The objectives of this study are; to explore if slow shear time-lapse seismic is imaging areas of pressure and stress change as shown by 3-dimensional geomechanical modeling, how these seismic changes can be used to optimize perforations, stimulations, and placement of completions, and to study how and if far-field depletion will affect future drilling and completions decisions. In addition to this, the modeling carried out

here will provide insight into the sensitivity of inputs into the model and how these inputs can affect future models that are built.

CHAPTER 2

MINI-FRACTURE TESTING AND ANALYSIS

2.1 RCP Data Set

Access was granted to Williams' well log and production data. Also, there were three dedicated time-lapse surveys completed; the base survey in 2003, a monitor survey in 2004, and the final monitor in 2006 within the RCP study area (fig. 2.1). In addition to these surveys, two 3D VSP's were collected, one of which is still being analyzed and interpreted. A pressure test was also collected and analyzed for this study (see below) to test the comparison of pressure and stress to seismic signatures.

Reservoir characterization has been carried out by several authors within the RCP over the course of this phase: a legacy time-lapse study from 1996 to 2003 using the DOE survey that overlaps the RCP study area (see fig. 2.1) (Kusuma, 2005), a dedicated P-wave and S-wave time-lapse analysis over the RCP study area from 2003 to 2004 (Keighley, 2006 and Rumon, 2006 respectively), a pressure related rock physics study (Rojas, 2005), a 1-D geomechanical model (Higgins, 2006), fault mapping from seismic (Jansen, 2005), a V_p/V_s analysis (Guyliev, 2007), and a microseismic study and analysis (Riley, 2007). In addition to these theses written on Rulison, there are also several ongoing studies analyzing the most recent VSP, the time-lapse response including the 2006 seismic survey, and ongoing reservoir modeling and simulation studies. This work combines many aspects of this past work and also utilizes other models, such as the reservoir modeling and simulation, without which this work would not have been possible (see Ch.3).

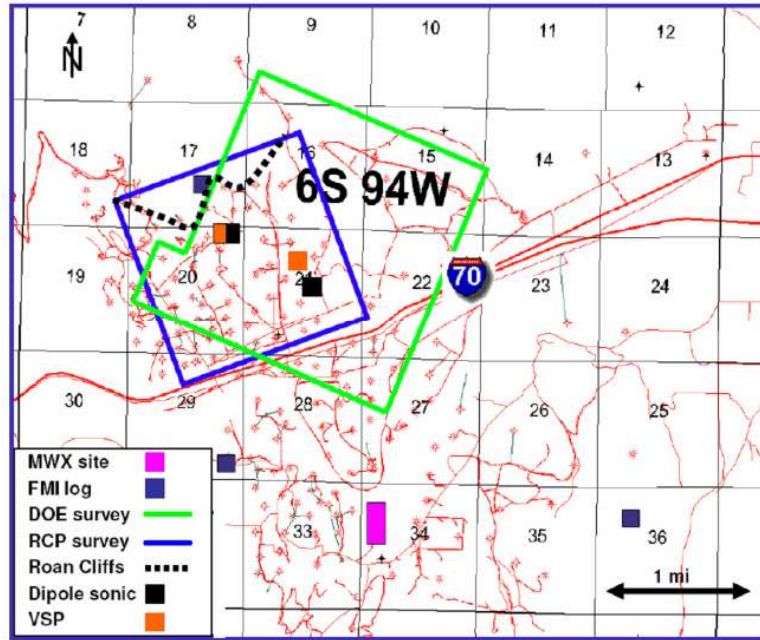


Figure 2.1: Location of RCP and 1996 DOE survey areas. Also included are locations of specialized well logs and VSP's.

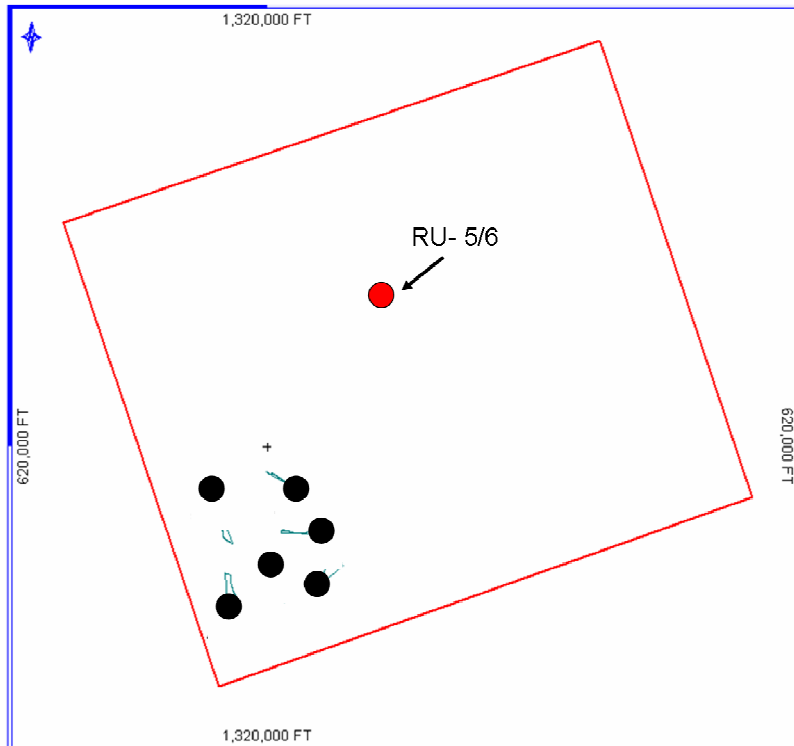


Figure 2.2: Diagram showing location of earlier pressure tests to the location of well RU-5/and RU-6 (two wells from one pad) within the RCP study area. Black dots denote the locations of previous pressure tests that were completed by Williams.

2.2 Mini-fracture Test Introduction

A series of mini-fracture tests were carried out on well RU-5 (see fig. 2.2) within the RCP study area, and also in the high fold seismic area. Mini-fracture tests are commonly used to gather information about pore pressures and minimum horizontal stress magnitudes. This test was carried out in a well drilled in June of 2006 to test the concepts of completing into depleted zones and for further validation that time-lapse seismic is imaging areas of pressure depletion and stress change. The results of this analysis were compared to other mini-fracture tests completed within the RCP study area.

2.3 Mini-fracture Basics

Mini-fracture tests are tests where a small amount of fluid is pumped at a constant rate into the formation to cause a fracture, pumping is continued until a drop in pressure is noted, pumping is stopped, and the well is then monitored as the fracture closes (fig. 2.3) (Fjaer, et. al., 1992). To achieve this, the formation of interest is isolated, and the fracture fluid is introduced at a constant rate into the formation. The pressure is monitored for a point where a fracture is opened (FIP); once a fracture has been initiated the well is shut in (ISIP) and then monitored with a pressure gauge at the surface of the well (Higgins, 2006). As the fracture closes magnitudes of minimum horizontal stress can be ascertained (Closure Stress), as can information about the pore pressure. The closure stress is where there is no longer fluid holding the fracture open and this pressure is needed to close the fracture. Since the direction of the fracture is in the direction of present day maximum horizontal stress, the value at closure is then the minimum horizontal stress (fig. 2.4). The pore pressure is assumed to be the final point where flow back is coming strictly from the matrix and natural fractures, and not from the mini-fracture closure (Pore Pressure).

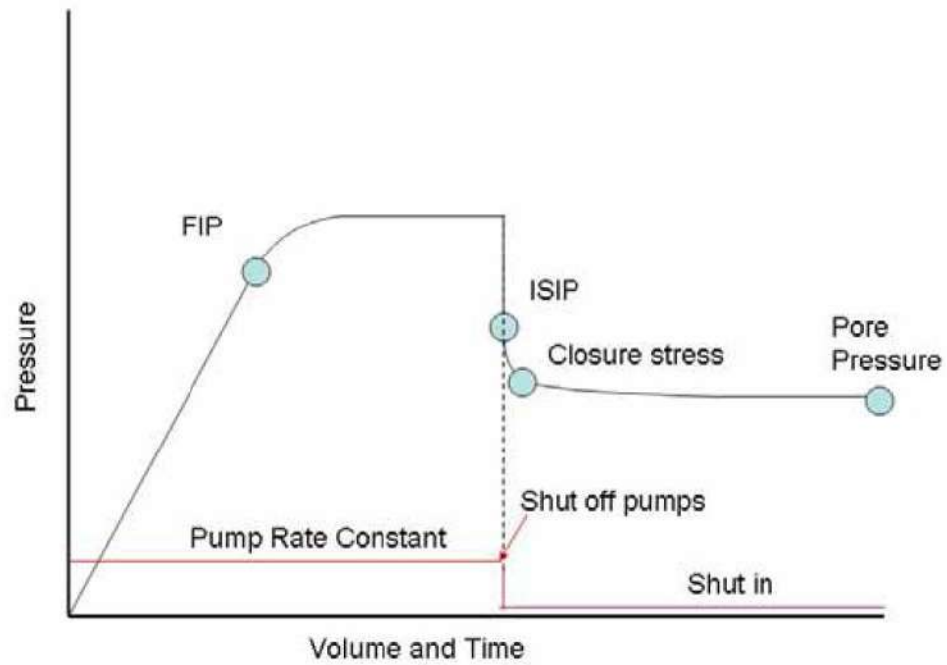


Figure 2.3: Generalized diagram of a mini-fracture test. From Higgins, 2006.

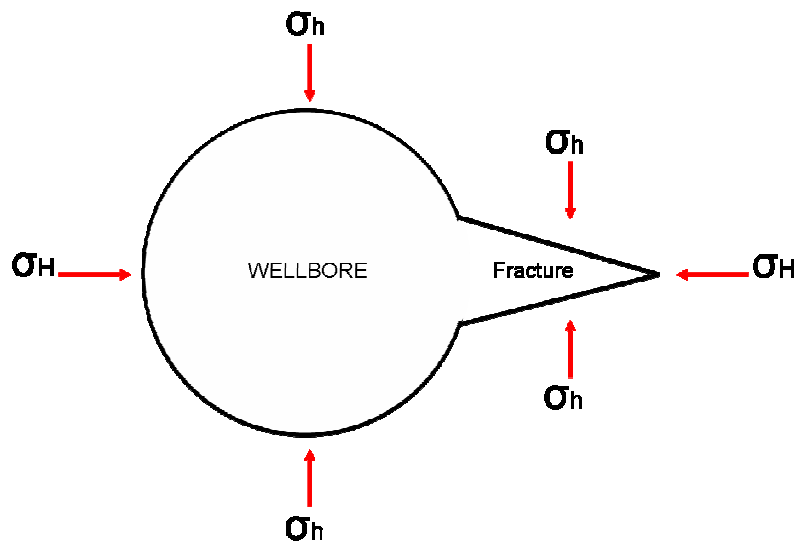


Figure 2.4: Generalized diagram of a mini-fracture. σ_H denotes maximum horizontal stress direction while σ_h denotes minimum horizontal stress direction. σ_h is closure stress as stated above.

2.4 Mini-Fracture Analysis

Analysis of the mini-fracture test on well RU-5 was completed by Halliburton. This included the completion of the test in the field, as well as the interpretation of the data. Halliburton analyzed the data using the analysis technique of the G-function, its derivatives, and a specialized analysis for permeability. A complete overview of these techniques can be reviewed in Barree et. al. 2007. This section will concentrate on the results of these techniques and their comparison to time-lapse seismic analysis.

Halliburton completed the analysis of this mini-fracture test and provided the results of each test by zone. Six zones (ranging in size from 25’-60’) were tested in this pressure test, the table below summarizes the results obtained by the G-function and Cartesian pseudo linear flow plots. Depths are mid-point of interval tested.

Completion Interval	Perforated Sand Depth (ft)	ISIP	Fracture Gradient (psi/ft)	Closure Pressure (psi)	After Closure Pore Pressure (psi)	Perm to gas (k _g) (md) Modified Mayerhofer	Leakoff Mechanism
MV-5	5822.5	3792	0.65	2803	1978	0.00695	2
MV-4	6095.5	4241	0.70	3129	*	*	3
MV-3 Zn.2	6200	3696	0.61	3158	2643	0.003	1
MV-3 Zn.1	6263.5	4350	0.69	3613	2981	0.0051	1
MV-1	6849	5382	0.79	4643	3677	0.0041	1
Cameo	7237	6535	0.90	5483	4026	0.0069	2
							1-Normal
							2-PDL
							3-Height Recession

Table 2.1: Table showing results from pressure test and related analysis from well RU-5.

Table 2.1 shows the results of the analysis by Halliburton. The depths and their associated zonal names are shown along with the Initial Shut-In Pressure (ISIP), fracture gradient (which is closure pressure divided by total vertical depth or TVD), closure

pressure, after closure pore pressure, permeability of gas (k_{gas}) by the modified Mayerhofer technique, and the leakoff mechanism. The leak off mechanism is a product of the G-function analysis performed by Halliburton and is important in understanding the tests and the implications for formation analysis.

The G-function and its derivatives have characteristic results when applied to mini fracture tests. A normal leakoff G-function analysis is that shown in figure 2.5.

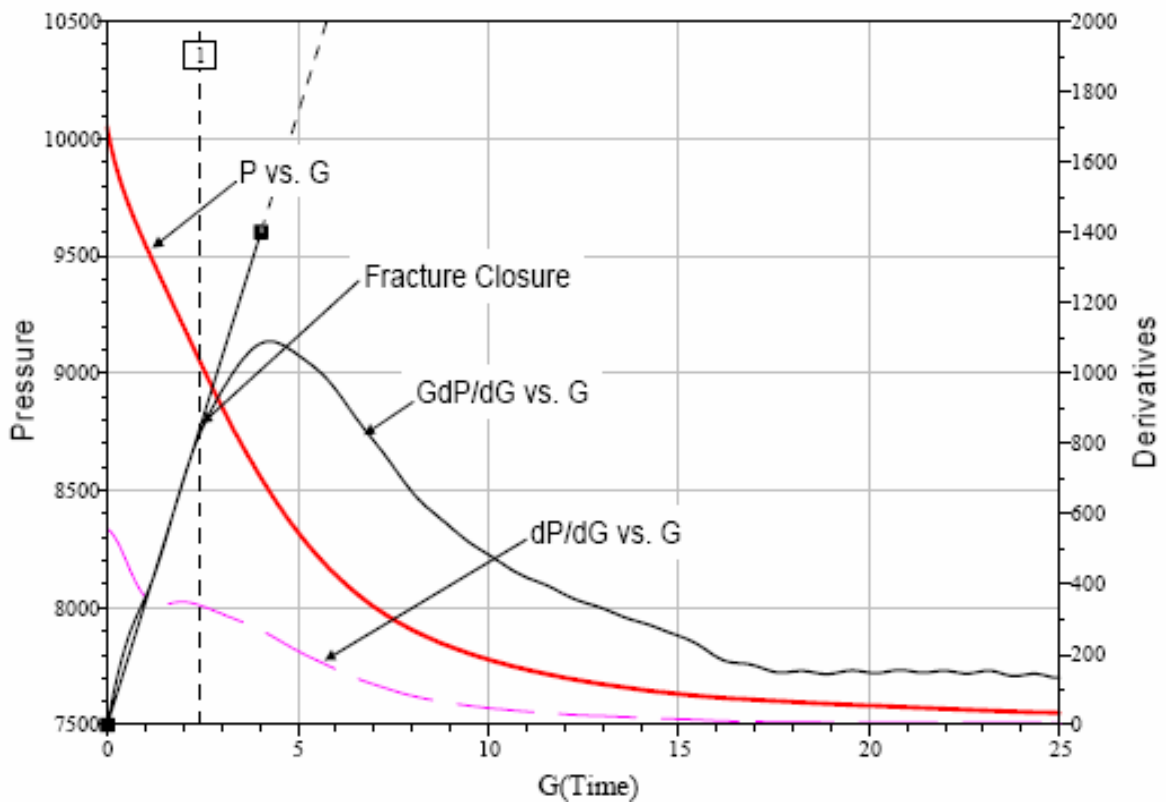


Figure 2.5: Generalized G-function plot (leakoff mechanism one in table one) showing Pressure vs. G(time), G-function (Gdp/dG vs. G(time)) and dp/dG vs. G(time). This is for normal leakoff into the the formation. Departure from the tangent line denotes fracture closure (shown by dashed line 1). From Barree et. al., 2007.

The expected signature of the G-function semi-log derivative is a straight line through the origin (zero G-function and zero derivative)(Barree et. al., 2007). In all cases the correct straight line tangent to the semi-log derivative of the pressure vs. G-function

curve must pass through the origin (Barree et. al., 2007). The deviation of the GdP/dG vs. $G(\text{time})$ from this tangent line denotes characteristics about the formation. The examples that pertain to the analysis of RU-5 are shown in figures 2.6-2.7 which are representative of the G-function response in the actual Rulison mini-fracture data.

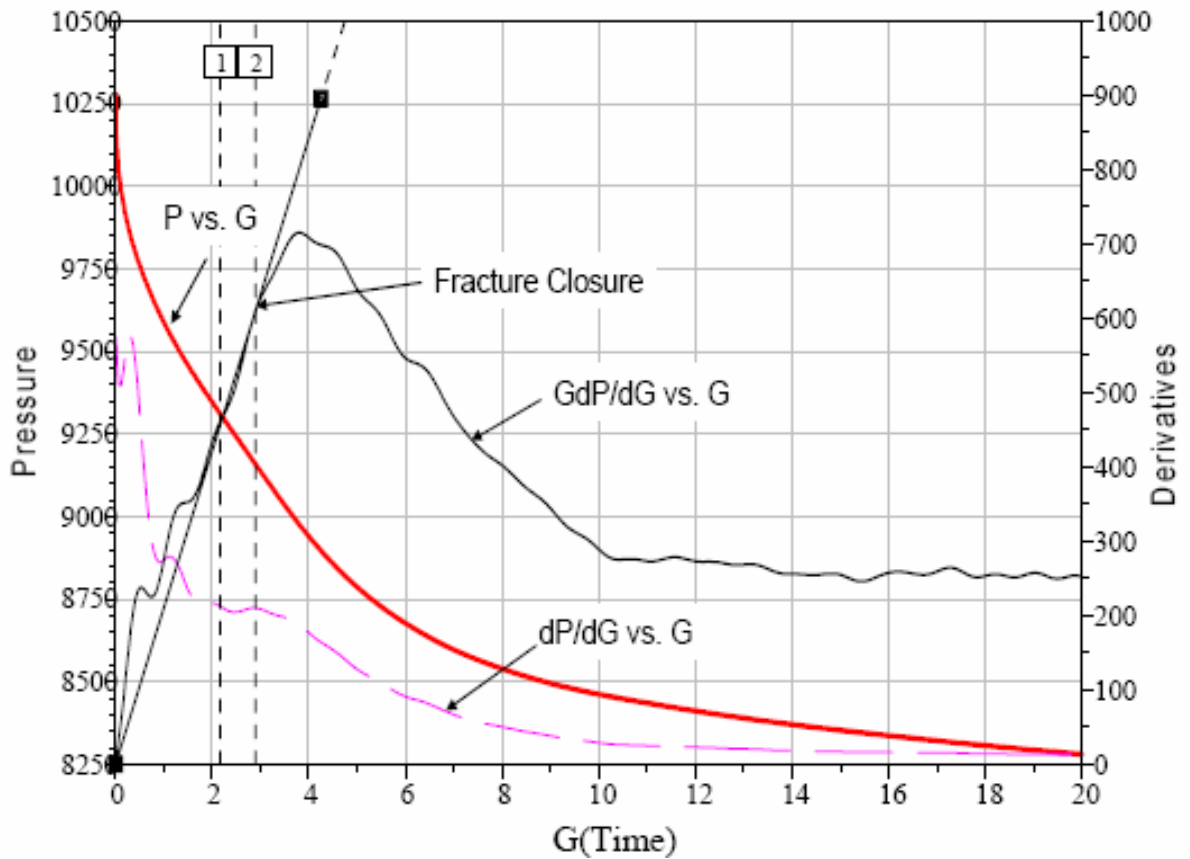


Figure 2.6: Generalized G-function plot showing pressure dependent leak off (denoted by leakoff mechanism two in table one). The characteristic ‘hump’ denotes pressure dependent leakoff (PDL). From Barree et. al., 2007.

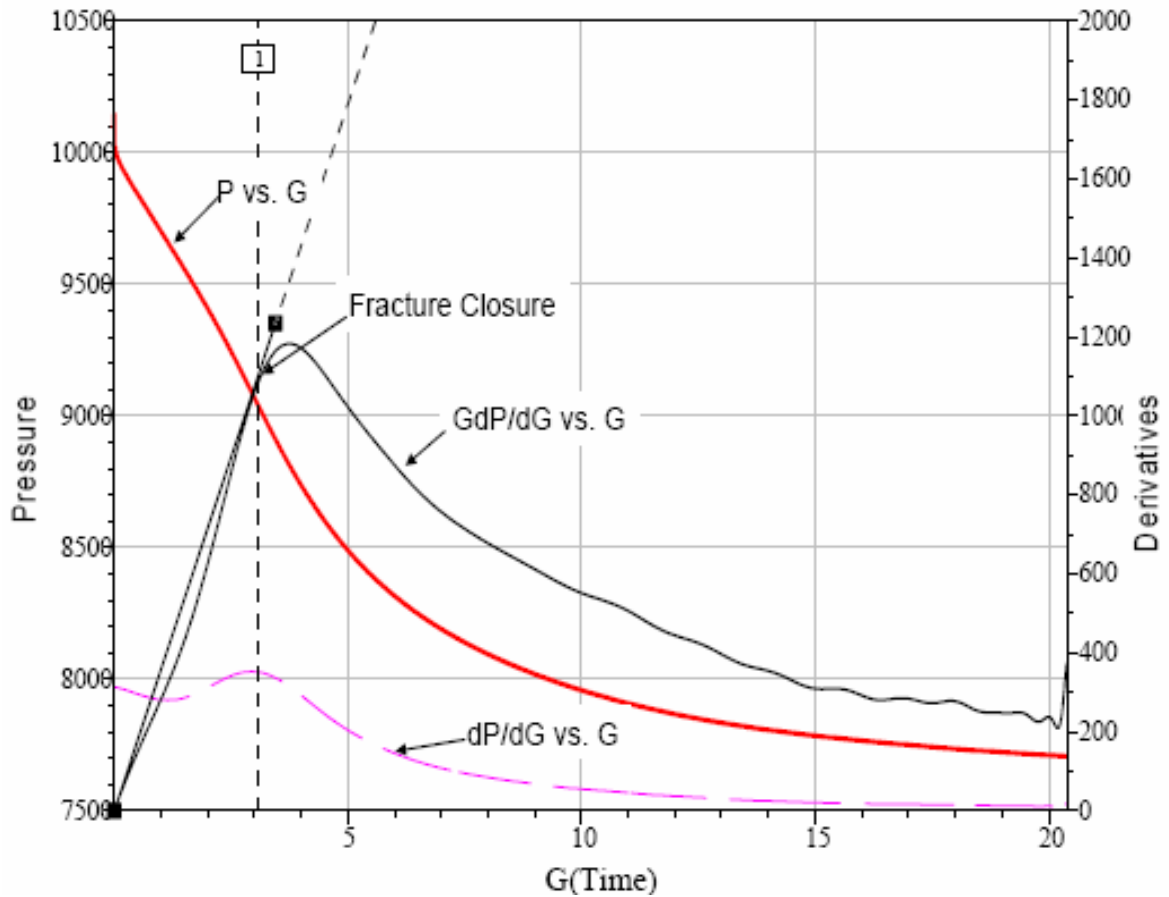


Figure 2.7: Generalized G-function plot showing height recession (denoted by leakoff mechanism three in table one). This is shown by the characteristic ‘belly’ of GdP/dG vs. $G(\text{time})$. From Barree et. al., 2007.

Pressure dependent leak off in a reservoir with pressure-variable permeability or flow capacity is usually caused by natural or induced secondary fractures or fissures (Barree et. al., 2007). Height recession is caused by the fracture treatment growing out of zone into another formation. This unrestricted height growth means that the formation in this area cannot be analyzed for pore pressure or k_{gas} , as shown in table one. These generalized examples are shown as examples for the analysis done on well RU-5. The G-function is shown here as it is the easiest visual tool for analysis. Shown below are the G-

function results from well RU-5 for the three different leakoff mechanisms shown above (fig. 2.8-2.10).

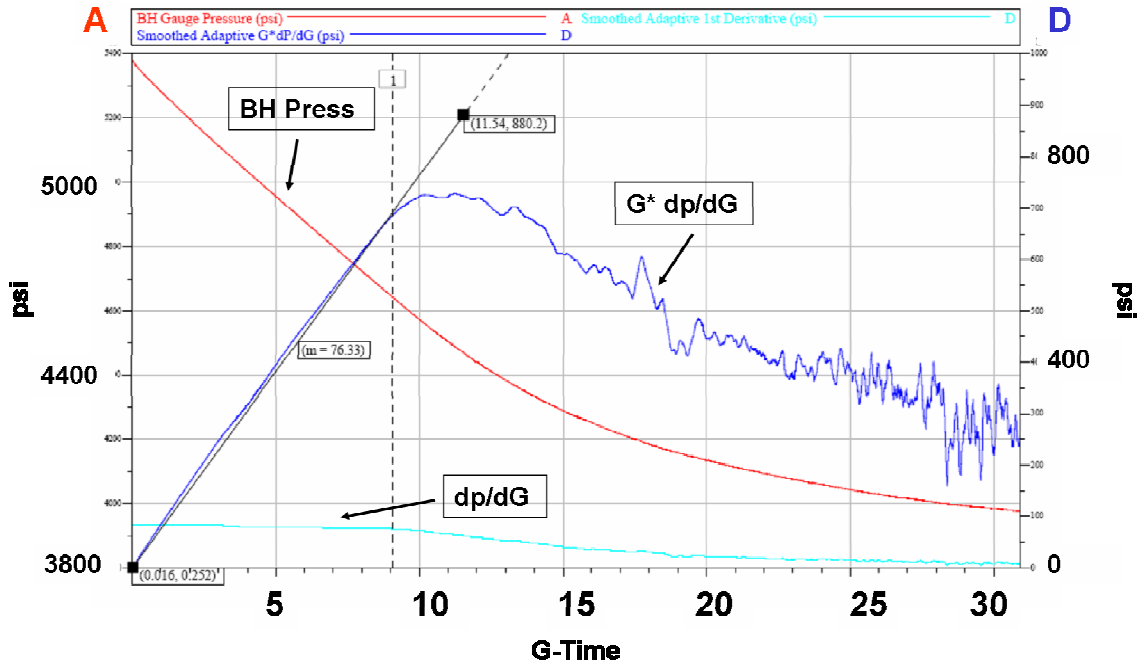


Figure 2.8: G-function plot for zone MV-1 showing normal leakoff mechanism. Analysis performed by Halliburton.

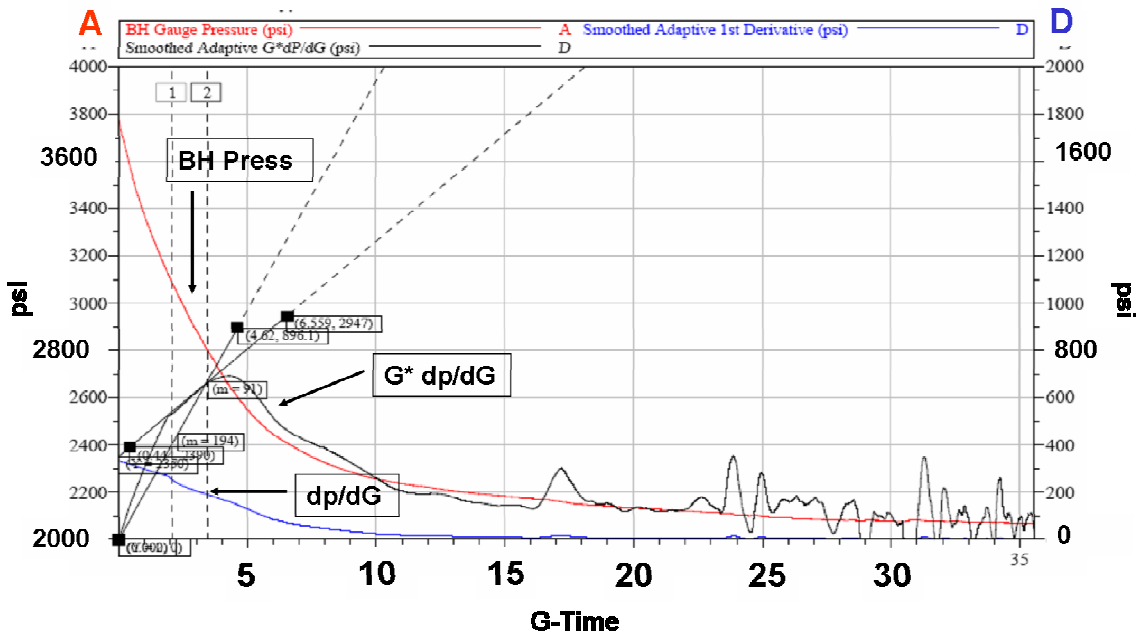


Figure 2.9: G-function plot for zone MV-5 showing storage caused by natural fractures. Analysis performed by Halliburton.

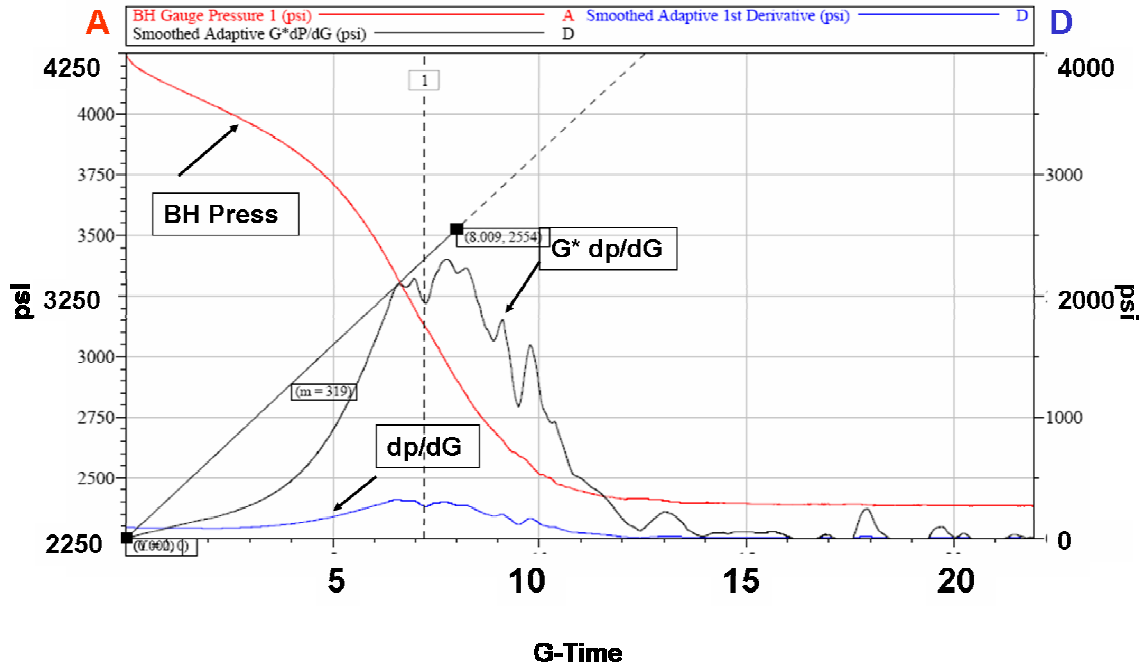


Figure 2.10: G-function plot for zone MV-4 showing height recession caused by unrestricted fracture growth out of zone. Analysis performed by Halliburton.

2.5 Mini Fracture Results

From the above analysis pore pressures and closure stresses were collected. This resulted in the RCP having the ability to not only compare these minimum horizontal stress magnitudes and pore pressures to those of other wells in the field, but also to compare these with the time-lapse seismic data.

Shown in figures 2.12-2.14 are the results of the mini-fracture tests compared to other tests in the field, and then compared to the time-lapse slow shear wave data. Studies performed by past authors at Rulison (Rumon, 2006) have shown that slow shear seismic data, specifically slow shear impedance change, is the most sensitive to pressure depletion and stress change. Therefore, this mini-fracture test is compared to the slow shear impedance changes from 2003-2004. For a complete overview of the processing that was done to the shear wave data please see Rumon, 2006.

At this point it is necessary to give some shear wave basics. Shear waves are much more suited to our needs than compressional waves in this naturally fractured reservoir for several reasons. Shear waves are induced horizontally, and assuming the medium is isotropic, the horizontal particle motion will be aligned with the horizontal source (Thomsen, 2002). Rulison, however, is not isotropic (vertical fracturing is present) and this causes the phenomenon of shear wave splitting. Shear wave splitting is caused by the polarization of the initial wave being at an angle different than the dominant crack direction. This splitting results in two shear waves, a fast and a slow (referring to propagation speeds). The fast shear wave (S11) is polarized parallel to the crack set, and the slow shear (S22) is polarized perpendicular to the crack set (Thomsen, 2002) (see fig. 2.11). Therefore, S11 only samples the stiff matrix component of the rock while S22 samples both the matrix and crack component (Thomsen, 2002). The physical nature of the slow shear wave suits our needs to monitor pore pressure depletion. This requires special processing to rotate the shear data to the dominant crack direction (Rumon, 2006). This direction is N45W which was taken from the 2003 VSP by reducing the off-diagonal energy in S12 and S21. Please note that this is the average direction for the reservoir. It has also been shown by Rumon, 2006, that slow shear impedance differencing is the most appropriate to interpret due to lower noise levels versus simply slow shear velocity differences. S22 impedance is (velocity x density). Again, for a complete overview of this processing and time-lapse analysis please see Rumon, 2006.

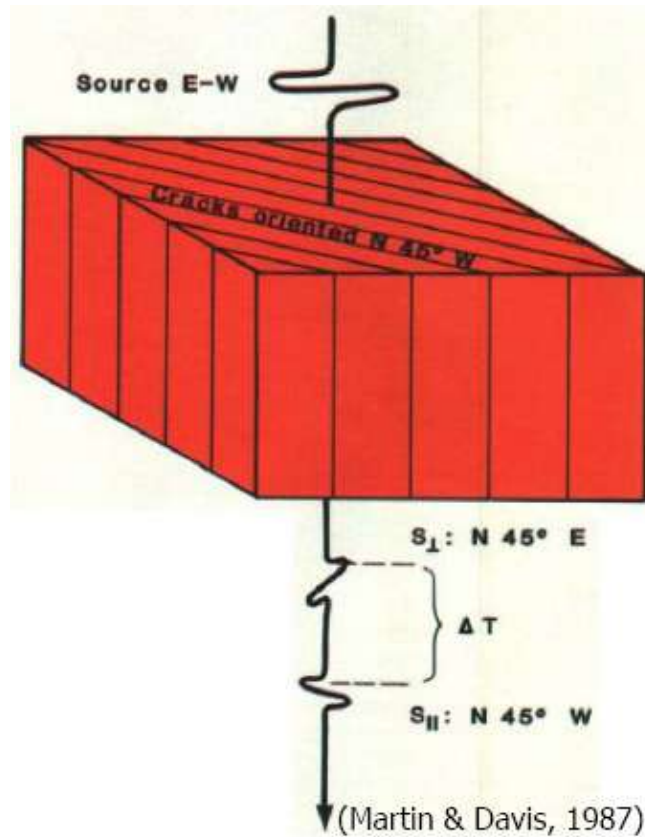


Figure 2.11: Figure highlighting shear wave splitting phenomenon. Note parallel shear wave (S1) is faster than perpendicular shear wave (S2). From Martin and Davis, 1987.

The first step after analyzing and compiling the data from the mini-fracture to RU-5 is to compare its results to those of others available in the field. Williams has kindly provided all pressure data that was available in the RCP study area. An analysis of the virgin pore pressures were done by Williams and are detailed below. Shannon Higgins completed a similar analysis and also included a minimum horizontal stress magnitude analysis for the field.

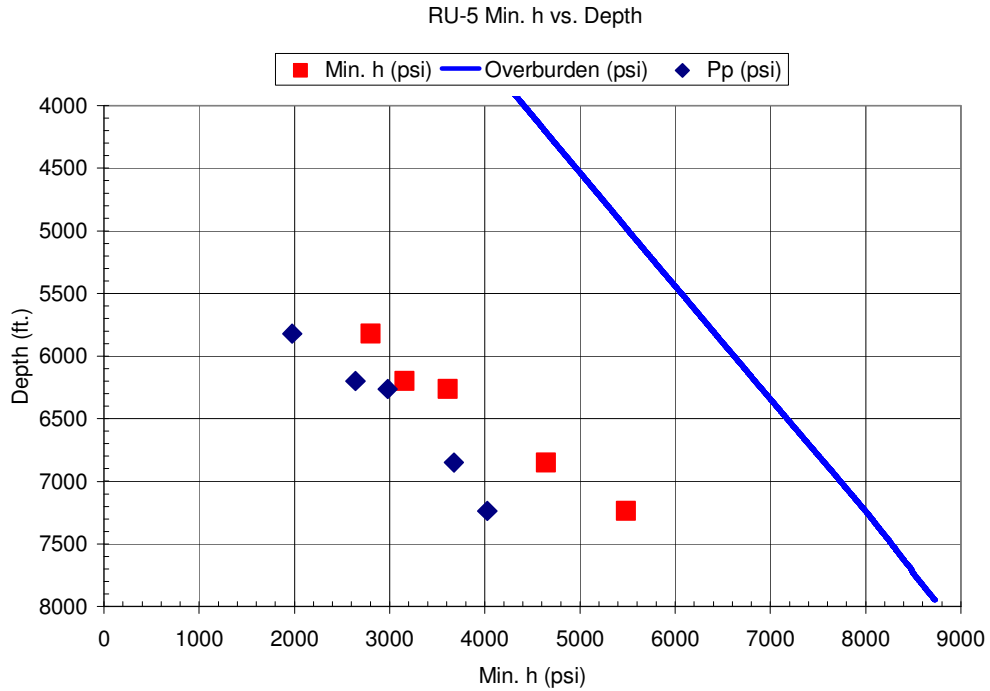


Figure 2.12: Chart showing results of mini-fracture test in RU-5 with the overburden.

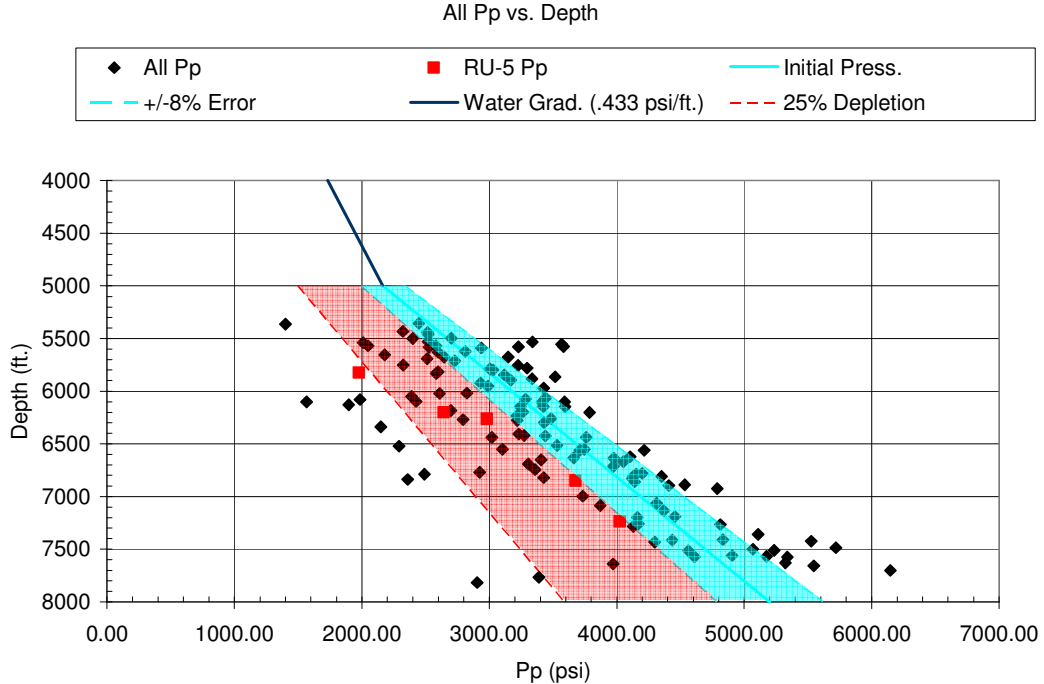


Figure 2.13: Chart showing pore pressure along with the virgin pore pressure gradient from Williams. The blue window is 8% error that was calculated by Williams. The red window shows partial depletion while the red dashed line denotes 25% depletion. Red dots denote RU-5 while black dots are all other pressure data available in the field.

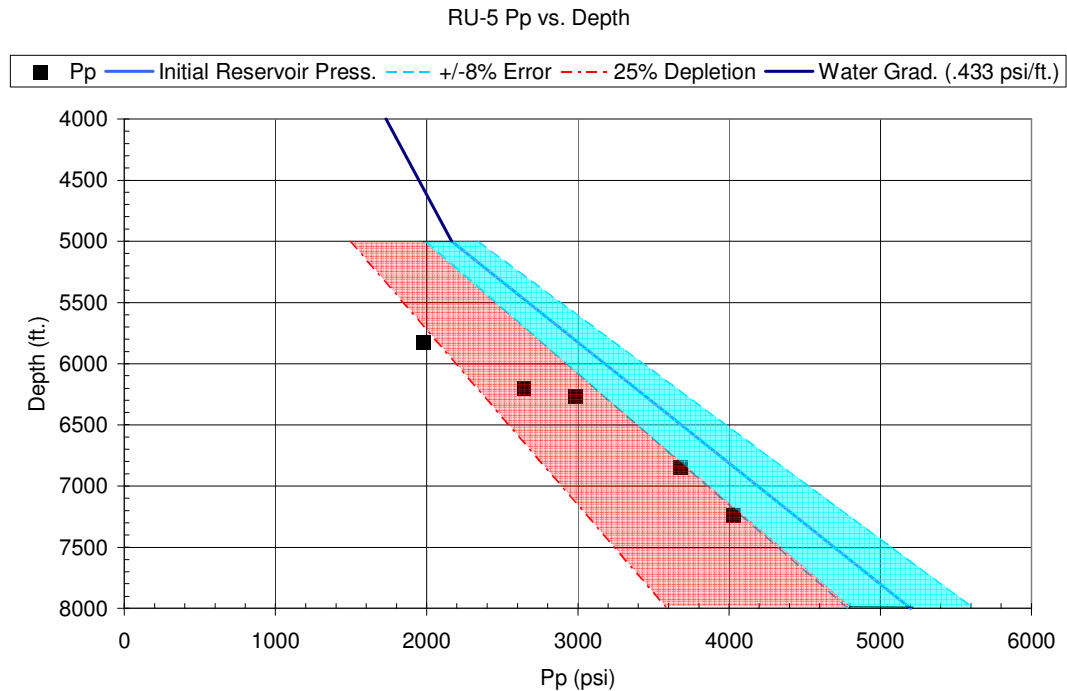


Figure 2.14: Chart showing pore pressure along with the virgin pore pressure gradient from Williams. The blue window is 8% error that was calculated by Williams. The red window shows partial depletion while the red dashed line denotes 25% depletion.

It can be seen from figures 2.12-2.14 that pore pressure in the upper three zones that were tested are partially depleted to greater than 25% depleted. It is also important to note that this well was drilled in the summer of 2006, and tested in September of 2006. No production had occurred before this well was tested. Therefore we can assume that the zones that were tested in the upper three zones are partially depleted from well communication. This fits with the geologic interpretation that amalgamated channel sands dominate deeper while more connective braided stream deposits are higher up section in the Williams Fork Formation (Cumella and Ostby, 2003). Due to the highly compressed and tight environment of this field this communication should be coming from a nearby well. We can also assume that although possibly low, pressure change was

occurring along these zones during the 2003-2004 period from base to monitor time-lapse surveys. This is shown by figure 2.15 which shows the pressure data compared to the seismic.

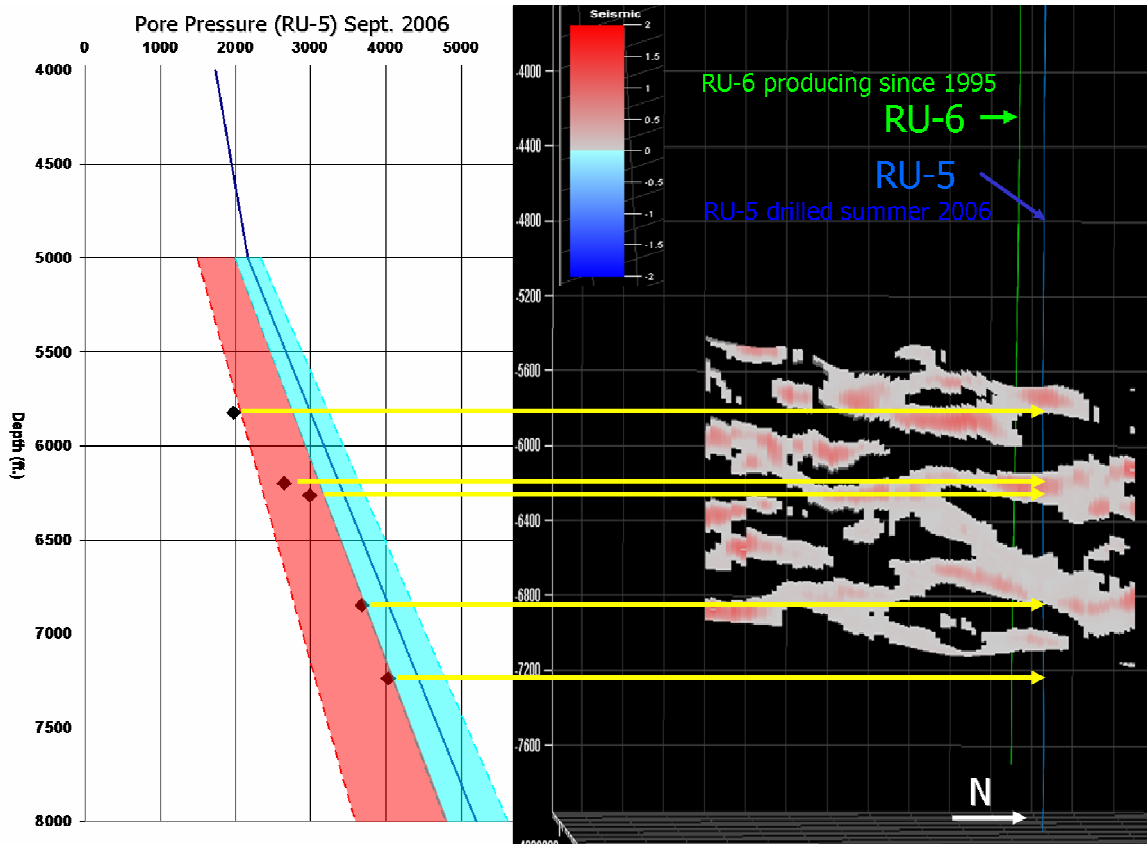


Figure 2.15: Figure showing pore pressure in RU-5 with the 2003-2004 slow shear (S22) impedance change. Also shown is well RU-6 which is from the same pad and is one (or the only) source of well communication. At these depths these wells are ~200 ft. apart

Comparison of the 2003-2004 slow shear seismic impedance change to the mini-fracture pore pressure results show that the partially depleted areas in the upper three zones correlate well to seismic changes. This analysis comes with some caveats and assumptions:

- We are assuming that the seismic change is due to pressure and stress change from production by nearby wells, and not due to noise. This is an important assumption due to the low percentage change of impedances (~2% in this area).
- Lower zones are not depleted due to either no communication with nearby wells or possibly from recharge from the Cameo coal interval.
- Upper zones are more connective than lower intervals (Cumella and Ostby, 2003)

Taking into account these assumptions we can now show that slow shear seismic impedance change is imaging these areas of pressure and stress change. These results justified moving forward with a 3-dimensional model to document pressure and stress change for time-lapse multicomponent seismic studies.

CHAPTER 3

GEOMECHANICAL MODEL INPUTS

3.1 Introduction

The generation of a 3-dimensional geomechanical model is a unique process that involves the building of several complex and intricate simulations before the mechanical program can be run. Not all the necessary work was completed on my own. A one-dimensional geomechanical model was built by Shannon Higgins and it has proven invaluable in understanding the complex stress regime in place at Rulison and in building boundary conditions for the 3-dimensional simulation. A geostatistical model of the subsurface was built by Matthew Casey; this model, its generation, and its parameters are extremely important to the geomechanical workflow. In addition, a production model was also constructed; this is a very important component as the pressure changes calculated by this simulation heavily influence the stress changes that occur within the mechanical model. A description of each of these components is described below.

3.2 Previous and Contributing Work

Shannon Higgins was the first to conduct a geomechanical analysis and build a one dimensional geomechanical model for four wells at Rulison field. Her work was the starting point for this research, and as such, shall be described in detail. In addition, Matthew Casey's PhD work (in progress) was also a large contributor to this research. Matthew has constructed a full reservoir model for the subsurface in the RCP study area. This work will also be described below as it is critical to the 3-dimensional geomechanical modeling done at Rulison field. This work would not have been possible without both Matthew and Shannon's work, thereby highlighting the need for integrated studies conducted by the RCP

The goal for Shannon Higgins' work was to provide insight into the relationship between natural and hydraulic fractures, optimal well placement, completion strategies, and hydraulic fracture design (Higgins, 2006). Shannon built one-dimensional geomechanical models for four wells, combining rock strength, static and elastic moduli, stress magnitudes, pore pressure, and stress direction. Empirical correlations were developed by Shannon to derive rock strength and static elastic parameters from well logs at Rulison field. Mini-fracture tests were used to determine pore pressure and minimum horizontal stress for the four wells at Rulison field. Stress directions were ascertained from image logs and sonic logs. This extensive data set was then integrated into continuous well models that provide stress and strength profiles for the subsurface at Rulison (figs. 3.1 and 3.2) (Higgins, 2006).

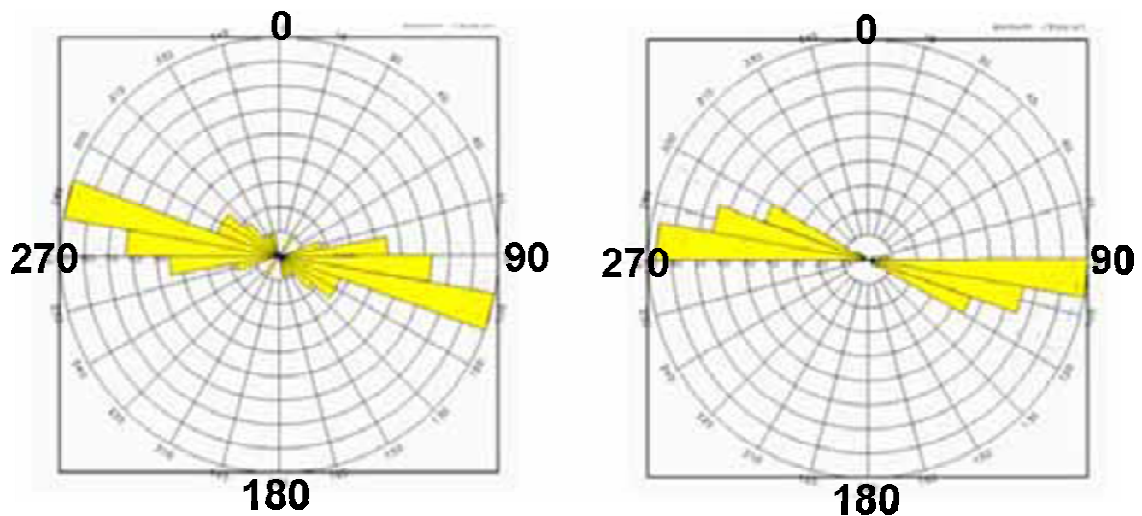


Figure 3.1: Image log rose diagrams for a well in the RCP study area for depths of 4000 to 7950 feet. In the left image the yellow shows the direction of natural fractures. In the right image the yellow shows the direction of drilling induced fractures (maximum horizontal stress). From Higgins, 2006.

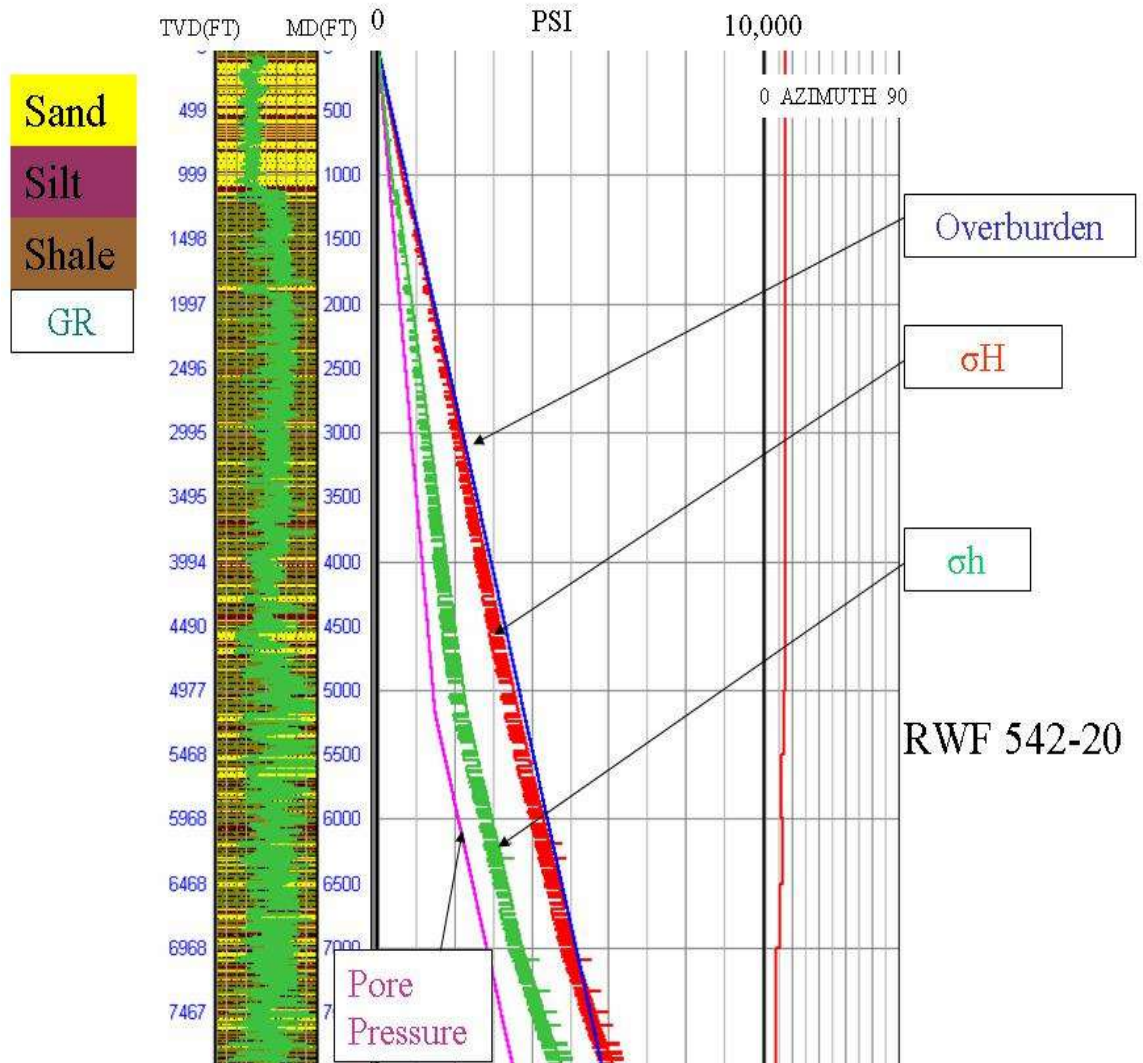


Figure 3.2: Stress profile for well 542-20 that shows results of the modeling. From Higgins, 2006.

Shannon's research found that for the wells modeled at Rulison field most natural fractures are aligned in the same direction as the direction of present day maximum horizontal stress. However, local fracture anisotropy is present (Matesic, 2006).

Shannon's worked showed that this stress regime controls hydraulic fracture growth and minimized interaction with natural fractures. In addition, provided that high horizontal stress anisotropy is maintained, fracture re-orientation projects are unlikely to succeed (Higgins, 2006). Finally, from mini-fracture tests and image logs, stress magnitudes were

found to be extremely lithology dependent, with stress in shales much higher than stress in sands. Hydraulic fractures tend to stay within the desired zone and terminate at bed boundaries. These data have been used as both a calibration and a reference for the work completed here.

3.3 Geostatistical Modeling

The construction of the geostatistical model was carried out by Matthew Casey. This is an important step in the modeling process, as vital properties such as porosity, permeability, and Young's modulus are populated throughout the model. These parameters have a significant impact on production and mechanical modeling. Due to the workflow followed, a bulleted format has been adopted to describe this process. What follows is a brief description of the steps that were taken to build the geostatistical model. For a detailed version of this please see Casey, 2006.

- The model was built from all 121 wells in the RCP study area, although only the high-fold seismic area in the reservoir interval was gridded and populated
- Lithology logs were built for all wells using a gamma ray cutoff of 80 API
- A probability cube of sand, shale and a transition zone was built from Keighley (2006) and Rumon (2006) for seismic, and Rojas (2005) for rock physics from MWX.
 - This resulted in a probability cube based on volumetric V_p/V_s (see Ch.2) scaled according to rock physics lithology correlations for sandstones and shales

- The lithology logs were always honored while the seismic probability cube was used as soft data for Sequential Indicator Simulation (SIS) which is a two-point variogram statistical method
- Facies were populated with porosity using Sequential Gaussian Simulation (SGS)
 - Φ vs. S_w used to constrain water saturation (shales are 100% S_w and no flow)
 - Φ vs. Young's modulus was used to populate Young's modulus and other mechanical properties

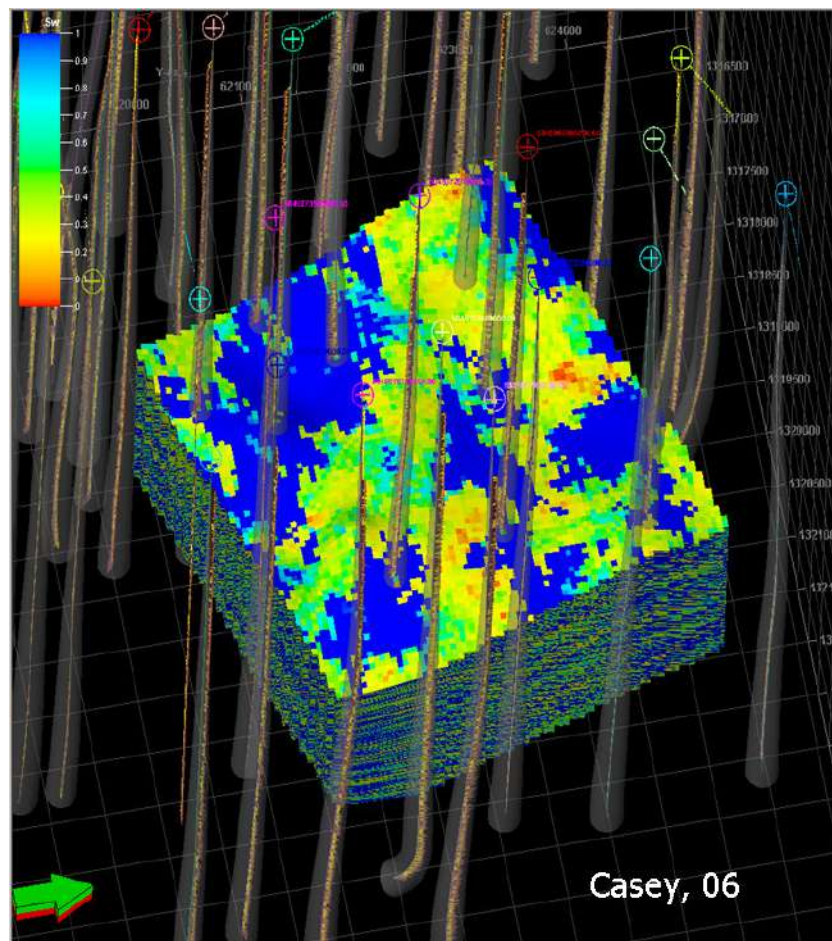


Figure 3.3: Figure showing water saturation for geostatistical model in reservoir interval of high fold seismic area. From Casey, 2006

It is important to note that the path of Young's modulus, as simulated by this model, has a strong impact on the path of production and stress. Therefore, we have built the most realistic model that we can at this time and chosen the most appropriate out of ten created realizations. That being said, the connective pathways in this model are not the same as those in the subsurface, and this model can be seen as our 'best educated guess', as they are restricted by two point statistics' ability to model connective and laterally/vertically heterogeneous geology. From this model, a section of reservoir was selected for production modeling.

3.4 Production Modeling

The model of production with time was constructed by Schlumberger Data and Consulting Services (DCS) Greenwood Village, CO. This model predicts production change with time within the reservoir. This modeling step is also important, as will be outlined in detail in the next chapter. The location of pressure change has a direct impact on where the model calculates 3-dimensional effective stress changes. This is particularly true where we have modeled hydraulic fractures, as hydraulic fracture stress change will have a dramatic effect on production; this is shown below in figure 3.6. The following steps were taken to produce the production model, again, due to the workflow a bulleted format has been adopted for ease of description. A full description of simulation processes can be found in the SPE monograph series on reservoir simulation by Mattax and Dalton, 1990.

- A black oil simulator (gas and water) was chosen as we are mainly only producing gas and minimal amounts of water from the reservoir interval. In

addition, the geomechanical simulator can only take black oil simulation as an input at this time.

- This type of simulator will allow us to study well pattern placement, completion intervals, infill drilling, and other operations (Mattax and Dalton, 1990).
- An area of the reservoir was chosen where the best production data was available, and on the first/best producing wells in the field was located (RU-1). RU-1 was drilled in 1981 and has had some of the best production in the field.
 - We were limited on the areal extent of the field due to the extremely thick reservoir section and lack of zonal pressure and production data. Therefore, we selected a section (1900ft x 1500ft x 1800ft xyz) that included four wells including RU-1 within the high fold seismic area. This would allow the geomechanical model to be well constrained in an area of the highest quality shear data (figure 3.4 and 3.5).
- The model was constructed using properties from the geostatistical model and the production histories were included.
 - This allowed us to have the most accurate permeability, porosity, and Sw estimates from the geostatistical model, in addition to all of the other important reservoir properties (Young's modulus, Poisson's ratio, density, etc.) that would be needed for the geomechanical modeling.
 - In addition to this, hydraulic fractures were modeled in the production model. This was carried out using higher permeabilities in areas where hydraulic fractures were created. Hydraulic fractures are 100 times more

permeable than the matrix. The direction and half length of these modified permeability zones were taken from micro-seismic studies (Riley, 2007) and the 1D geomechanical Model (Higgins, 2007).

- History matching was carried out.
 - Generally, the reservoir description used in the model is validated by running the simulator with historical production and comparing calculated pressures and fluid movements (Mattox and Dalton, 1990). This type of workflow was carried out on individual wells as a more rigorous test. During history matching, the permeability field and the relative permeability/saturation relationships were manipulated to match individual well pressures.
 - Since this is based on a geostatistical model that is out ‘best educated guess’ the manipulation of these permeability/saturation relationships makes the history match possible. As the model does not match the subsurface perfectly and we have no zonal pressure control.

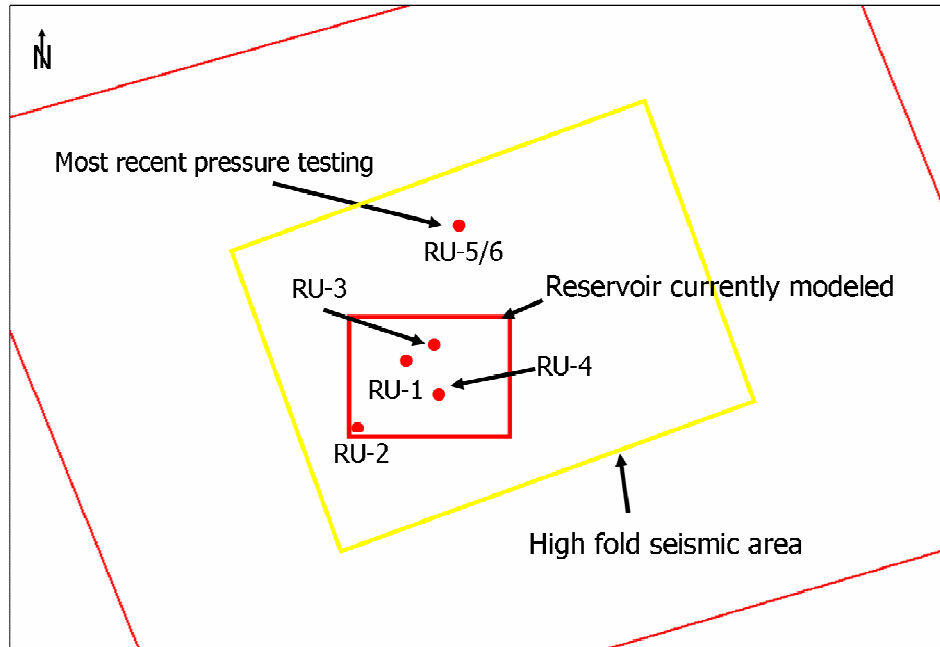


Figure 3.4: Map showing location of the production/geomechanical model and the wells included within the models.

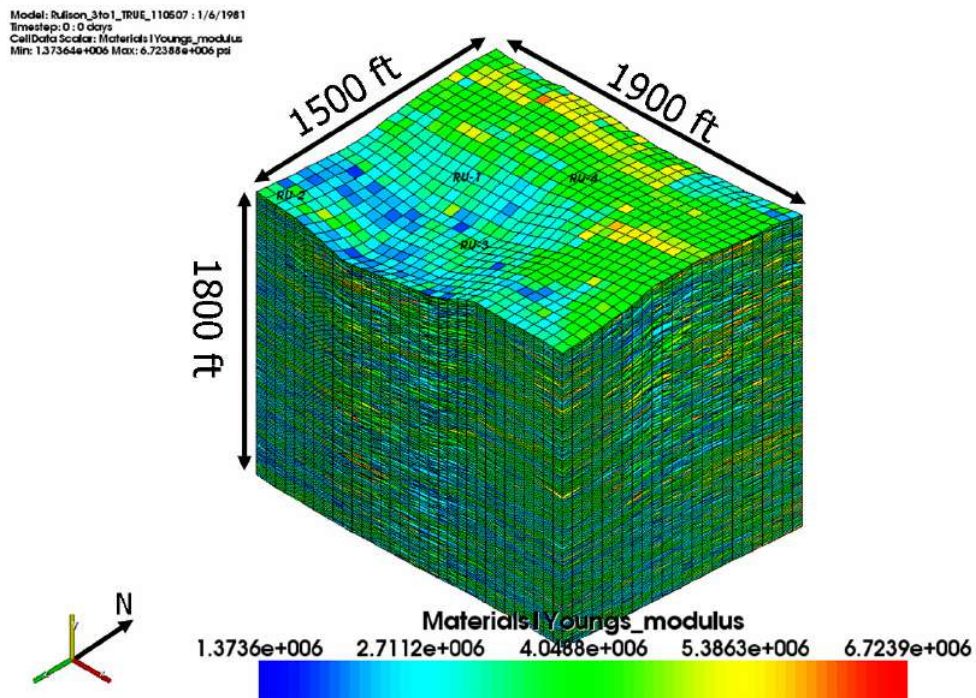


Figure 3.5: Figure showing the scale used for the production/geomechanical models. The property shown is Young's modulus which denotes lithology. Green and higher is sandstone, while the lower values (blues) are shales or sandy shales.

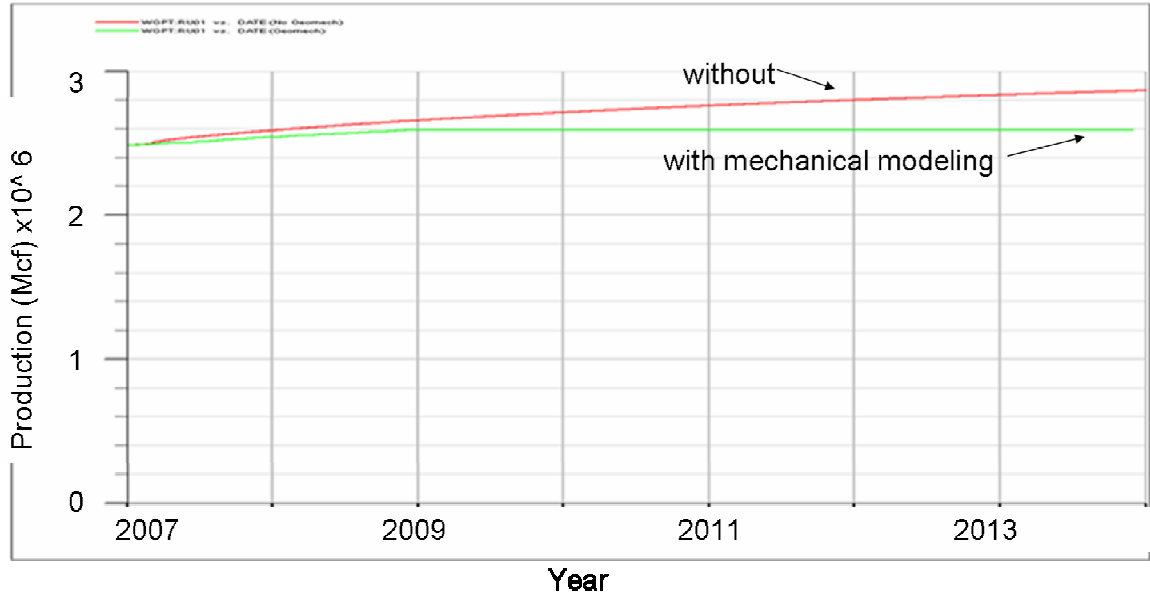


Figure 3.6: Figure showing impact of geomechanics on production. The red line shows the simulation without including the geomechanical model. The green line shows the 3-dimensional geomechanics included in the simulation. This chart applies to model. Courtesy Schlumberger DCS.

It can be seen from figure 3.6 that the geomechanical response over time is expected to have an impact on production, even within these tight low porosity rocks. This response is due to effective stress change within this tight reservoir, and the response of compliant hydraulic fractures modeled high permeability over time with reservoir depletion. These concepts will be gone over in detail in the following chapters which deal with the coupling of the production simulator to the geomechanical model and the results of this study.

CHAPTER 4

GEOMECHANICAL MODELING

4.1 Introduction

As stated in previous chapters, the workflow for building this 3-dimensional geomechanical model has been developed and adapted over the course of this project. What follows in this chapter is an explanation of earth stresses and the context in which they are used in this work, the final and most appropriate workflow that was used, and the inputs for the model. The boundary conditions will be discussed, as will the equations for effective stress calculations from pressure change. This will provide the necessary background for chapter five which deals with the results and implications of the modeling processes and comparisons to seismic research that is ongoing within the RCP study area at Rulison.

4.2 Explanation of Earth Stresses

The goal of this research is to define stress magnitudes in three dimensions and their changes with production. It is necessary to define stresses in the convention we will be discussing them in the following sections. Stresses in the earth will be discussed using the convention of principal stresses; σ_v (σ_{zz}) for overburden stress, σ_H (σ_{xx}) for maximum horizontal stress, and σ_h (σ_{yy}) for minimum horizontal stress. The directions and magnitudes of these stresses are crucial as inputs and boundary conditions for the mechanical model. The overburden was calculated by integrating the bulk density log (equation 4.3 and figure 4.5) and the maximum and minimum horizontal stresses were constrained using results from Higgins, 2006. From these inputs the mechanical model was controlled and run.

Stress is a force per unit area, and the complete stress tensor of an infinitesimally small cube can be visualized using figure 4.1. This stress tensor has three normal stresses and six shear stresses. A rotation can be applied to this tensor which results in the shear stresses going to zero leaving only principle stresses (fig. 4.2 and 4.3). This is what has been carried out here and also by Higgins, 2006. This assumes that the overburden is vertical and horizontal stresses are normal to the vertical stress (Jaeger and Cook, 2007).

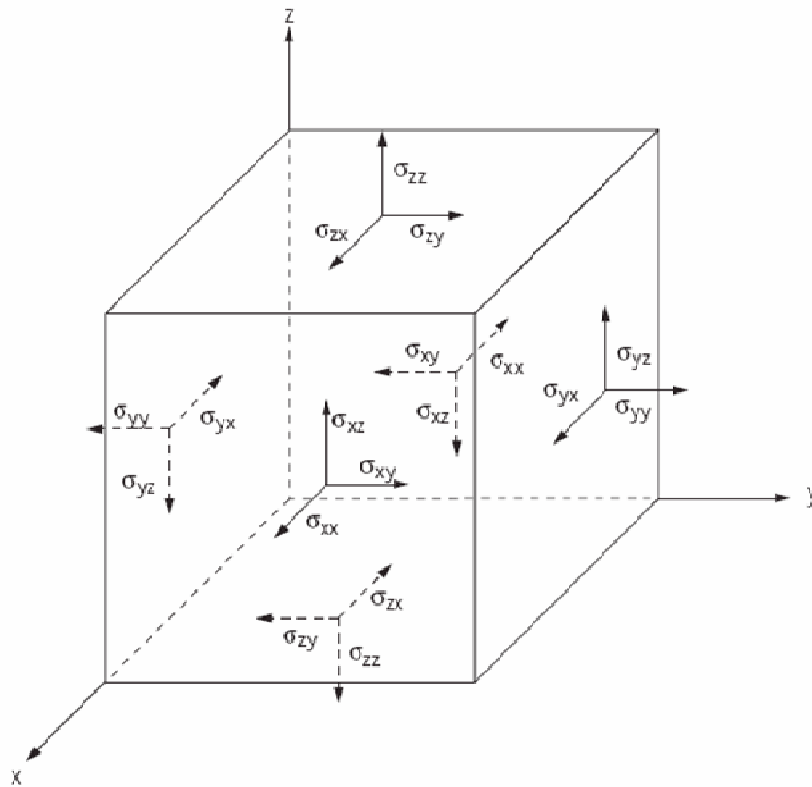


Figure 4.1: Figure showing 3-dimensional stress state in an infinitely small cube.

$$\begin{pmatrix} \sigma_{xx} & \sigma_{xy} & \sigma_{xz} \\ \sigma_{yx} & \sigma_{yy} & \sigma_{yz} \\ \sigma_{zx} & \sigma_{zy} & \sigma_{zz} \end{pmatrix} \text{ or } \begin{pmatrix} \sigma_{xx} & \tau_{xy} & \tau_{xz} \\ \tau_{yx} & \sigma_{yy} & \tau_{yz} \\ \tau_{zx} & \tau_{zy} & \sigma_{zz} \end{pmatrix}$$

Figure 4.2: Complete stress tensor showing two notations

$$\begin{pmatrix} \sigma_{xx} & 0 & 0 \\ 0 & \sigma_{yy} & 0 \\ 0 & 0 & \sigma_{zz} \end{pmatrix}$$

Figure 4.3: Rotated stress tensor that shows zero shear stresses and only principle components.

In the following sections results will be shown from the geomechanical modeling program. The principle stresses shown will be negative, this is due to the fact that the modeling program using the convention of compressional stresses being negative.

4.3 Workflow

A workflow was developed for the building of this 3-dimensional geomechanical model. This workflow starts with the geomechanical modeling, it is implicit that the geostatistical model and history matched production model have been validated and quality controlled before these steps are started. This workflow is unique to Schlumberger proprietary software; although it should be similar to most other loose or partially coupled mechanical simulators available.

- Scale is critical to any modeling that is done. The size of each cell was determined by production modeling. The model was upscaled using pore volume weighted upscaling (fig. 4.4).

$$\bar{\phi} = \frac{(PV)_1}{(PV)_1 + (PV)_2} \phi_1 + \frac{(PV)_2}{(PV)_1 + (PV)_2} \phi_2$$

ϕ = Porosity
 PV = Pore Volume

Figure 4.4: Equation combining two cells porosity in to one. This equation was used as the basis for upscaling the production and therefore, the geomechanical model.

- The equation above took the geostatistical model from 50ft. x 50ft. x 3ft. xyz (1x1 model) to 50ft. x 50ft. x 9ft. (3x1 model).
- This upscaling is appropriate as it matches production from model runs and cuts down on computation time. It also has the added benefit of being very near the seismic bin size of 55ft. x 55ft. The resolution of the model is, however, higher than the resolution of the shear seismic which will be discussed in Ch. 5
- The mechanical modeling program uses the run file from the production model as a basis for mechanical modeling. Therefore, this file must be manipulated to complement the mechanical simulator and the production simulator
 - In this case, ECLIPSE was used with Visage (both marks of Schlumberger)
 - Visage accepts only ECLIPSE 100 (black-oil or two-phase) commands, with no local grid refinement. This means that hydraulic fractures are modeled as modified permeabilities according to the half-lengths, directions and heights shown by micro-seismic and one-dimensional geomechanical modeling (Higgins, 2006 and Riley, 2007).

- The ECLIPSE run file must be modified to exclude the rock properties files (Young's modulus, rock density, and Poisson's ratio) while the Visage file must have these available.
- After the ECLIPSE file is manipulated and directory structures built, the boundary conditions, initial condition, and type of model used are input, this is the focus of the next section.
- Once the model run is completed, the results must be appended to the grid using VisGen, which is Visage's graphical visualization tool.
 - Results are viewed and calculations can be made using the calculator function which is critical in this case where we are comparing results to time-lapse seismic.
 - Since we have a loose idea of what we are expecting, we looked for realistic results in pressures and effective stresses. This step is where adjustments to inputs were made and the model was run again.
- This is an iterative process that required many model runs before an acceptable model is constructed. The results shown in following chapters are the result of months of modeling runs.

4.4 Inputs and Boundary Conditions

The inputs and boundary conditions were built based on available data. First the boundary conditions will be explained, and then the inputs for the mechanical model will be explained below.

Boundary conditions were constructed using available data on Rulison field from Higgins, 2006, the available MWX data, and information provided by Williams production company. The boundary conditions were constructed as follows.

4.4.1 Soil effective weight

$$\sigma'v = \sigma v - Pp \quad (4.1)$$

$$\text{Soil effective weight} = \sigma'v / \text{depth} \quad (4.2)$$

Where: $\sigma'v$ = Effective overburden
 σv = overburden stress
 Pp = Pore pressure

Pore pressure was constructed using a gradient of .433 psi/ft to 5000 ft. and then a gradient of 1.01 psi/ft from Williams modeling done on pilot pressure tests in the SW of the RCP study area. Overburden was constructed by integrating the bulk density log from RU-5 using equation 4.3 and figure 4.5:

$$\sigma_v = \int_0^z \rho g dz \quad (4.3)$$

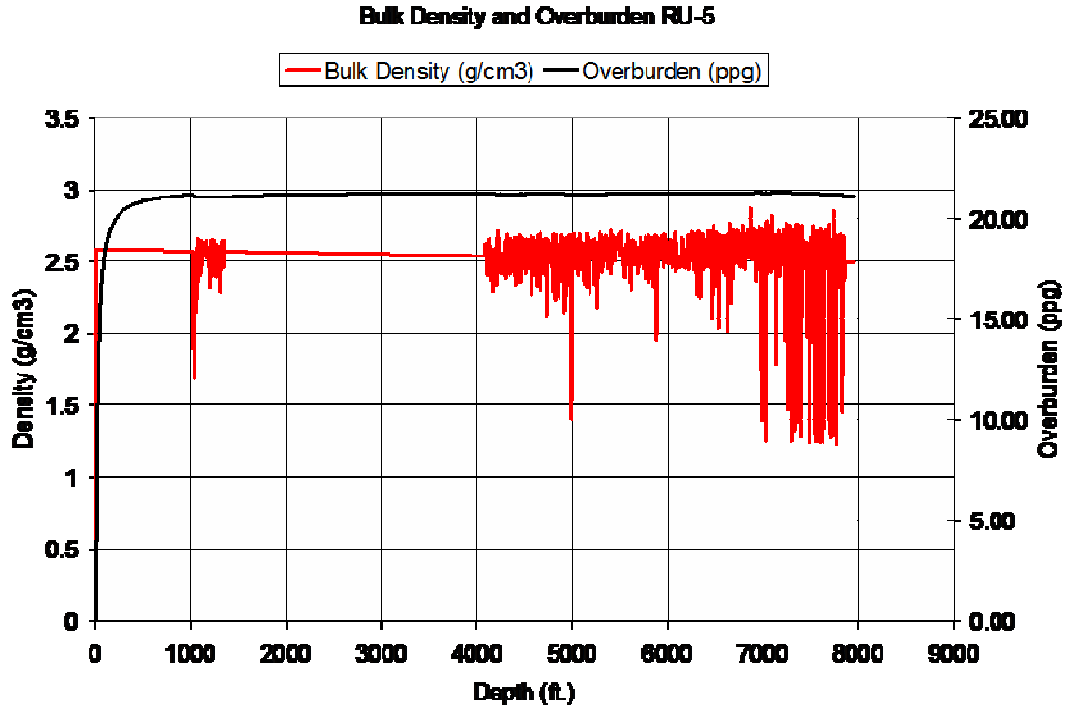


Figure 4.5: Figure showing integration of overburden. The density log was not run to the surface; therefore a linear extrapolation was used.

The next step in building the boundary conditions is constructing the minimum and maximum horizontal stress coefficients. They were constructed as follows.

4.4.2 Maximum Horizontal Stress Coefficient

$$\sigma'H = \sigma_H - P_p \quad (4.4)$$

$$\sigma_H \text{ coeff.} = \sigma'H / \sigma_v' \quad (4.5)$$

Where: $\sigma'H$ = Effective maximum horizontal stress magnitude
 σ_H = Maximum horizontal stress magnitude
 σ_H coeff. = Maximum horizontal stress coefficient
 σ_v' = Effective overburden
 P_p = Pore pressure

Magnitudes of maximum horizontal stresses were taken from work done by Shannon Higgins and mini-fracture results from well RU-5.

4.4.3 Minimum Horizontal Stress Coefficient

$$\sigma'h = \sigma_h - P_p \tag{4.6}$$

$$\sigma_h \text{ coeff.} = \sigma'h / \sigma'v \tag{4.7}$$

- Where:
- $\sigma'h$ = Effective minimum horizontal stress magnitude
 - σ_h = Minimum horizontal stress magnitude
 - $\sigma_h \text{ coeff.}$ = Minimum horizontal stress coefficient
 - $\sigma'v$ = Effective overburden
 - P_p = Pore pressure

Magnitudes of minimum horizontal stresses were taken from work done by Shannon Higgins and mini-fracture results from well RU-5.

Once these values were compiled, they were decimated so values were taken every 100 ft. This made a smoother boundary condition to avoid any anomalies caused by irregular boundary conditions. These were input into Visage as boundary conditions. The figure below shows the graphical representation of what was input into the mechanical modeling program.

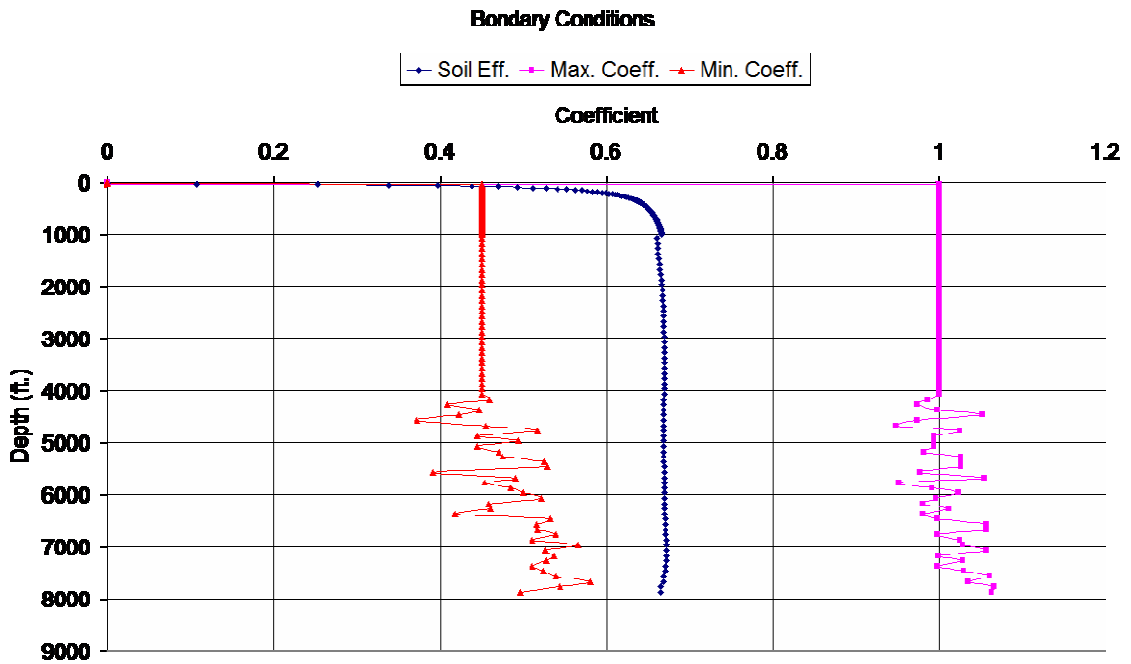


Figure 4.6: Chart showing boundary conditions as input into the mechanical modeling program.

Parameter	Input	Unit	Source
Young's modulus	ECLIPSE	psi	Geo-statistical model
Poisson's ratio	ECLIPSE	dimensionless	Geo-statistical model
Blot's coefficient	0.7	dimensionless	Rock physics
Thermal Expansion coefficient	9.0 e -06	1/F	default
Pressure	ECLIPSE	psi/ ft	Higgins, 2006 and Williams
Max horizontal stress coefficient	see above	dimensionless	
Min horizontal stress coefficient	see above	dimensionless	
Soil effective weight	see above	psi/ ft	
Horizontal Stress azimuth	98	degrees	see below
Vertical Stress Inclination	90	degrees	see below
Failure Criterion	Mohr-Coulomb		see below
Cohesion	1.45 e 21	psi	default
Friction angle	30	degrees	default
Dilatation angle	5	degrees	default
Tensile stress cut-off	1.45 e 21	psi	default
Material fluidity	1	dimensionless	default
Hardening/Softening coefficient	0	dimensionless	default
Permeability	ECLIPSE	mD	Geo-statistical model
Porosity	ECLIPSE	%	Geo-statistical model
Water Saturation	ECLIPSE	%	Geo-statistical model

Table 4.1: Table showing inputs for mechanical modeling and their sources.

4.4.4 Inputs

The above table shows all of the mechanical inputs for the mechanical modeling program. Biot's coefficient is modeled at 0.7 due to the exceptionally hard, low porosity nature of these rocks. This number is taken from previous rock physics work on low porosity sands (Hoffman, et. al., 2005). The horizontal stress azimuth and vertical inclination were chosen as shown below.

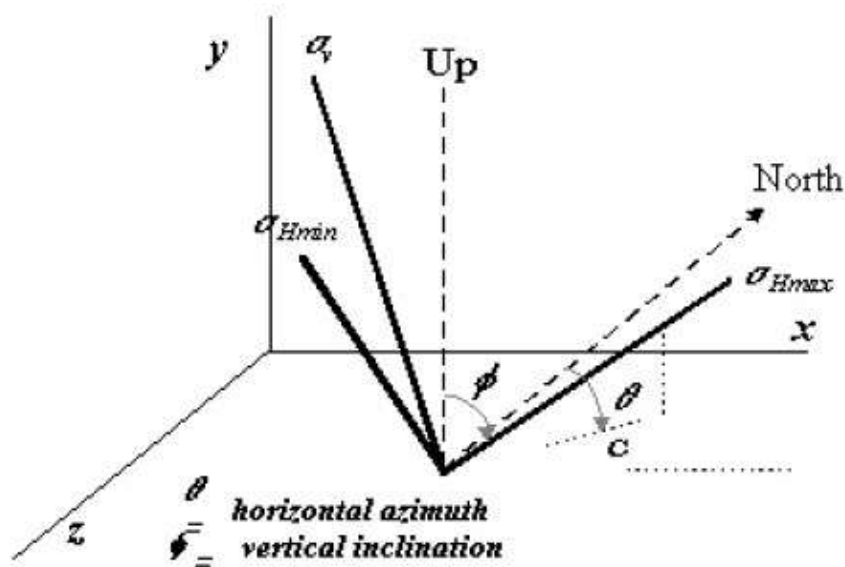


Figure 4.7: Figure showing convention of horizontal stress azimuth and vertical inclination. From VisGen manual.

The horizontal stress azimuth is taken from the image logs. In this case the input is 98 degrees from North, as shown in figure 1.9 and 3.2. The vertical inclination is the angle the maximum principle stress is inclined to the vertical, Φ . Since overburden is the maximum principle stress the inclination is 90 degrees. This is acceptable as drilling induced fractures are vertical on average in image logs at depth (Matesic, 2006).

Mohr-Coulomb failure criterion was chosen, however, in this situation it is elastic, as we never move into the failure stress specified. Due to the hard nature of these rocks,

failure is never reached, nor is plastic deformation, and the inputs for the failure criterion are essentially never used. For more on Mohr-Coulomb and effective stresses please see Jaeger and Cook, 2007.

4.5 Pressure Related to Effective Stress

Visage is the mechanical simulator used to construct this model (Visage is a mark of Schlumberger). Visage is a finite element modeling program that utilizes the explicit method for geotechnical work, advanced engineering problems, and geomechanics. In 'explicit' methods, displacements at a time-step are evaluated in terms of the accelerations and displacements of the previous time-step. In 'implicit' methods, displacements at a time-step are dependent on the accelerations at that step. Determinations of displacements then require iterative numerical techniques at each step (Visage manual). Finite element modeling is a complex topic and will not be gone over in detail in this work. For a complete overview please see Lin, 2003.

The coupling from the production model to the mechanical model is proprietary, and will not be shown; however, representative equations will be discussed in this section. These equations relate pore pressure change to effective stress changes in the earth. Effective stress changes are highest in magnitude closest to the wellbore. This is expected as this location is where the highest permeabilities are modeled, and where the highest pressure change occurs. This description is taken mainly from Jaeger and Cook, 2007 and Thiercelin, 1994.

This stress model is essentially based on linear elasticity and assumes that rock is a semi-infinite isotropic poro-elastic medium subjected to gravitational loading

(Thiercelin, 1994) and horizontal strains are the product of initialization of the boundary conditions from above. This results in the following equations for principle stresses.

4.5.1 Stress Equations

Overburden stress in this case is a principle stress, and this vertical stress is essentially a result of the overburden and pore pressure.

$$\sigma_v = S_v - \alpha P_p \quad (4.8)$$

Where: σ_v = Effective overburden stress
 S_v = Overburden stress
 α = Biot's constant
 P_p = Pore pressure

$$\sigma_{h \min} = \frac{\nu}{1-\nu} (S_v - \alpha P_p) + \frac{E}{1-\nu^2} \epsilon_{H \min} + \frac{E\nu}{1-\nu^2} \epsilon_{H \max} + \alpha P_p \quad (4.9)$$

Where: S_v = Overburden stress
 $\sigma_{h \min}$ = Effective minimum horizontal stress
 ν = Poisson's ratio
 E = Young's modulus
 P_p = Pore pressure
 $\epsilon_{H \min}$ = Minimum horizontal strain
 $\epsilon_{H \max}$ = Maximum horizontal strain
 α = Biot's constant
 P_p = Pore pressure

$$\sigma_{H \max} = \frac{\nu}{1-\nu} (S_v - \alpha P_p) + \frac{E}{1-\nu^2} \epsilon_{H \max} + \frac{E\nu}{1-\nu^2} \epsilon_{H \min} + \alpha P_p \quad (4.10)$$

Where: S_v = Overburden stress
 $\sigma_{H \max}$ = Effective maximum horizontal stress
 ν = Poisson's ratio
 E = Young's modulus
 P_p = Pore pressure
 $\epsilon_{H \min}$ = Minimum horizontal strain
 $\epsilon_{H \max}$ = Maximum horizontal strain
 α = Biot's constant
 P_p = Pore pressure

The dependence of horizontal stress on rock lithology results from the dependence of Poisson's ratio on rock lithology. If the uniaxial strain assumption is relaxed and uniform (vs. depth) anisotropic strain is added, the elastic model is what is shown above (Thiercelin, 1994). Above, a dependence of Young's modulus is shown, therefore, the higher the Young's modulus, the higher the horizontal stress. This model gives a better qualitative description of the state of stress measured in an area where compressive tectonic stresses are suspected (Thiercelin, 1994). It is also of importance to note that if the strains are reduced to zero, this model fulfills the uniaxial strain model.

The model shown above is the best representation that is available for the type of calculations performed by the geomechanical modeling program. It is important to note the effective stress dependence on pressure. This is critical in assessing the results of this model, and will give a better insight into the seismic signature as well. With the geology of the area being extremely hard, low porosity rocks, effective stress change will occur only where pressure changes. This implies the maximum effect is adjacent to natural and hydraulic fracture closure. No plastic behavior or failure is assumed in this situation. The next chapter deals with the results of this model and comparisons to seismic data.

CHAPTER 5

MODELING RESULTS

5.1 Introduction

This chapter deals with the well chronology, results of the modeling process, correlation to seismic, and a sensitivity analysis of the inputs into the model. It also shows how principal effective stresses have changed with production, and how these pressure and effective stress changes relate to seismic. More importantly, correlations are shown between pressure and effective stress changes for both the 03-04 and 03-06 time-lapse survey data. This also illustrates how time-lapse S22 impedance (velocity of slow shear in reservoir averaged direction) is indicative of pressure depletion and effective stress change.

5.2 Well Chronology

It is necessary to show the timeline of wells drilled within the model and the timing of their drilling and completion. This is required as the times of drilling and the times of the time-lapse monitor surveys is important in upcoming sections. The time-lapse surveys are as follows:

- 2003 Base Survey
- 2004 Monitor
- 2006 Monitor

The seismic data has been analyzed by fellow students, and the results that are used are from their respective work at Rulison. Shown in following sections will be work from Rumon, 2006 and Meza, in progress. For complete details on seismic processing, cross-equalization, and filtering please reference the above work. The wells that are in the model and their locations are shown in figure 5.1.

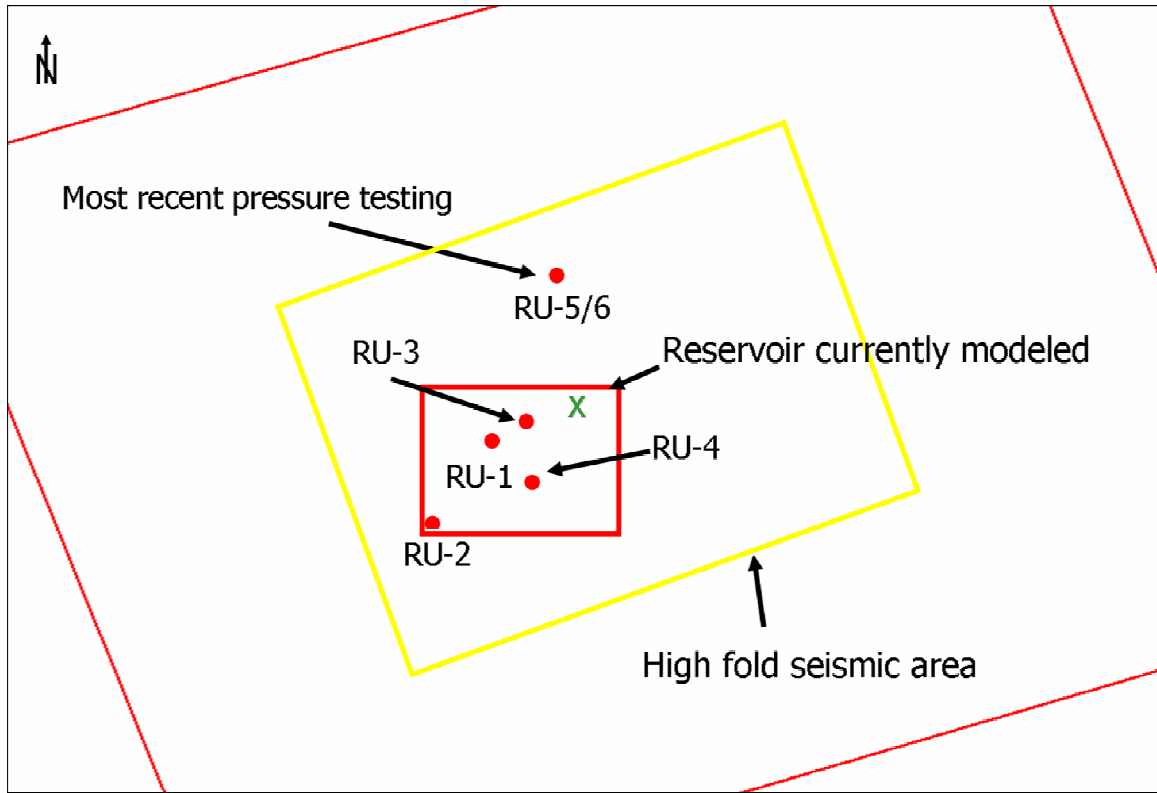


Figure 5.1: Location of wells with respect to geomechanical model inside high fold seismic area. Red outer box is the RCP survey site. Green X in NE corner of mechanical model is location of data in model compared to RU-5 mini-fracture test.

The timing of the wells inside the geomechanical model is as follows:

- RU-1 drilled and completed in 1981
- RU-1 re-completed in 1995
- RU-2 drilled 1997
- RU-3 drilled 2005
- RU-4 drilled 2005
- RU-5 drilled and zonal pressure tested (Ch.2) 2006

Several important points should be made at this time. In relation to the 2003-2004 seismic survey in the geomechanical model, there was very little production, as RU-1 and RU-2 have been producing since 1981 and 1997 respectively. Therefore, shear seismic change in the model area is low during this time (Rumon, 2006) due to low pressure change and therefore low stress change. In these tight sands, it can be seen from

production data and the production model that the majority of pressure drop (average pressure within model boundaries) occurs due to new wells and re-completions. After this time the ellipse of drainage caused by the hydraulic fracturing process is drawing from the far field, which is controlled by low porosity tight rocks and hydraulic fracture conductivity degradation through time. This pressure change in the production model drives responses in the geomechanical model. From the production models overall pressure change, we can see this timeline in a physical sense.

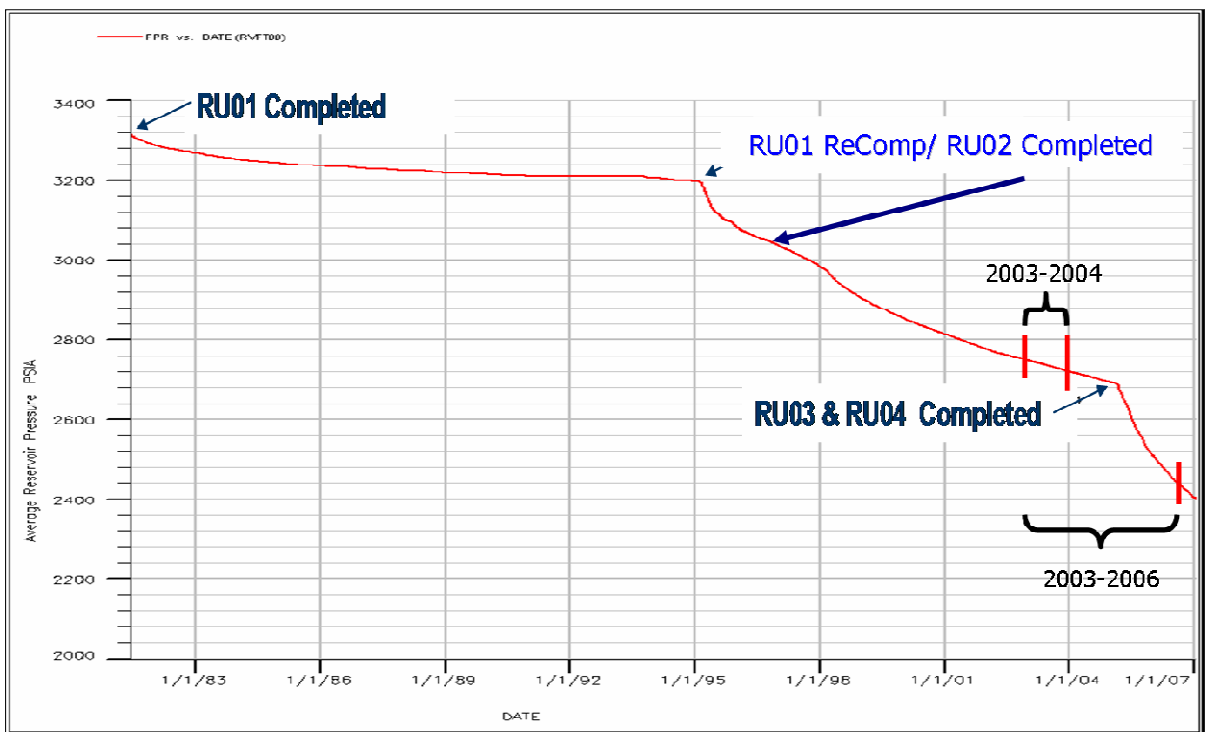


Figure 5.2: Chart highlighting average pressure within the production model with drilling events and time-lapse seismic surveys. The y-axis shows pressure in psia and the x-axis shows the date. Courtesy of Schlumberger DCS Denver.

From figure 5.2 it can be seen that the pressure drop (and therefore stress change) is most dramatic at times of wells being drilled or re-completions (hydraulic fracturing to increase production long after initial fracturing at time of drilling). Within the model

area, the most change occurs from 2003-2006 due to the drilling of RU-3 and RU-4 in the monitor period within the model. This is shown in section 5.3.4.

5.3 Results

The results of the modeling can be viewed in several ways; first the graphical results are shown, then the 3-dimensional representation of that data, and finally the 3-dimensional data shown correlating to the seismic visually. It is shown that as pore pressure decreases in the model the effective stress increases as the rock matrix supports more of the load.

5.3.1 Graphical Representation

Shown below in figure 5.4-5.6 are the effective stress states around well RU-1 from the initial state in 1981, the time of the first seismic survey in 2003, and the two surveys in 2004 and 2006 at three different depths.

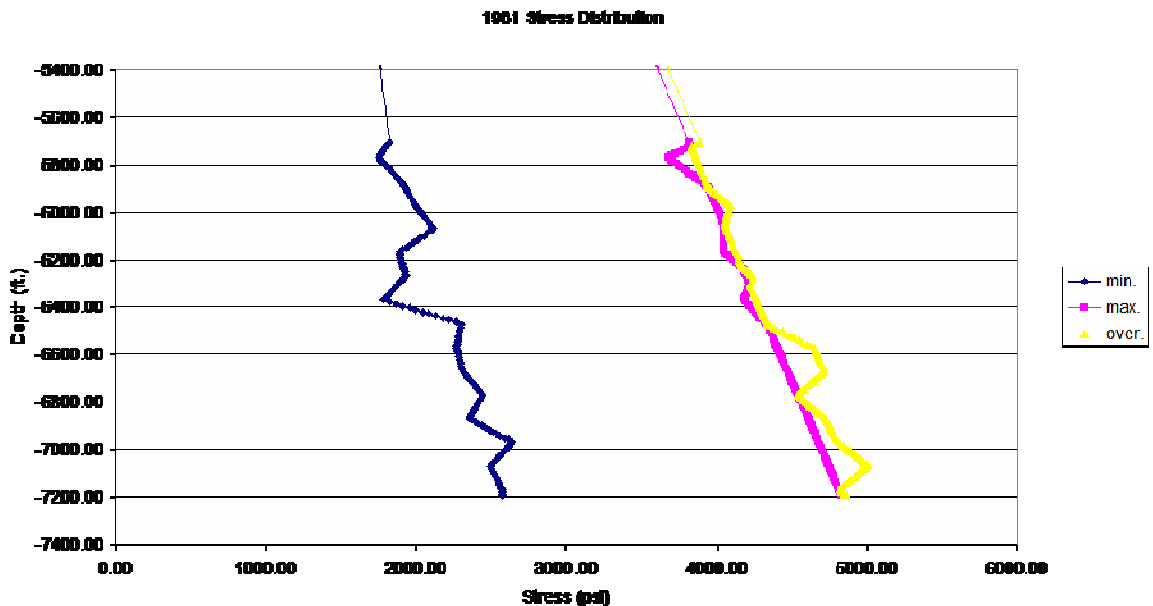


Figure 5.3: Chart showing stress distribution at well RU-1 in 1981. The stress profile at this time is the initial distribution which is a product of the boundary conditions.

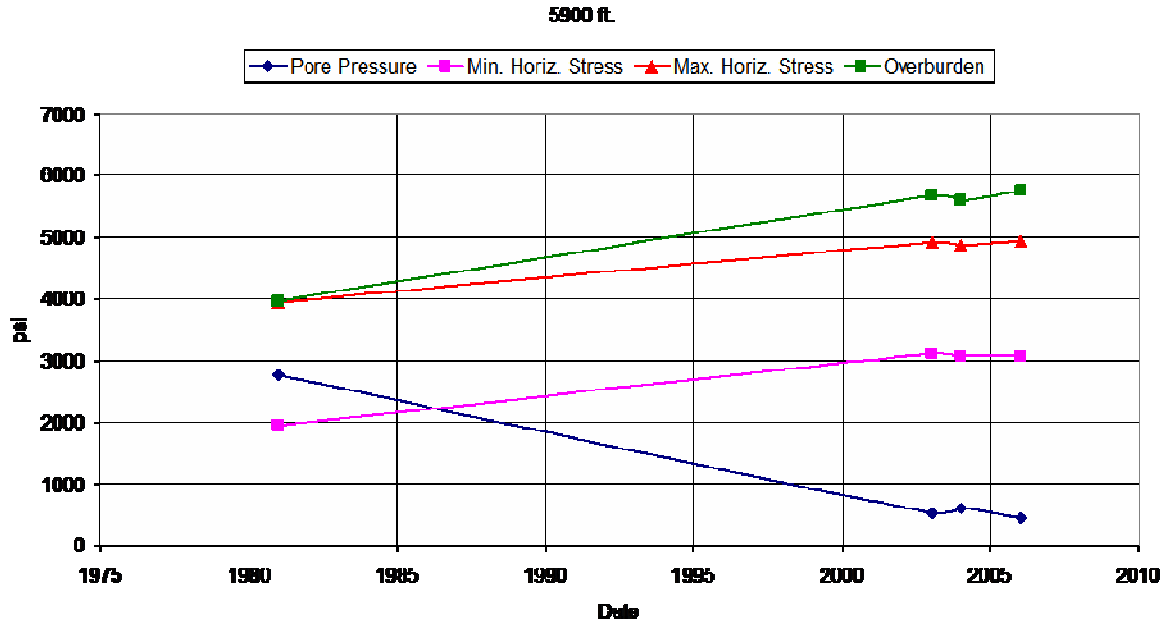


Figure 5.4: Pore Pressure and effective stress change through time at 5900 ft. depth at well RU-1. Please note that these are effective stresses, which is why pore pressure is higher than min. horiz. stress in 1981.

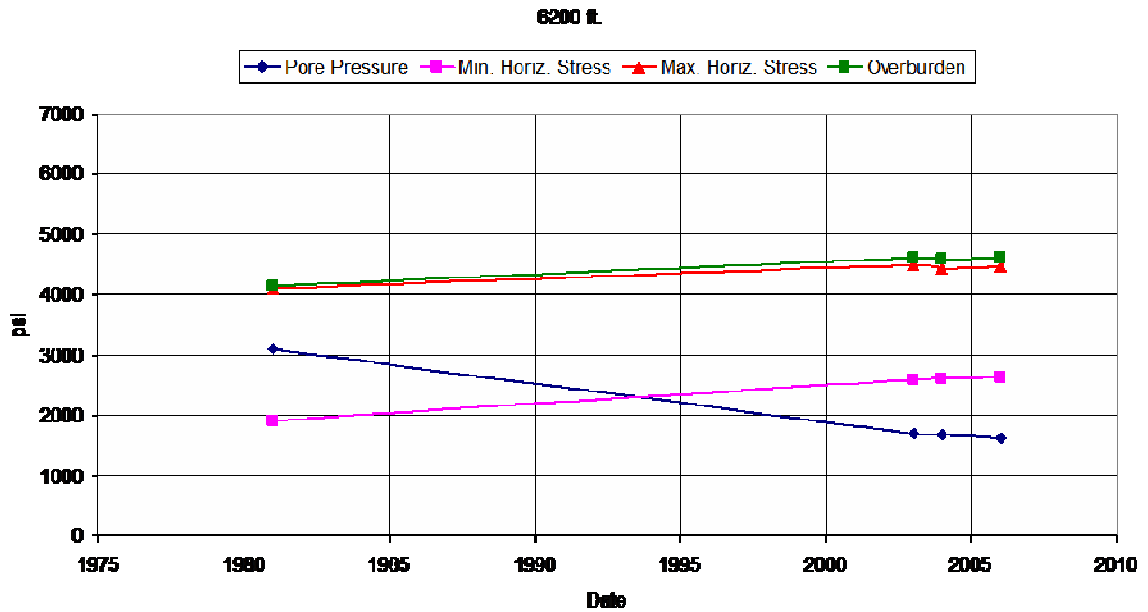


Figure 5.5: Pore pressure and effective stress change through time at 6200 ft. depth at well RU-1. Please note that these are effective stresses, which is why pore pressure is higher than min. horiz. stress in 1981.

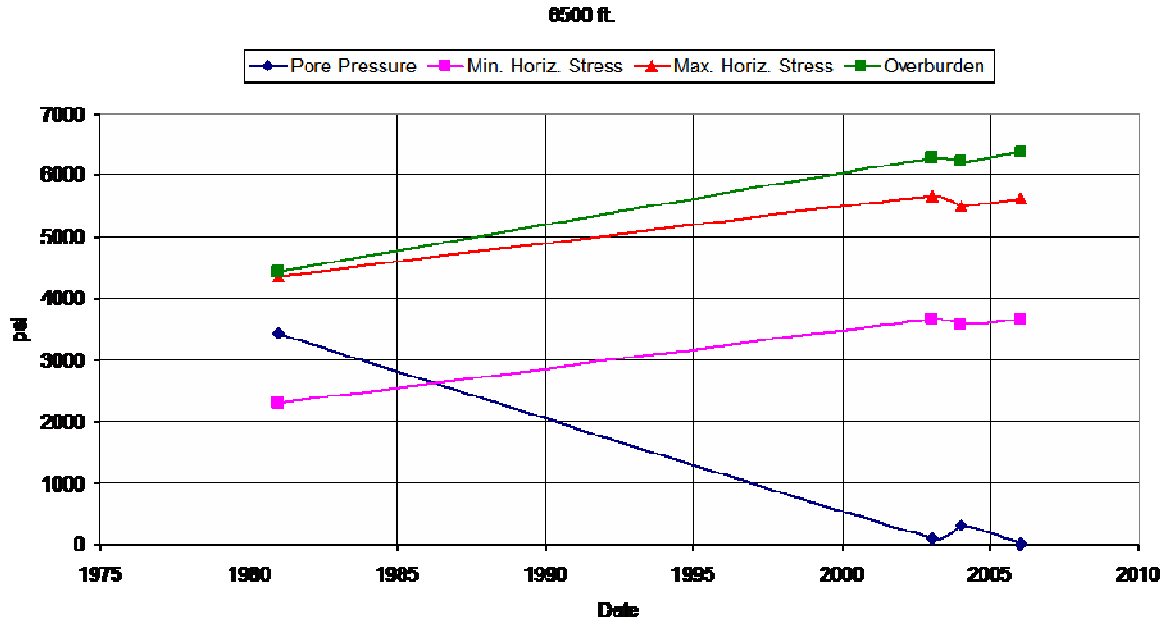


Figure 5.6: Pore pressure and effective stress change through time at 6500 ft. depth at well RU-1. Please note that these are effective stresses, which is why pore pressure is higher than min. horiz. stress in 1981.

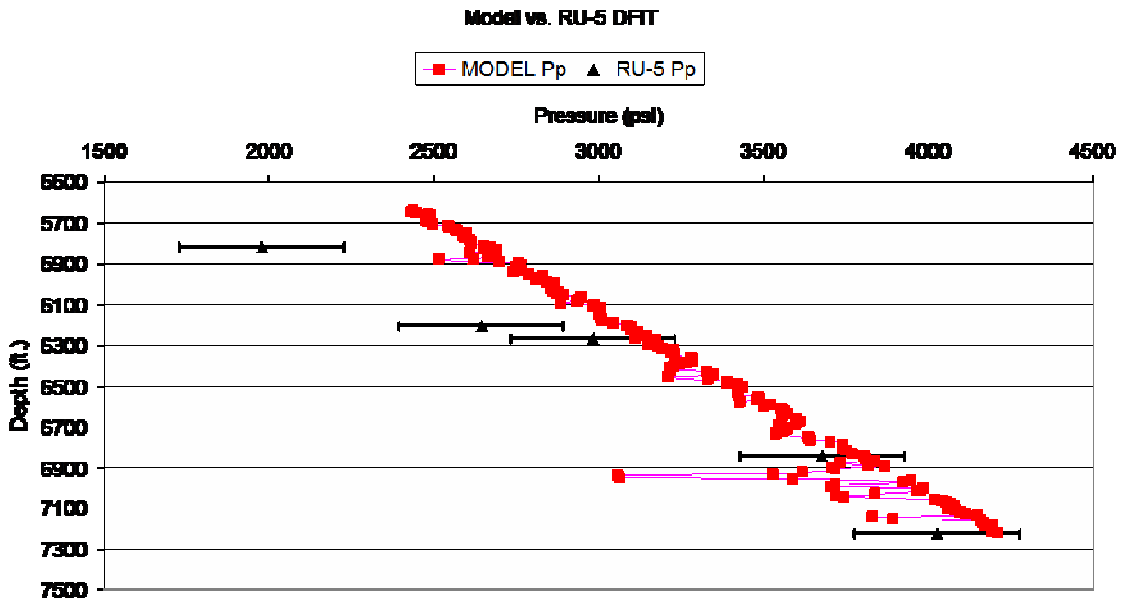


Figure 5.7: Model pressure with depth showing results from mini fracture tests in well RU-5.

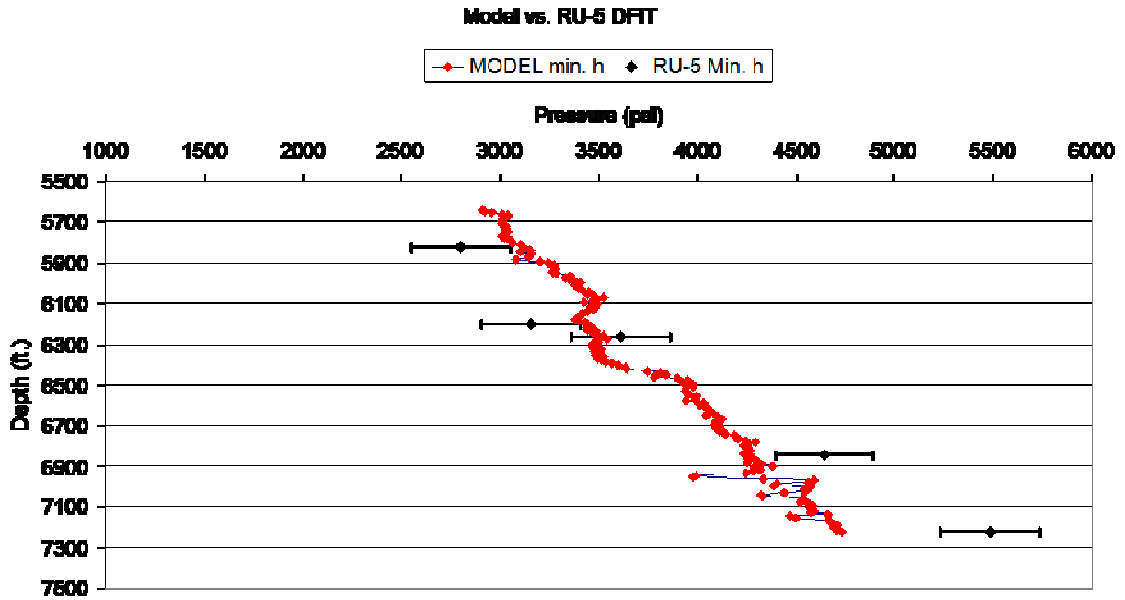


Figure 5.8: Model minimum horizontal stress vs. mini fracture tests at RU-5

The graphs above highlight the nature of stress change with production. This change is dependent on several rock characteristics (Young’s modulus which is a lithology indicator, rock density, and Poisson’s ratio) and also the location of permeabilities, pressure change, and hydraulic fracture location. It can be seen that effective stresses increase over time and production. Please note also the variation of stress change with depth. This shows that depletion is not constant over the reservoir interval, which is that different depths experience varying levels of stress and pressure change. This physical characteristic is highlighted in the 3-dimensional visualization as well. This increase is the result of over 25 years of production from well RU-1. This lowered pore pressures which increased the effective stress, as the rock matrix is now responsible for supporting more load.

Shown below the graphs of stress at RU-1 (fig. 5.7 and 5.8) are pressure and minimum horizontal stress profiles at the northeast corner of the model (see fig. 5.1 for

location). This was done as this was the closest point to well RU-5 where the aforementioned mini-fracture test was completed. Well RU-5 is 1200 ft away at reservoir depth from the stress profile taken from the model. The stress profile was taken in September 2006 of the model while the mini-fracture test was completed in the end of June 2006. This time difference is acceptable as this corner of the model has seen little to no change in this time period due to its distance from producing wells. The method we are using is the most reasonable one available at this time. It can be seen that for pressure 60% of mini-fracture results fall within acceptable error and for stress 80% fall within the acceptable errors. The error bars on the mini-fracture test are set at 250 psi (Bratton, personal communication).

The mini-fracture tests pressures differ from the model at the upper portion of RU-5; this is due to this area of the reservoir being partially depleted by a nearby well (Ch. 2) and more connective channels present near the top of the Williams Fork (Cumella and Ostby, 2003). In addition to this, the mini-fractures minimum horizontal stress measurements below 6800 ft. are much higher than the model predicts. Well RU-5's proximity to an interpreted fault (fig. 5.9) could be the cause of this. For a full report on micro-seismic analysis please see Riley, 2007.

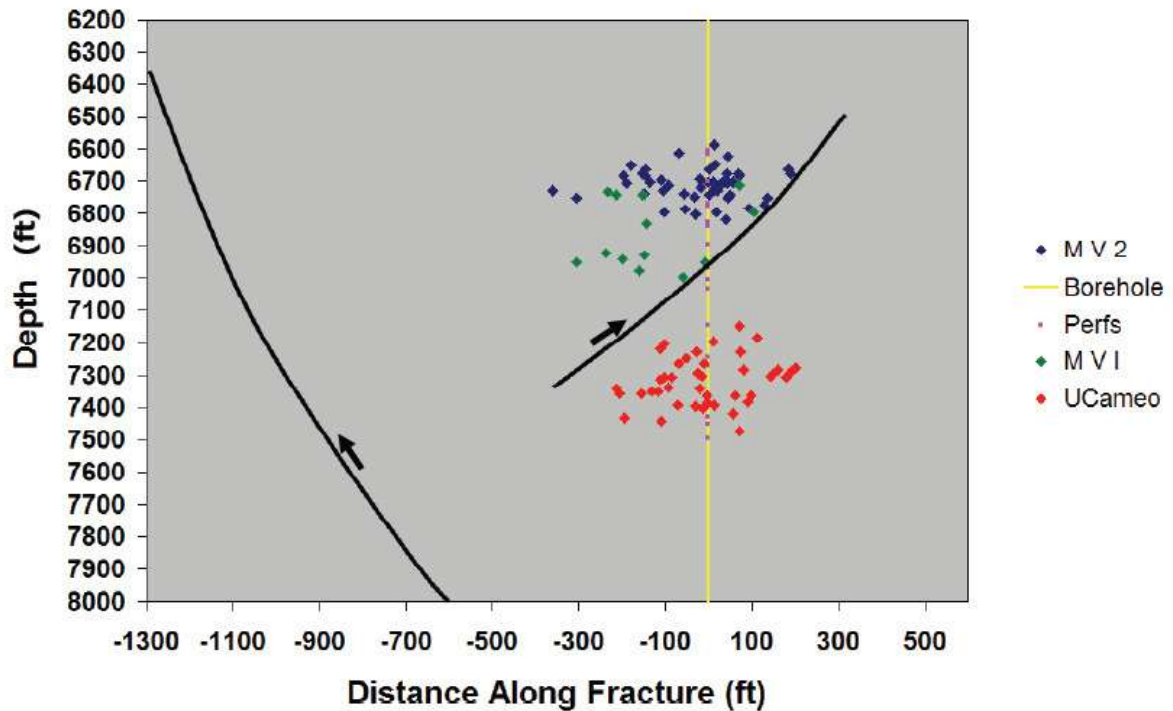


Figure 5.9: Chart showing micro-seismic events at well RU-5. This well was also pressure tested before fracturing (Ch.2). It can be seen that micro-seismic events terminate at the interpreted fault (black lines and arrows). This fault system could also cause some of the anomalously high stress values seen in the mini-fracture results at the same depth (fig. 5.8). Figure from Riley, 2007.

5.3.2 3-Dimensional Representation

When shown in 3D, the relationship between pressure and effective stress change becomes much more apparent. First it is shown how the geomechanical simulator handles geology. There is no lithology discrimination in the mechanical simulator; however, variations in Young's modulus correlate to lithology (fig. 5.10). This is a very important point; Young's modulus describes lithology, and is a proxy for porosity and permeability. Where shales are modeled there is effectively no porosity, no permeability, and 100% water saturation. What this implies is that no gas flow will occur in shales (pressure drop); however, effective stress change may occur from loading changes from above and below.

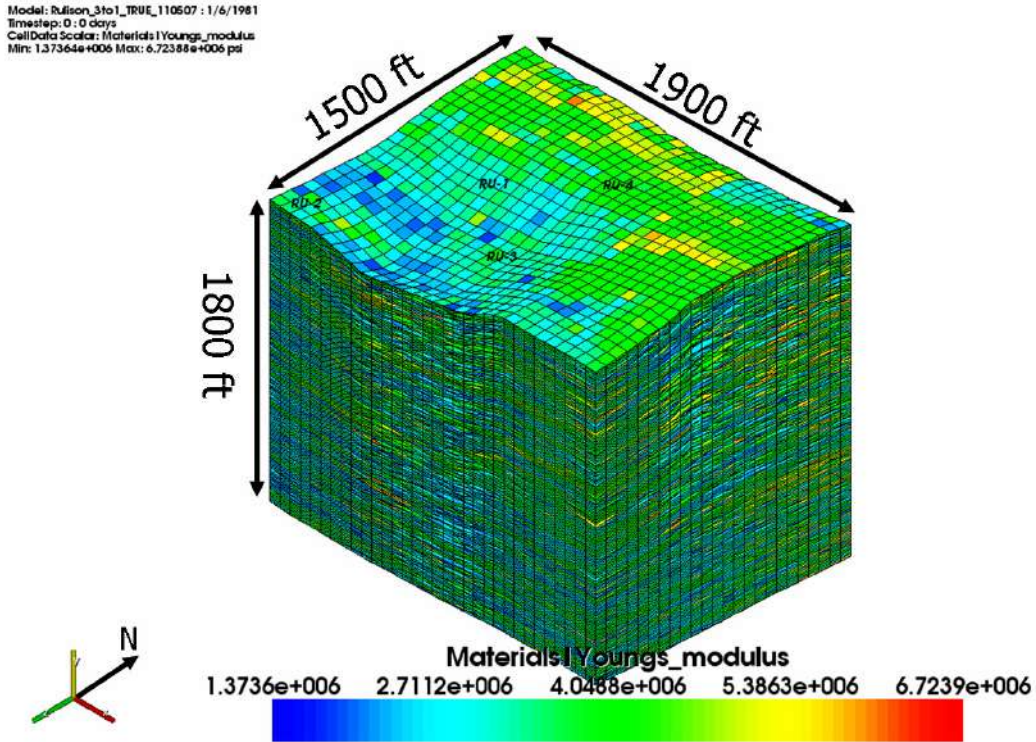


Figure 5.10: 3-dimensional representation of geomechanical model showing Young's modulus distribution. This is a lithology discriminant, 4.048 e+006 psi and above is sandstones, and below is shales and transition zone (shaly sands).

Where Young's modulus is modeled, it is a control on pressure change and permeability distributions. Although permeability and water saturations can be modified for production modeling, this distribution of Young's modulus has a large impact on future modeling. Next, slices of depth looking down in map view will be shown. These pressures are relative from 2003-2004 and 2003-2006. This will highlight pressure and effective stress differences between the respective time-lapse surveys and seismic analysis that has already been completed. Absolute pressures and effective stresses (overburden or third principle) through time are shown below at 1981, 2003, 2004, and 2006.

Model: Rulison_3to1_TRUE_110507 : 1/6/1981
Timestep: 0 : 0 days
Cell Data Scalar: pressure
Min: 23.48.11 Max: 4325.88 psi

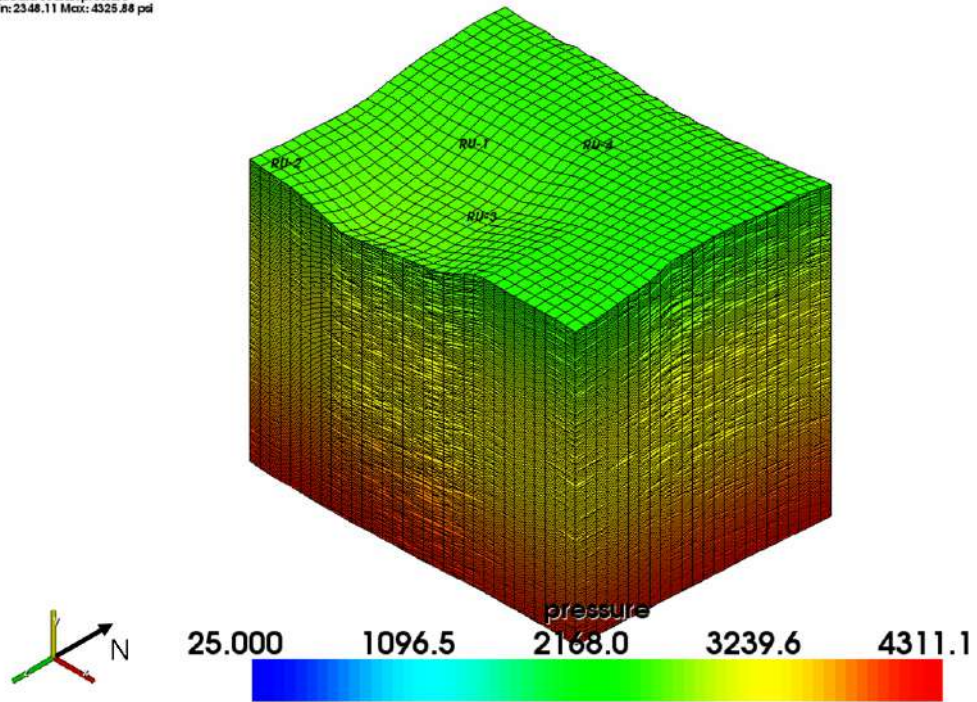


Figure 5.11: Absolute pore pressure in 1981 for entire model. This is a product of the linear gradient used to model pressure.

Model: Rulison_3to1_TRUE_110507 : 1/10/2003
Timestep: 269 : 8157 days
Cell Data Scalar: pressure
Min: 93.2036 Max: 4316.03 psi

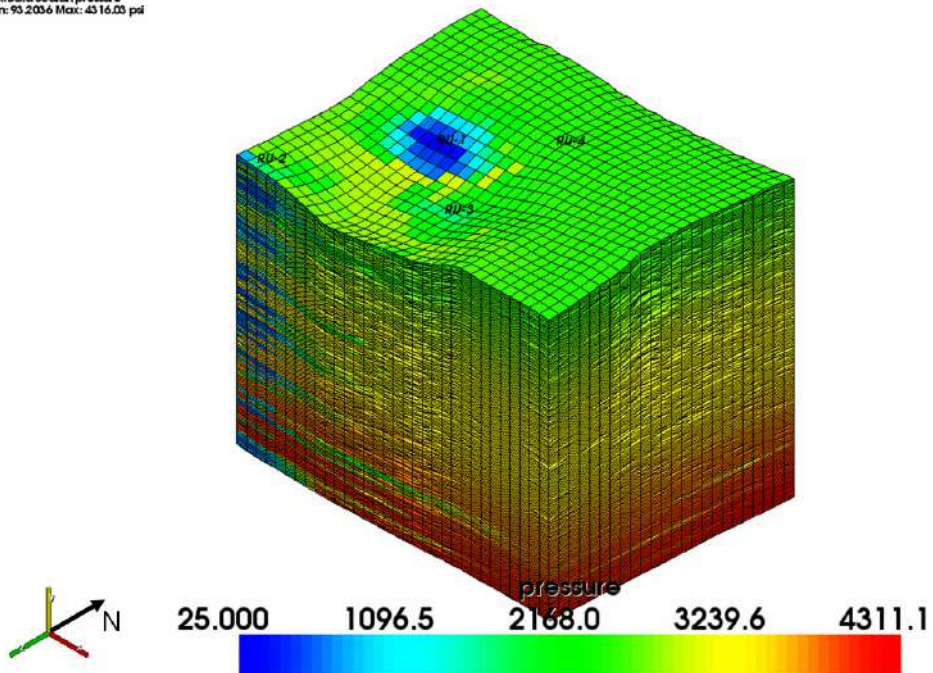


Figure 5.12: Absolute pore pressure in 2003 for entire model.

Model: Rutison_3to1_TRUE_110507 : 1/9/2004
Timestep: 260 : 6493 days
Cell Data Scalar: pressure
Min: 0.122775 Max: 4311.08 psi

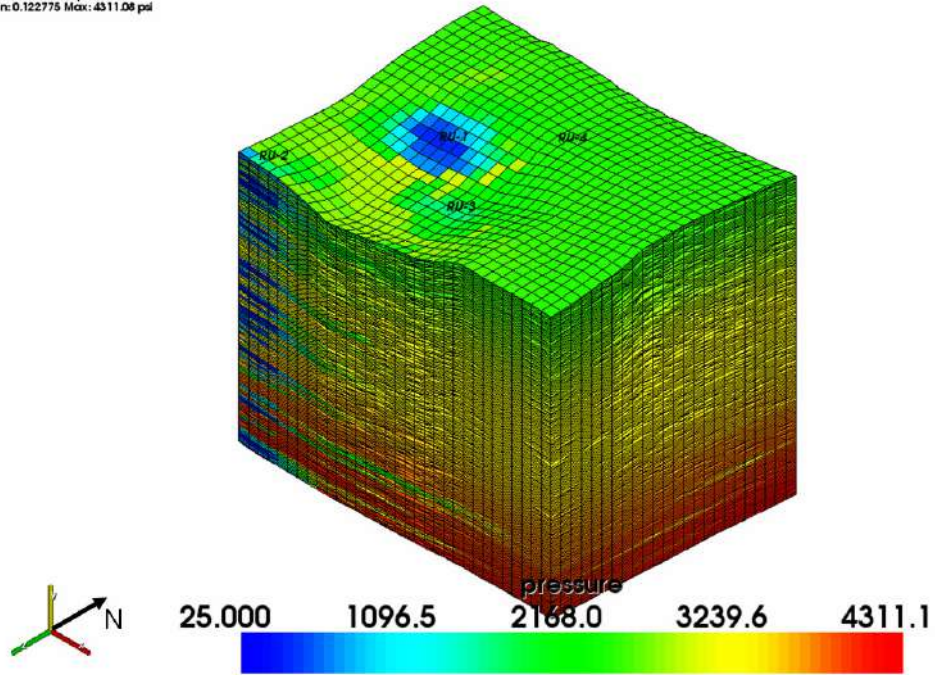


Figure 5.13: Absolute pore pressure in 2004 for entire model. Please note the far field depletion at depth.

Model: Rutison_3to1_TRUE_110507 : 1/8/2006
Timestep: 304 : 9192 days
Cell Data Scalar: pressure
Min: 0.122112 Max: 4311.08 psi

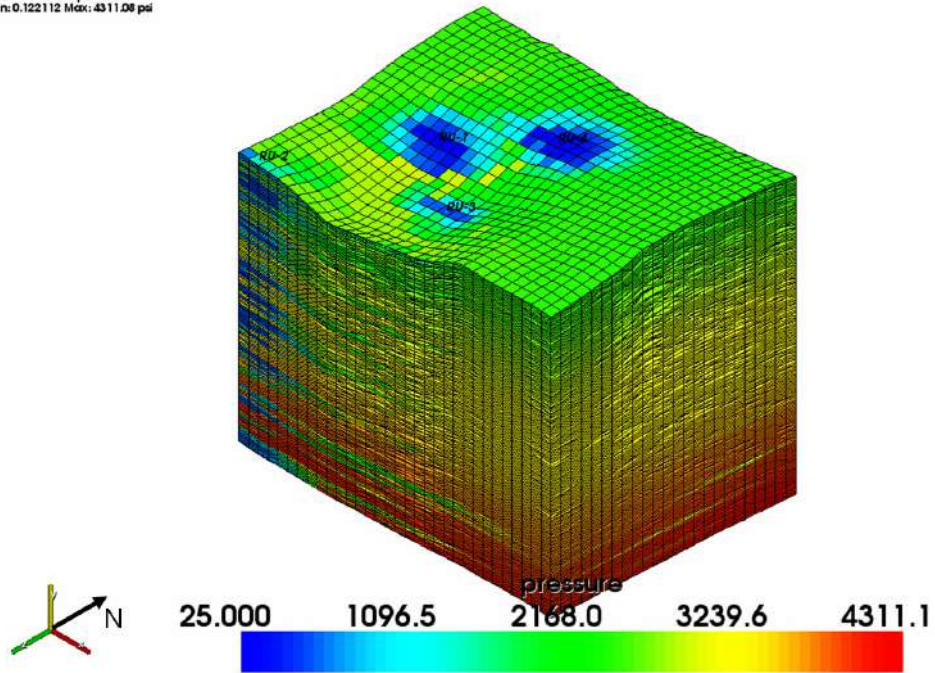


Figure 5.14: Absolute pore pressure in 2006 for entire model. Note location of new wells

Model: Pullson_3to1_TRUE_110507 : 1/6/1981
Timestep: 0 : 0 days
Cell Data Scalar: Stress3d(p3)
Min: -5020.99 Max: -3703.73 psi

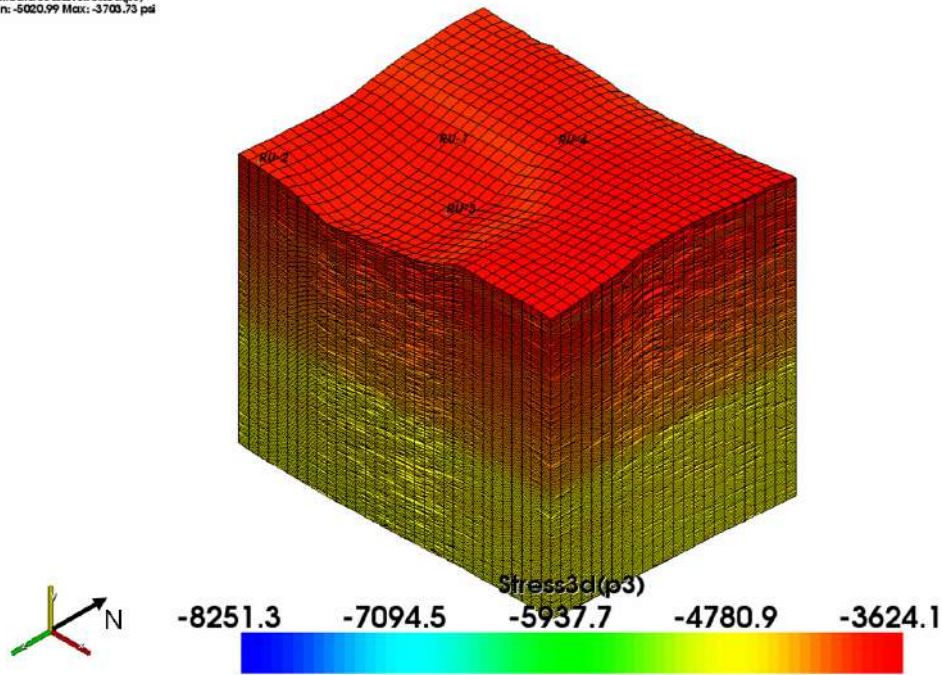


Figure 5.15: Absolute effective stress in 1981 for entire model. This is a product of boundary conditions as described in Ch.2.

Model: Pullson_3to1_TRUE_110507 : 1/10/2003
Timestep: 269 : 815.7 days
Cell Data Scalar: Stress3d(p3)
Min: -8111.07 Max: -3590.54 psi

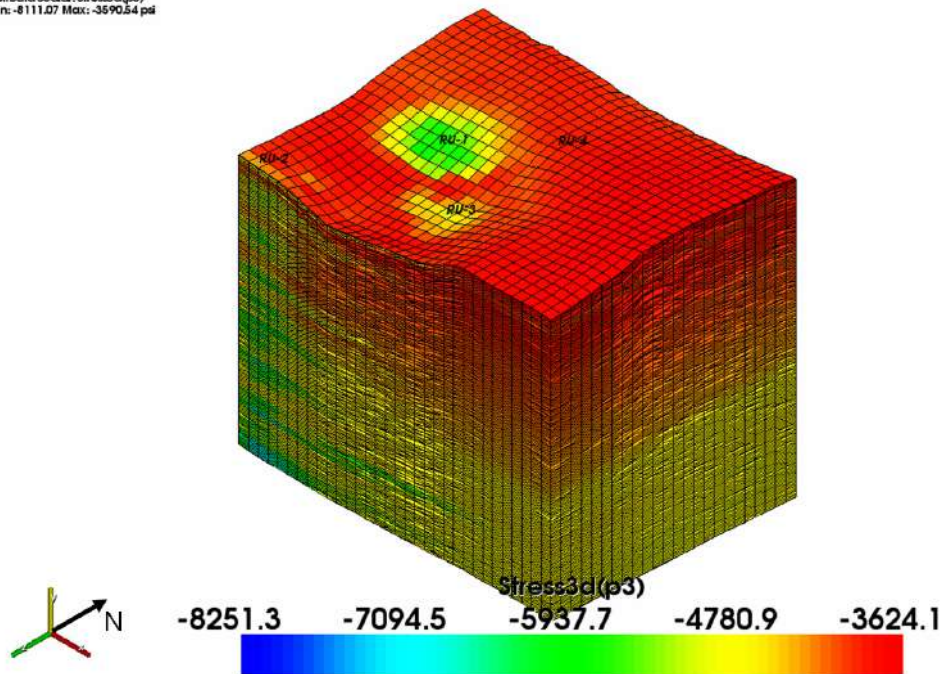


Figure 5.16: Absolute effective stress in 2003 for entire model.

Model: Rufison_3to1_TRUE_110607 : 1/9/2004
TimeStep: 280 : 8493 days
CellData Scalar: Stress3d(p3)
Min: -8016.06 Max: -3601.62 psi

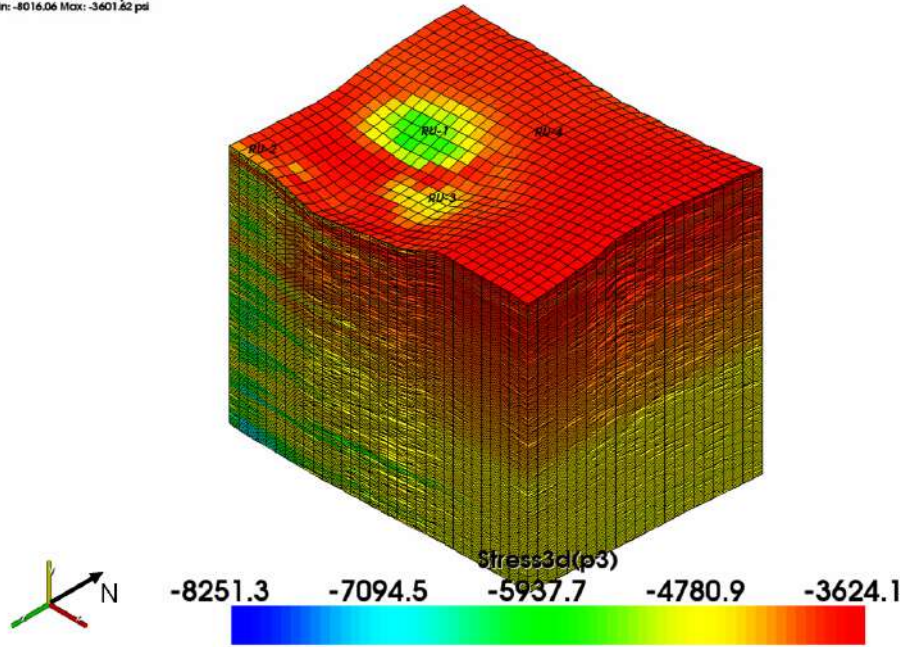


Figure 5.17: Absolute effective stress in 2004 for entire model.

Model: Rufison_3to1_TRUE_110607 : 1/8/2006
TimeStep: 504 : 9192 days
CellData Scalar: Stress3d(p3)
Min: -8251.27 Max: -3624.1 psi

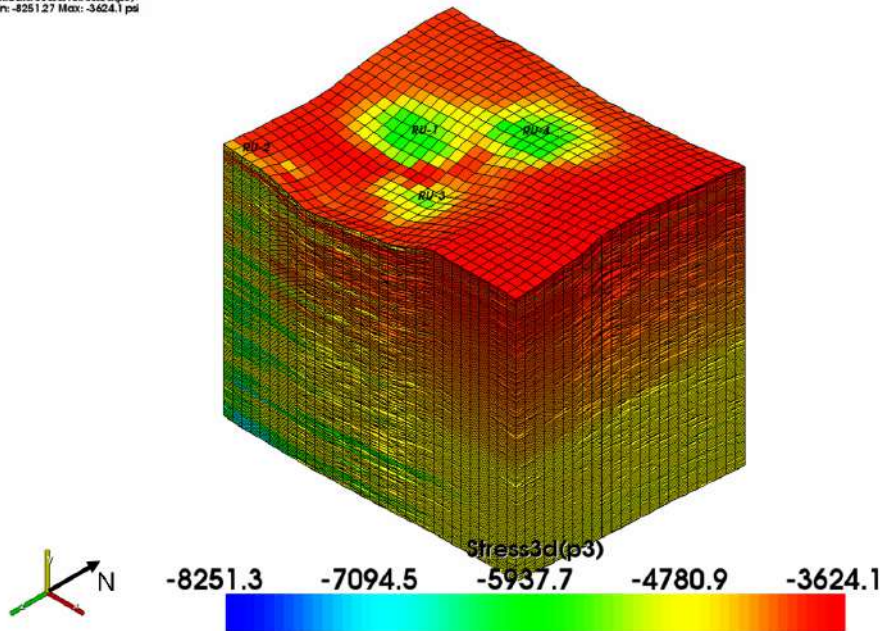


Figure 5.18: Absolute effective stress in 2006 for entire model. Note location of new wells and associated stress change.

5.3.3 2003-2004 Pressure and Effective Stress Change

As shown above (fig. 5.11), the pressure and effective stress change from 2003-2004 is smaller in magnitude from 2003-2006. This is apparent in the overburden change, which is shown in figures 5.15-5.18. Overburden effective stress change is directly coupled to pressure and is usually greater in magnitude in this model (see equation 4.8). Minimum and Maximum horizontal effective stress change within the model boundaries is almost non-existent for 03-04, therefore it will not be shown. Three depth levels have been chosen for simplifying the explanations of the results. These depths have been chosen as they correspond with the highest seismic (S22) anomalies. The same depth will be shown for all principle effective stresses, depths, and time periods.

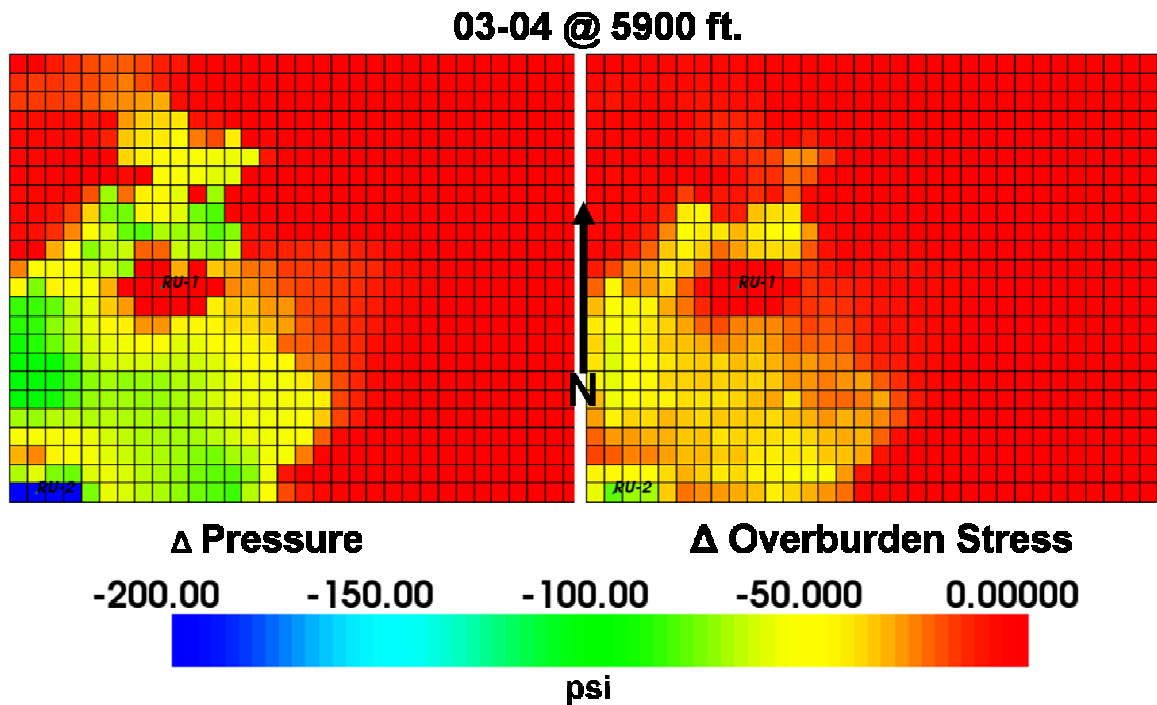


Figure 5.19: Pressure change from 03-04 compared to the effective overburden stress (σ_v) change at 5900ft. depth in the reservoir. Note the visual similarity and scale.

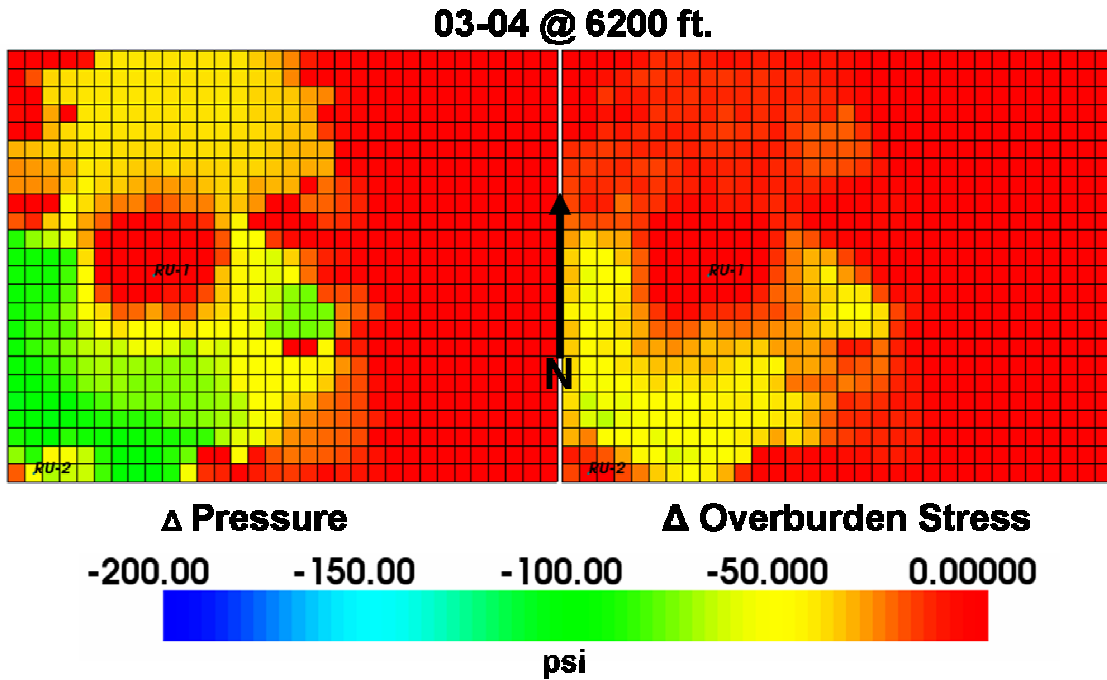


Figure 5.20: Pressure change from 03-04 compared to the effective overburden stress (σ_v) change at 6200ft. depth in the reservoir. Note the visual similarity and scale.

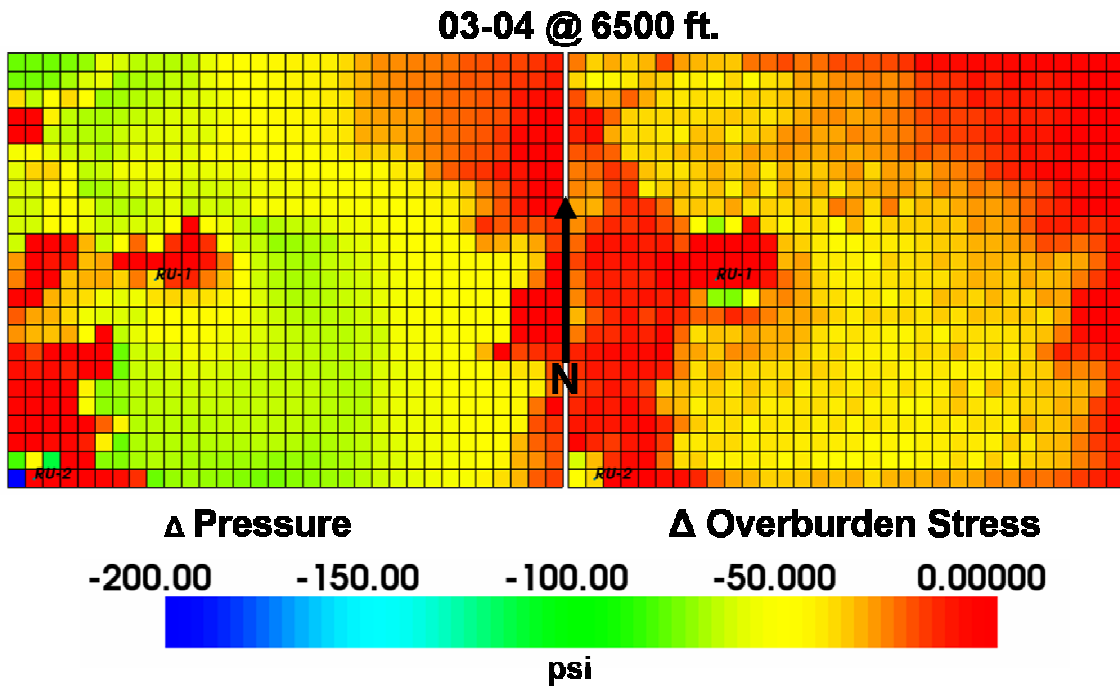


Figure 5.21: Pressure change from 03-04 compared to the effective overburden stress (σ_v) change at 6500ft. depth in the reservoir. Note the visual similarity and scale.

Several points become apparent from these results. First is the dependence of effective stress change on pressure change. Due to the equation:

$$\sigma'v = Sv - \alpha Pp \quad (4.8)$$

Where: $\sigma'v$ = Effective overburden stress
 Sv = Overburden stress
 α = Biot's constant
 Pp = Pore pressure

Remembering that these changes are relatively small from 03-04 (see fig. 5.2), the change depends on pore pressure change times Biot's constant which in this hard formation is modeled at 0.7 (see Ch. 4 for input description). The magnitudes of effective overburden stress are approximately 70% of pore pressure change. This pressure change also relates to horizontal effective stress changes, but due to the low pressure change (at a max ~200 psi) little to no horizontal effective stress change is seen. These changes will be highlighted by the much larger magnitudes from 2003-2006.

5.3.4 2003-2006 Pressure and Effective Stress Changes

As stated above, the drilling of RU-3 and RU-4 has caused a much larger pressure drop within the model. This has caused large effective stress changes in all three principle stresses as well. These changes, their causes, and the implications are discussed below.

The above relations to effective overburden are still the same for these figures. From 2003-2006 maximum pressure change occurred around RU-3 and RU-4 at a magnitude of ~2000 psi. The scales shown below are smaller, and are shown to highlight the shape and extent of smaller changes. For other depths please see Appendix A.

03-06 @ 5900 ft.

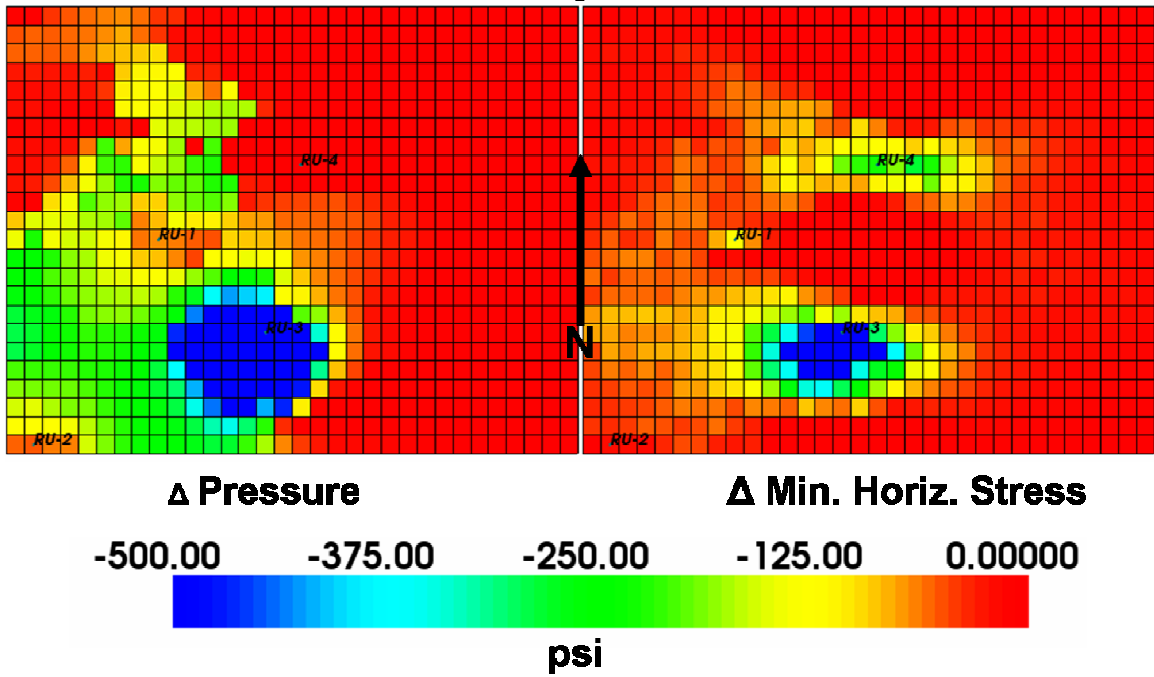


Figure 5.22: 2003-2006 minimum horizontal effective stress change compared to 03-06 pressure change. Note the direction of the stress anomaly and the direction of input horizontal stress (98 degrees east of north). This is also impacted by lithology and modified permeabilities from modeled hydraulic fractures. Also note stress change from coupling and not pressure change at RU-4

03-06 @ 5900 ft.

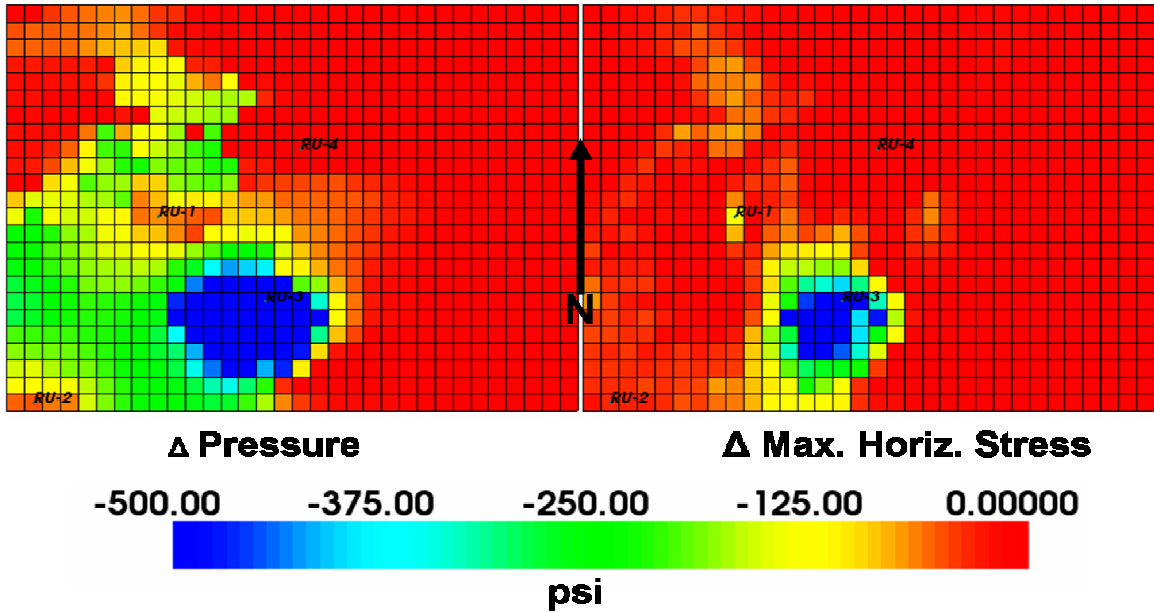


Figure 5.23: Maximum horizontal effective stress change from 2003-2006 compared to pressure change from 03-06. Note higher magnitude due to larger pressure changes and direction perpendicular to min.

03-06 @ 5900 ft.

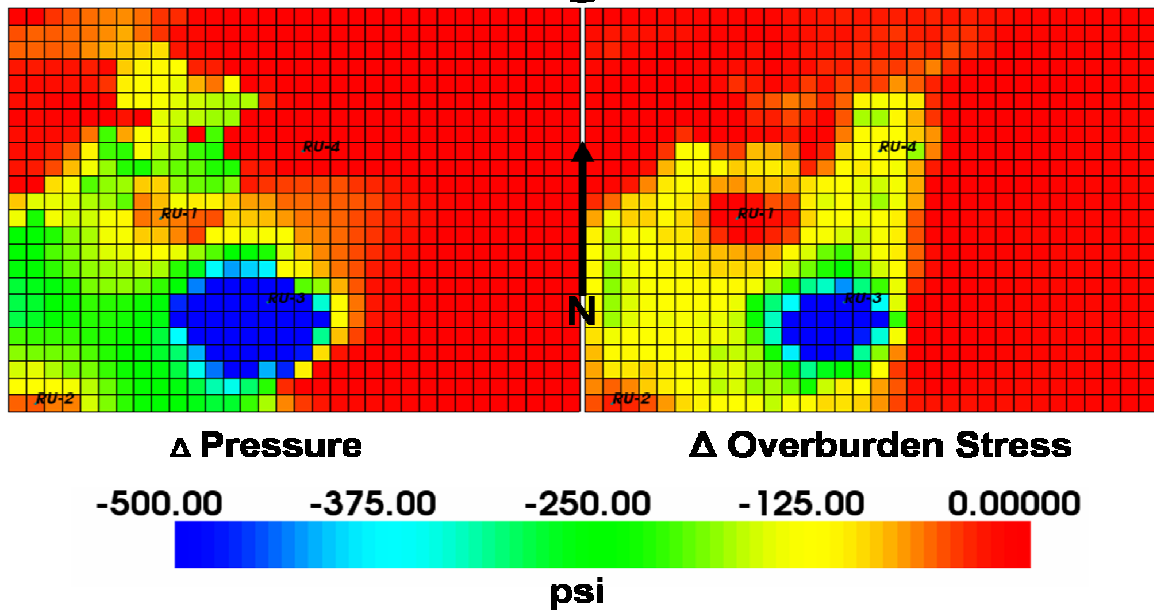


Figure 5.24: Overburden effective stress change from 2003-2006 compared to pressure change from 03-06. Note Pressure change is absent from RU-4 yet present in overburden change. This could be a product of coupling and depletion from above and below not explained by simplified equations shown here.

Above at 5900 ft. depth several conclusions can be made. The minimum horizontal effective stress change is linked to the direction input into the simulator (horizontal stress azimuth). This change is a visual example of a 'drainage ellipse' that has been discussed by previous authors on Rulison (Higgins, 2006) which is caused by hydraulic fracturing. In the far-field, multiple fracture directions also aid production and these multiple fracture directions can be seen in image logs (Matesic, 2006), although hydraulic fracturing dominates near wellbore production. This ellipse is essentially why Rulison field is being drilled on 10 acre spacing (fig. 5.25).

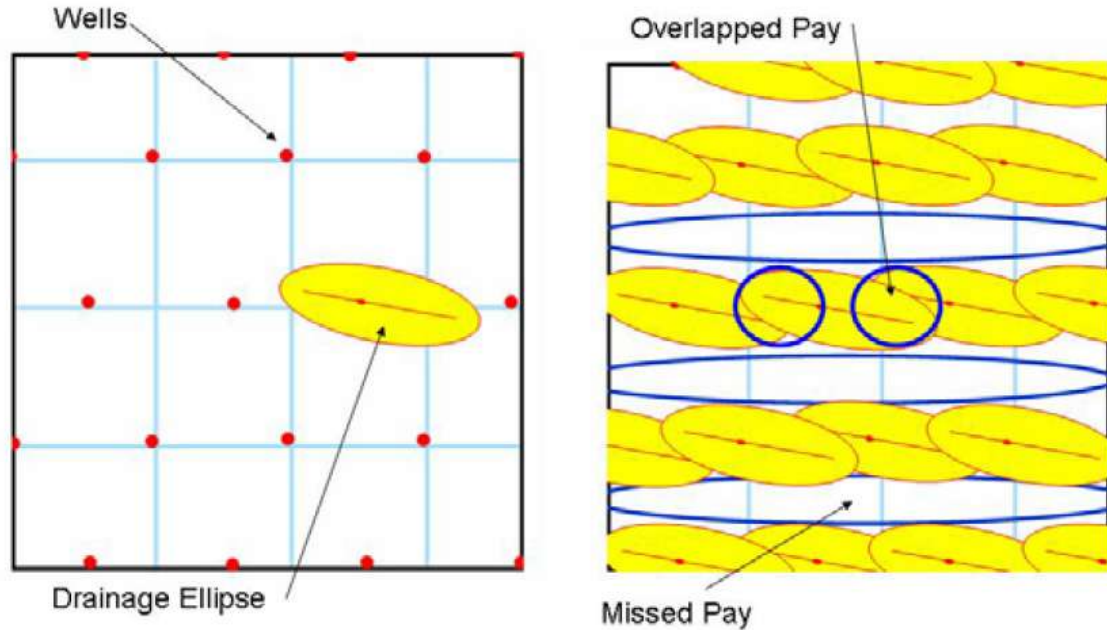


Figure 5.25: Figure showing drainage ellipse concept, this figure is specific to Rulison's minimum horizontal stress direction. This concept is highlighted by the minimum horizontal stress change in all three intervals from 2003-2006. From Higgins, 2006.

In addition to this, the scale is becoming more negative, this is due to the convention used in this thesis where compressive stresses are considered negative. Minimum and maximum horizontal effective stress changes are controlled by the equations shown below.

$$\sigma_{h \min} = \frac{\nu}{1-\nu}(\sigma_v - \alpha Pp) + \frac{E}{1-\nu^2} \epsilon_{H \min} + \frac{E\nu}{1-\nu^2} \epsilon_{H \max} + \alpha Pp \quad (4.9)$$

Where: σ_v = Effective overburden stress

$\sigma_{h \min}$ = Effective minimum horizontal stress

ν = Poisson's ratio

E = Young's modulus

Pp = Pore pressure

$\epsilon_{H \min}$ = Minimum horizontal strain

$\epsilon_{H \max}$ = Maximum horizontal strain

α = Biot's constant

Pp = Pore pressure

$$\sigma_{H \max} = \frac{\nu}{1-\nu}(\sigma_v - \alpha Pp) + \frac{E}{1-\nu^2} \epsilon_{H \max} + \frac{E\nu}{1-\nu^2} \epsilon_{H \min} + \alpha Pp \quad (4.10)$$

Where: σ_v = Effective overburden stress

$\sigma_{H \max}$ = Effective maximum horizontal stress

ν = Poisson's ratio

E = Young's modulus

Pp = Pore pressure

$\epsilon_{H \min}$ = Minimum horizontal strain

$\epsilon_{H \max}$ = Maximum horizontal strain

α = Biot's constant

Pp = Pore pressure

From the above equations it can be seen that there is a large dependence on Young's modulus, Poisson's ratio, and the effective overburden stress. Boundary conditions initialize the horizontal strains, and the change is dictated simply by pore pressure changes from cell to cell (or effective stress change). The direction is also important as the minimum horizontal effective stress direction is perpendicular to maximum horizontal effective stress. This direction controls the drainage ellipse. The pressure change at this interval not corresponding to effective stress change can be explained through coupling. Effective stress change is coupled in a 3-dimensional model to what happens above, below, and next to it (i.e. pressure and stress change). This can be seen from the other depth intervals as well (Appendix A).

From previous chapters it has been shown that there are natural fractures present in this reservoir (Ch. 2 G-function analysis). The production model is not capable of incorporating discrete hydraulic or natural fractures. Therefore, modified permeabilities have been used to match pressures for hydraulic fractures. It can be seen that there is much larger magnitude changes from 2003-2006 and these changes should result in a larger response of time-lapse shear waves. This is due to the hard rock environment;

since there is no collapse, porosity change, or subsidence. The only physical parameters changing with time are pressure, stress, natural fracture compliance, and hydraulic fracture compliance. Hydraulic fracture change could produce strain changes; however, the model is incapable of simulating this. These physical changes will be the topic of the next section which deals with the comparison of the model to seismic.

5.4 Geomechanical Modeling Compared to Shear Seismic

As stated in chapter two, shear waves are much more suited to our needs in this naturally fractured reservoir (Ch. 2.5), specifically slow shear (S22) impedance changes. The emphasis of this section will be on 2003-2006 shear data as the magnitude change within the mechanical boundaries are much larger, resulting in much higher percentage seismic anomalies. For complete 2003-2004 please see Appendix C. The changes in the seismic are compared to model pressure and effective stress changes below (fig. 5.27-5.34). The effective stress changes in this instance are set with a maximum horizontal stress direction of 135 degrees to match shear seismic rotation. This is in contrast to the effective stresses shown above which have the maximum stress direction of 98 degrees (fig. 5.26). 135 degrees (or N45W) is the direction in which the shear data has been rotated to align with the average reservoir fracture direction and minimize off diagonal energy (Rumon, 2006). 98 degrees is the direction of present day maximum horizontal stress (Higgins, 2006). I have shown a comparison of seismic with the models horizontal stress azimuth set to 135 degrees as this allows a more accurate comparison due to similar geometric rotations.

Effective min. horiz. stress comparison @ 5900 ft.

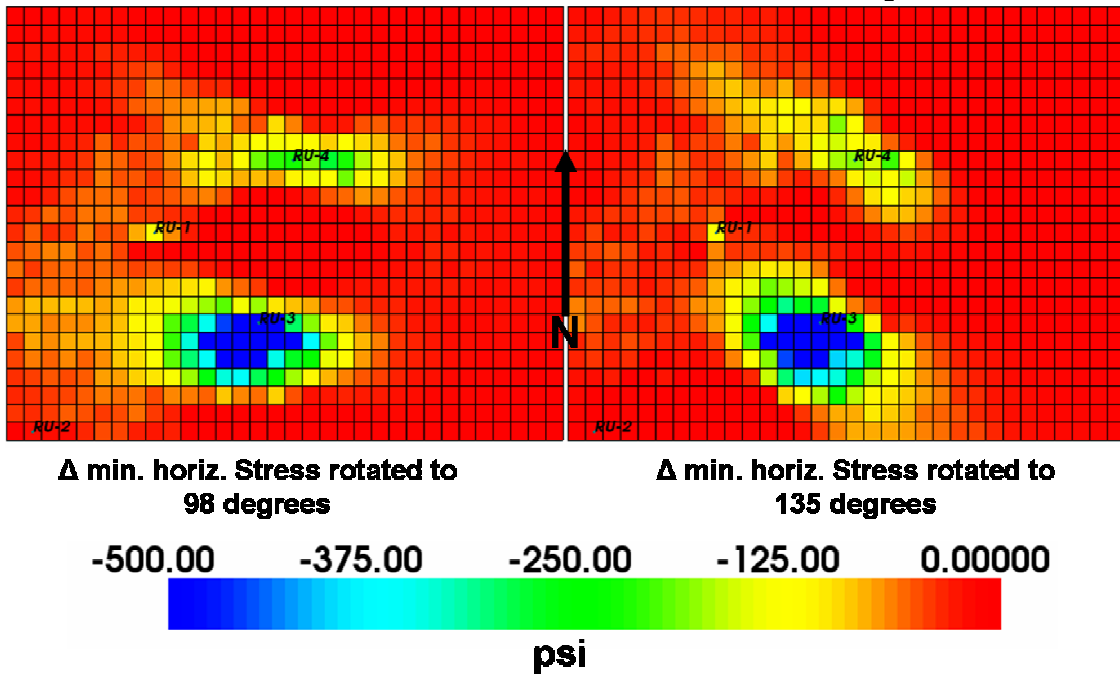


Figure 5.26: Figure showing the modeled difference in maximum horizontal stress direction change. On the left is the modeled present day maximum horizontal stress direction (98 degrees) while on the right is the model using the direction of rotated shear seismic, which is 135 east of north or N45W.

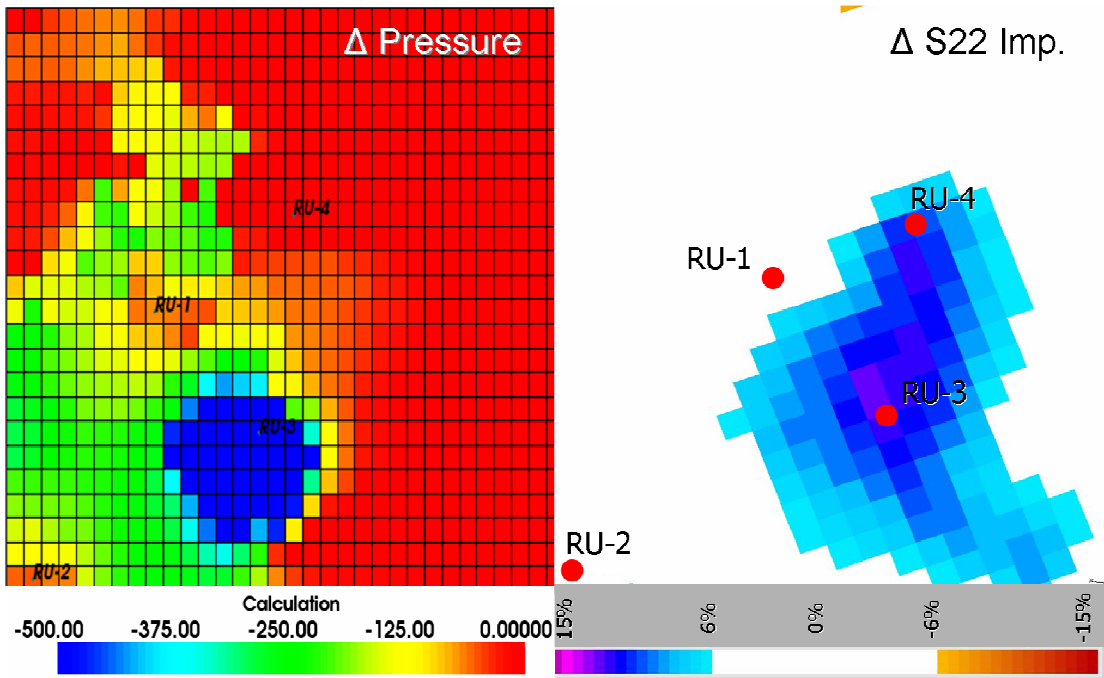


Figure 5.27: Pressure compared to slow shear (S22) impedance change from 2003-2006 at 5900 ft. depth. Note no pressure change around well RU-4. This problem could be from scale issues between seismic and the model.

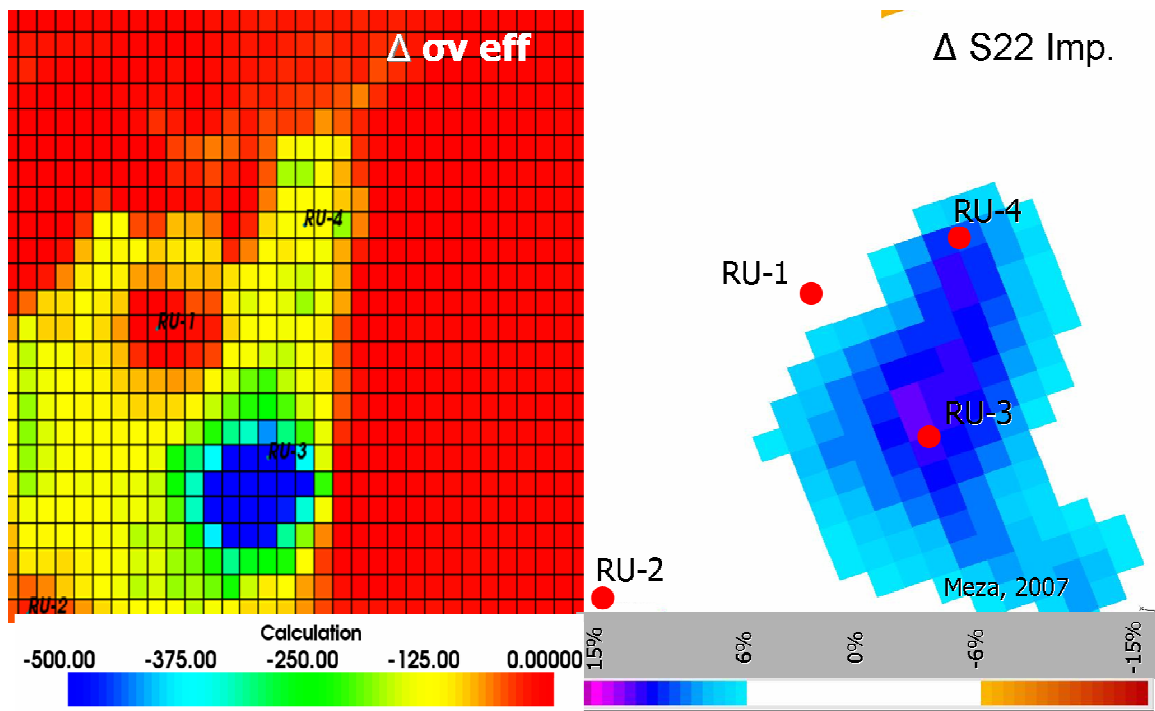


Figure 5.28: Effective overburden stress change from 2003-2006 compared to slow shear (S22) impedance change at 5900 ft. depth. Note overburden change with no pressure change at RU-4.

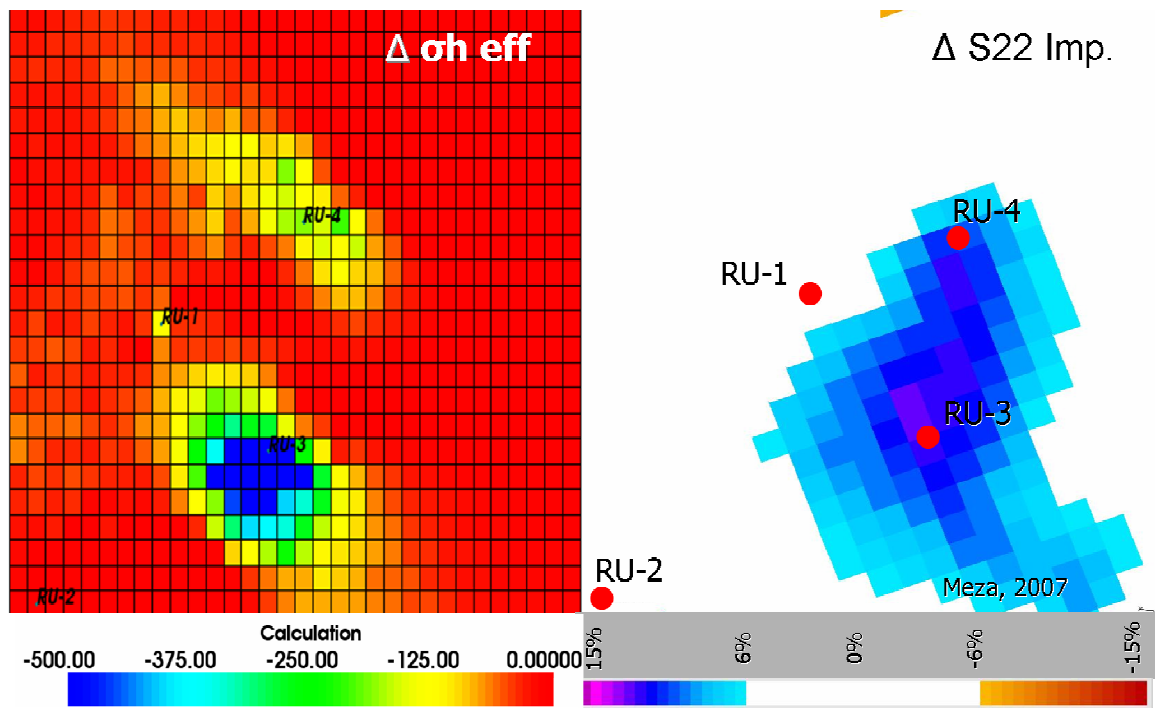


Figure 5.29: Effective minimum horizontal stress change from 2003-2006 compared to slow shear (S22) impedance change at 5900 ft. depth. Note effective stress change with no pressure change at RU-4. This is probably due to coupling from above and below.

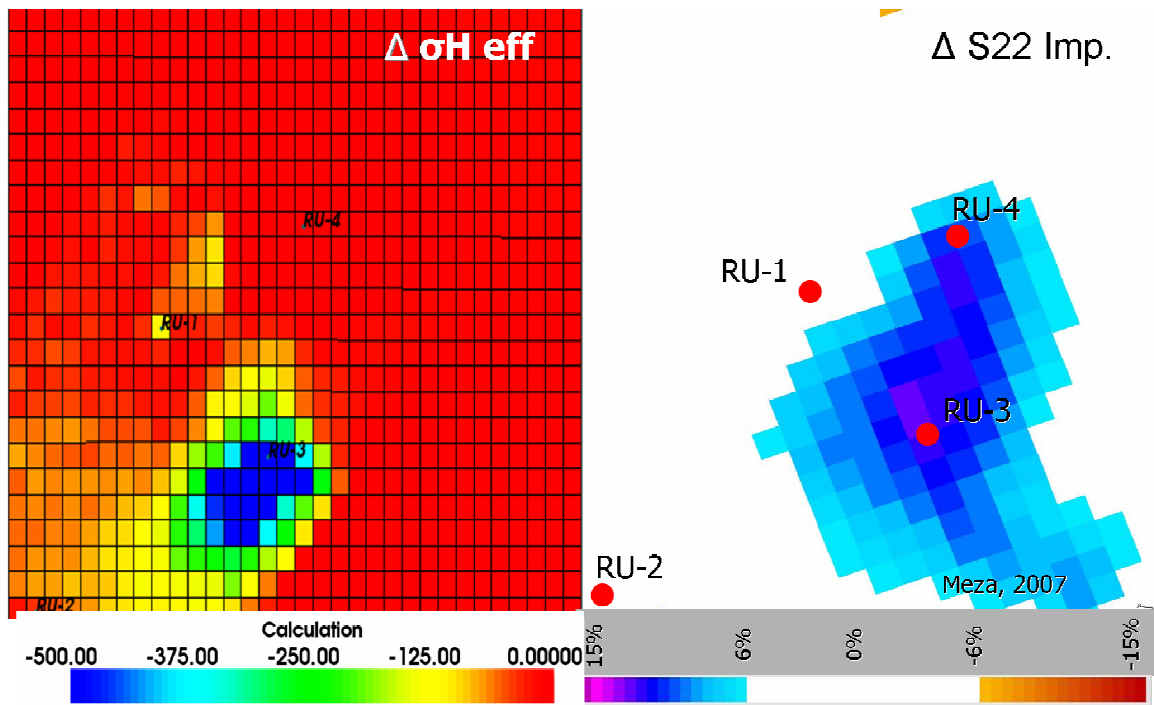


Figure 5.30: Effective maximum horizontal stress change from 2003-2006 compared to slow shear (S22) impedance change at 5900 ft. depth. Note no effective stress change at well RU-4.

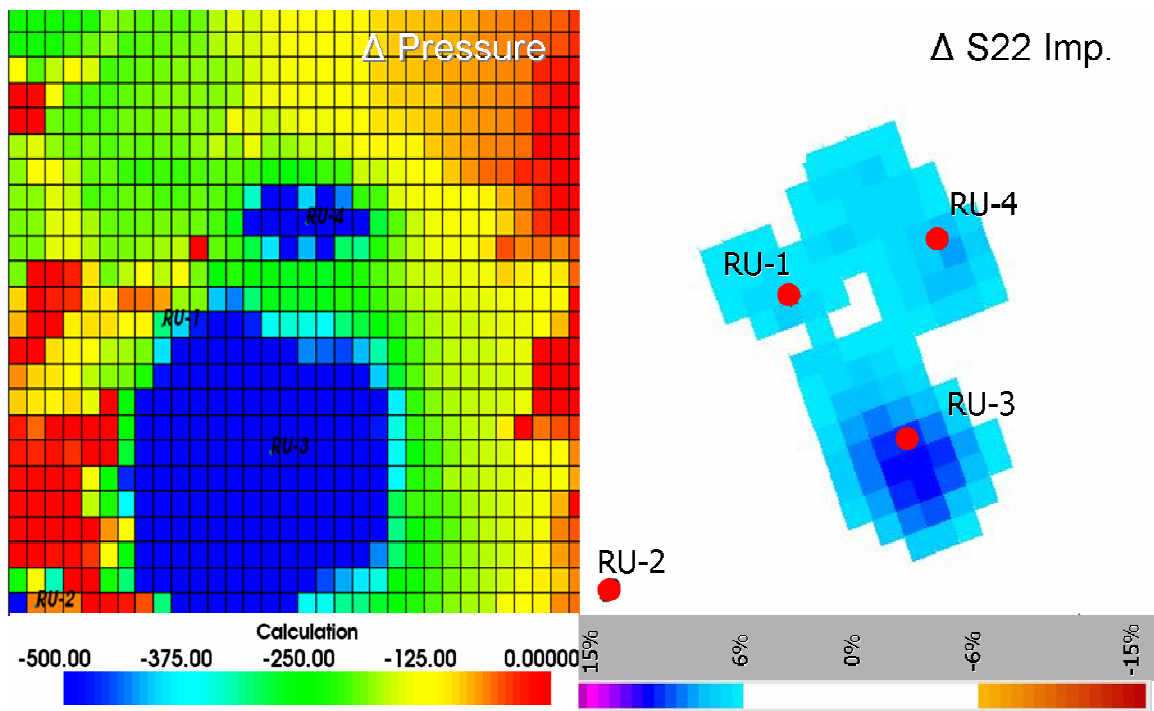


Figure 5.31: Pressure compared to slow shear (S22) impedance change from 2003-2006 at 6500 ft. depth.

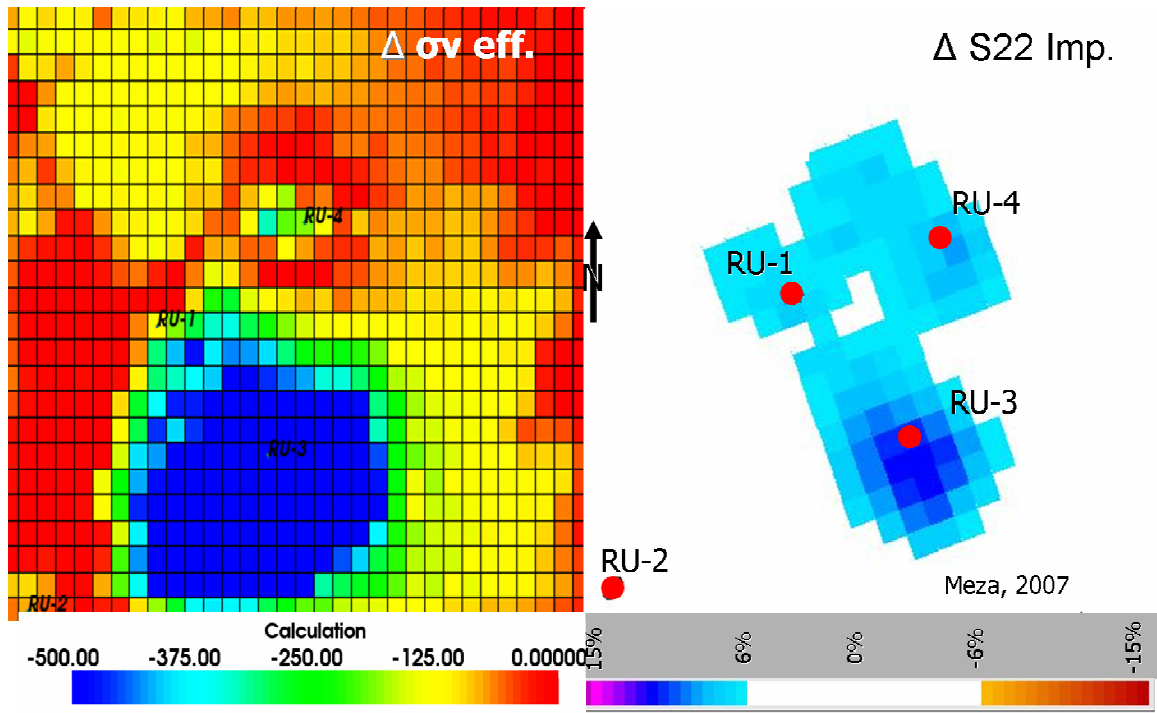


Figure 5.32: Effective overburden stress change from 2003-2006 compared to slow shear (S22) impedance change at 6500 ft. depth.

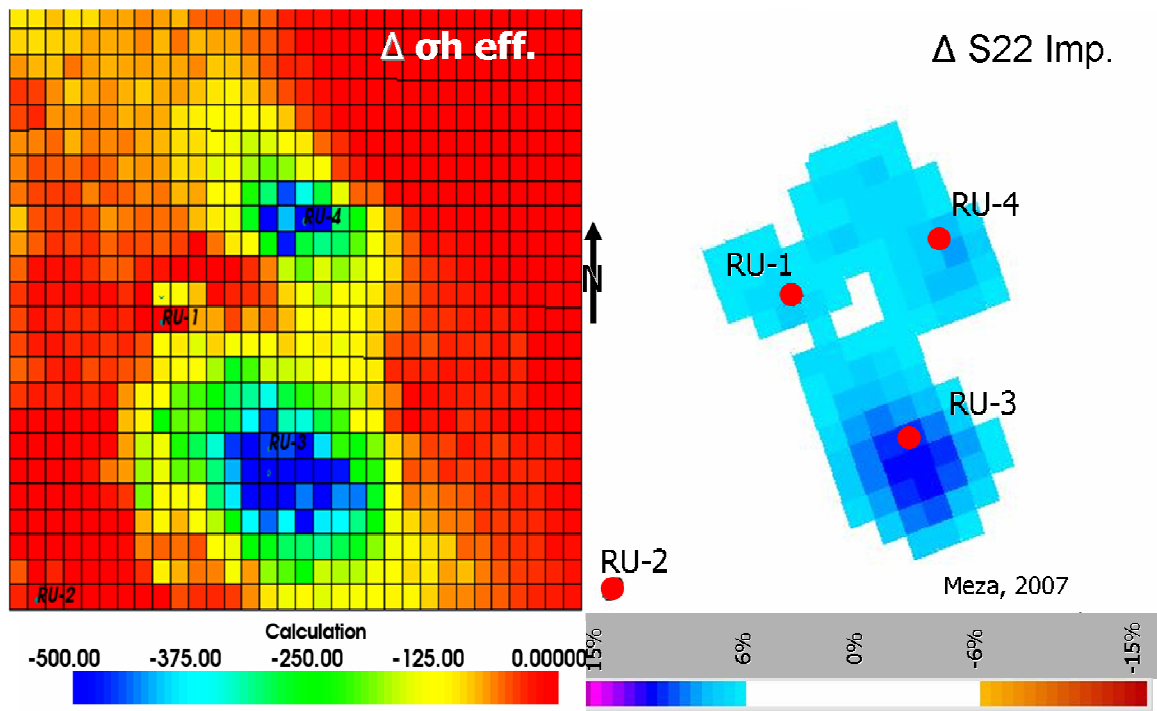


Figure 5.33: Effective minimum horizontal stress change from 2003-2006 compared to slow shear (S22) impedance change at 6500 ft. depth.

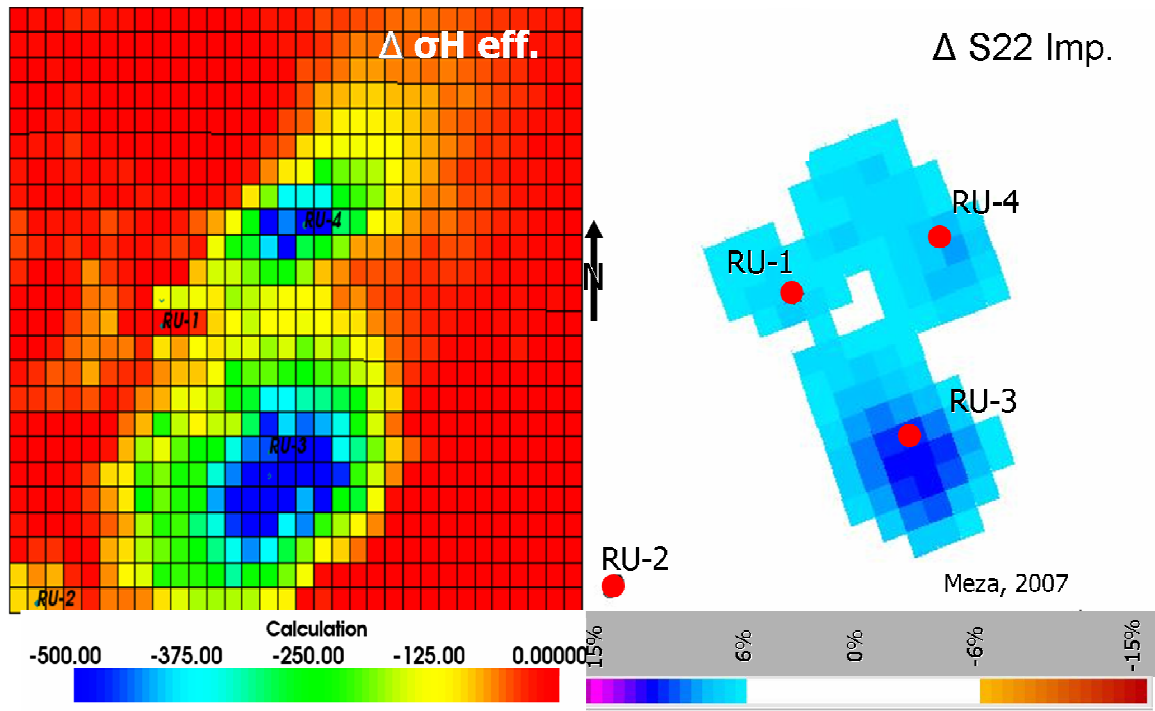


Figure 5.34: Effective maximum horizontal stress change from 2003-2006 compared to slow shear (S22) impedance change at 6500 ft. depth.

The magnitudes from 2003-2006 in the shear seismic are much higher in the 2003-2006 seismic 6-15% impedance change as opposed to 2-6% impedance change in 2003-2004 (Rumon, 2006 and Meza, In Progress). This is a result of the two new wells being drilled in 2005. The pressure drops are much larger due to the production and hydraulic fracturing in the two wells.

Visually, the pressure and stress change correlate well to the seismic. However, the correlation is not perfect. There are several reasons for this. First, is the absence of natural fractures in the model which are present in the reservoir as seen in FMI and other studies completed on Rulison (Matesic, 2006 and Higgins, 2006). Second, the seismic is also rotated to N45W (or 135 degrees), which minimizes off diagonal energy in the shear seismic but is an amalgamation of regional faulting, fracturing, and stresses. This seismic direction is average for the reservoir, and does not take into account local variations that

were observed at MWX and at Rulison field (Higgins, 2006 and Vasconcelos and Grechka, 2007). Third, the model shows stresses broken down in to three principle stresses with pressure change. The seismic is the combination change of all of these components including natural fracture closure. Fourth, the statistical nature of the model also affects the correlation. All properties away from the well bore are statistically simulated, although constrained by the seismic V_p/V_s11 , it is still a two-point statistical guess. This highlights the need to build more realistic connective models, which is research that is ongoing in the RCP (Casey, In Progress). The final problem is the problem of scale; each cell is 50 ft. x 50ft. wide and 9 ft. thick. Shear wave resolution at this depth is approximately 70 ft. Therefore, we have taken the depth from seismic in the middle of the anomaly and taken the according depth from the geomechanical model. The problem of scale needs to be considered when analyzing the above image. This problem is not insurmountable, and different scales of the model can be considered and built in the future when analyzing the model against seismic (using proper upscaling methods for rock moduli).

Several conclusions can now be made from the above interpretation. The most apparent is that slow shear seismic (S22) is imaging areas of pressure and effective stress change. Although not perfect, the correlation to new wells is difficult to discredit. From this, well placement and completions can be optimized. In addition, this highlights the need for more realistic connective models to be built using time-lapse seismic as a soft constraint. This is part of future work ongoing by Matthew Casey at the RCP.

5.5 Well Placement

The above comparisons to seismic have shown that slow shear (S22) impedance is more than likely reacting to pressure and effective stress changes as indicated by the geomechanical model. Although the model is incapable of incorporating natural fractures, an important feature and permeability enhancer at Rulison, the model still highlights the magnitude of far-field depletion at Rulison. Since these wells are being drilled on ten acre spacing, incorporating time-lapse seismic to avoid already producing and depleted zones is critical. An example of this far field depletion is shown in figure 5.35.

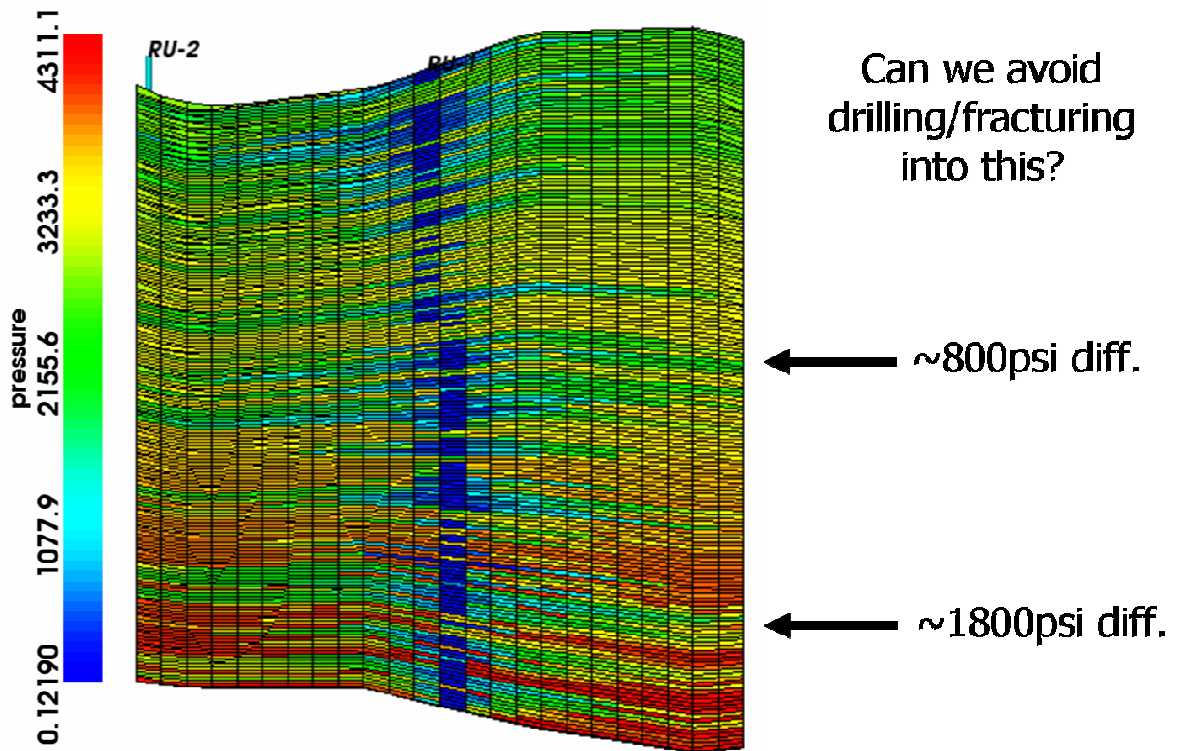


Figure 5.35: Cross-section view showing extent of far-field depletion from RU-1. At this point in time RU-1 had been producing for almost 25 years, this was the month before two new wells were drilled only 1000 ft. away at depth.

In the plane coming out of the page, RU-3 and RU-4 had been drilled and completed into several of these partially depleted zones. As shown in the figure, far-field depletion has progressed to over 600 ft. away from the wellbore (each cell is 50 x 50 x 9

xyz). In some areas the depletion is in excess of 1800 psi. With multiple layers of dramatically differently pore pressure these data will allow us to optimize completions such as placement of perforations, completion staging, and zone selection. For example, time-lapse seismic can show areas of depletion surrounding a new well at different depths, this can in turn be used to avoid fracturing this zone, and placing more perforations in untapped sands elsewhere in the formation in new wells. This concept is highlighted below.

5.6 Gamma Comparison

Another method to analyze the model is to use the gamma operator as defined by Hettema, et. al., 1998. The mathematics and comparison to data is outlined below.

$$\gamma_v = \Delta\sigma_v / \Delta P_p \quad (5.1)$$

Where: γ_v = Depletion Coefficient
 $\Delta\sigma_v$ = Change of total vertical stress
 ΔP_p = Change in pore pressure

Similarly, this method can be applied to both minimum and maximum horizontal stresses as shown below:

$$\gamma_H = \Delta\sigma_H / \Delta P_p \quad (5.2)$$

Where: γ_H = Depletion Coefficient
 $\Delta\sigma_H$ = Change of total max. horiz. stress
 ΔP_p = Change in pore pressure

$$\gamma_h = \Delta\sigma_h / \Delta P_p \quad (5.3)$$

Where: γ_h = Depletion Coefficient
 $\Delta\sigma_h$ = Change of total min. horiz. stress
 ΔP_p = Change in pore pressure

From these equations we can make a comparison between the initial data in the model in 1981 and the depleted data in 2006 (1981 shown below as $\sigma_{h \text{ init}}$ and $P_{p \text{ init}}$ respectively). This will give us insight into how the total stresses are changing relative to the pressure depletion within the model.

Model Gamma Calculation:

$$\gamma_h = \frac{\Delta\sigma_h}{\Delta P_p} = \frac{\sigma_{h \text{ init}} - \sigma_{h \text{ 2006}}}{P_{p \text{ init}} - P_{p \text{ 2006}}} \quad \text{or} \quad \Delta\sigma_h = \gamma_h \Delta P_p \quad (5.4)$$

Where: $\sigma_{h \text{ init}}$ = Initial minimum horizontal stress
 $P_{p \text{ init}}$ = Initial pore pressure
 $\sigma_{h \text{ frac}}$ = 2006 min. horiz. stress
 $P_{p \text{ frac}}$ = 2006 pore pressure

This equation can be applied with the change of maximum horizontal stress and overburden in the numerator as well. This is what has been carried out below, which results in the following table.

**MODEL
GAMMA
1981-
2006**

Depth ft.	Pp diff psi	h diff. psi	GAMMA Min.
5900	2308	472	0.20
6200	1473	310	0.21
6500	3399	1017	0.30

Hdiff psi	GAMMA Max.
628	0.27
666	0.45
1116	0.33

Over diff. psi	GAMMA Over.
254	0.11
579	0.39
427	0.13

Table 5.1: Table showing Gamma calculations from geomechanical modeling.

The table above highlights several things. The first is that gamma varies with depth. This is a product of the heterogeneous lithology present at Rulison field. Another is that γ_h for most environments, such as the North Sea and the Gulf of Mexico, has been calculated as $\sim .5$ (Hettema, et. al., 1998). This hard rock environment at Rulison causes γ_h to be reduced to around 0.2-0.3. This can be visualized with the conceptual model shown in figures 5.36-5.38 below. Zonal fracturing implies that several zones are being fractured at the same time; they are perforated, the zone is isolated from the rest of the wellbore, and hydraulically fractured in one stimulation. This procedure is what is currently being implemented at Rulison field.

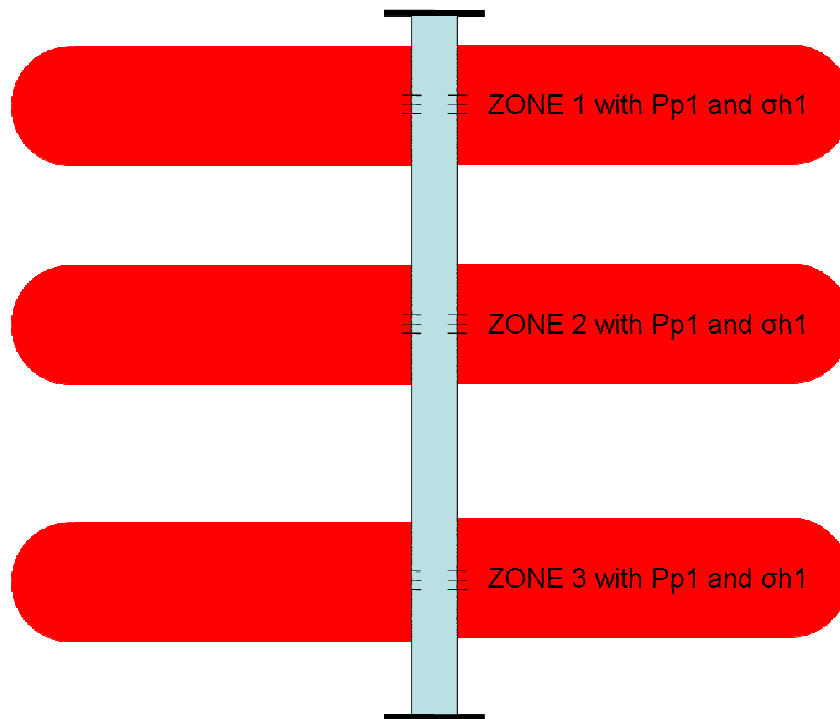


Figure 5.36: Conceptual model of zonal fracturing where all zones have same pore pressure and minimum horizontal stress and are being fractured simultaneously.

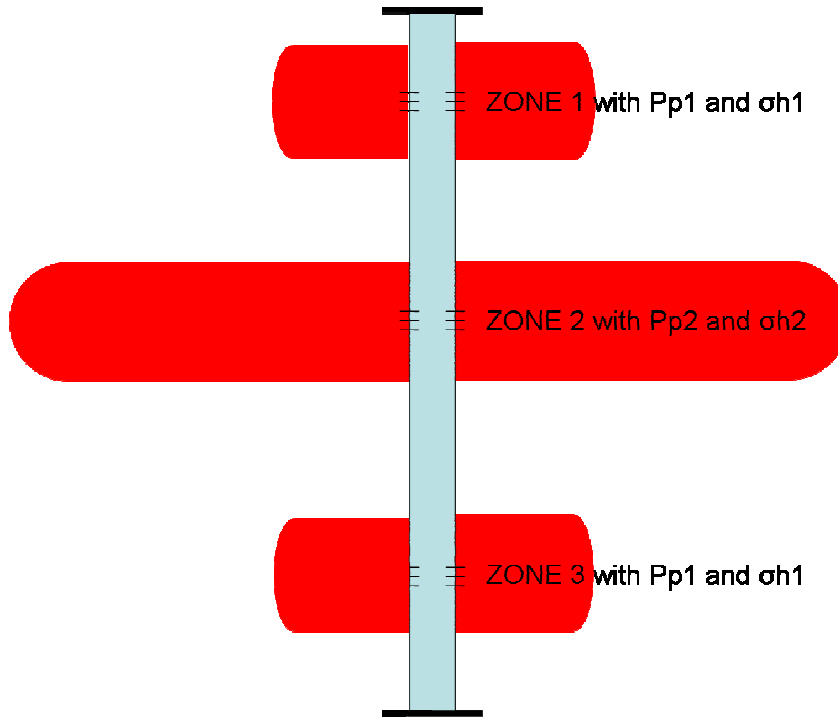


Figure 5.37: Conceptual model where zone 2 is partially depleted and is causing a larger fracture in the depleted zone. P_{p2} and $\sigma_{h2} < P_{p1}$ and σ_{h1} .

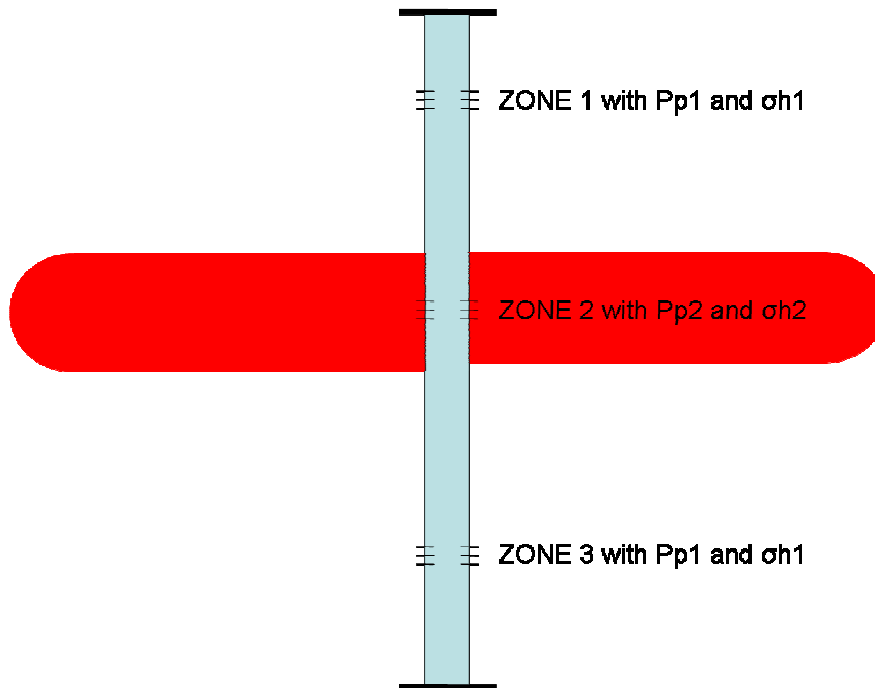


Figure 5.38: Conceptual model where a greatly depleted zone is diverting zonal hydraulic fracture and leaving virgin zones un-stimulated. P_{p2} and $\sigma_{h2} \ll P_{p1}$ and σ_{h1}

Figure 5.36 shows what fracturing would look like if γ_h were 0. If it were 0, no horizontal stress change would occur for any magnitude of pressure depletion. At Rulison, modeling has shown that it is between .2-.3, which has a smaller impact than say in other more conventional areas with a γ_h of .5. This still means, however, that depletion has an affect on minimum horizontal stresses. I have shown that effective stress increases with time (fig. 5.4-5.6); in addition, total stress is decreasing over time. When hydraulically fracturing it is the total stress that must be overcome (Bratton, Personal Communication), and this decreases with time and production as shown below.

$$S_{h \min} = \sigma'_{h \min} + \alpha P_p \quad (5.5)$$

Where: $\sigma'_{h \min}$ = Effective maximum horizontal stress

α = Biot's constant

P_p = Pore pressure

$S_{h \min}$ = Total minimum horizontal stress

In 1981 at 5900 ft. (fig. 5.4)

$$S_{h \min} = (1937) + (.7)(2758) = 3868 \text{ psi}$$

In 2006 at 5900 ft. (fig. 5.4)

$$S_{h \min} = (3080) + (.7)(451) = 3396 \text{ psi}$$

$$S_{h \min} (1981) - S_{h \min} (2006) = \mathbf{472 \text{ psi decrease}}$$

Imagine if the above zones were all open for fracturing. The depleted zone would 'capture' or be the path of least resistance for a hydraulic fracture to propagate. This would cause minimal fracturing, if any, into virgin zones and larger fractures created in already depleted/depleting zones. At Rulison it is possible that scenarios in figure 5.37 and 5.38 are taking place, especially with 10 acre spacing. This is a scenario we can avoid by integrating time-lapse seismic.

5.7 Sensitivity Analysis

From the modeling results a sensitivity analysis was carried out on inputs into the geomechanical model. This allows us to study the importance and impact of one parameter against another. What follows is the table shown in section 4.4.4 and then an in depth analysis of each parameter and their impact on the modeling.

Parameter	Input	Unit	Source
Young's modulus	ECLIPSE	psi	Geo-statistical model
Poisson's ratio	ECLIPSE	dimensionless	Geo-statistical model
Biot's coefficient	0.7	dimensionless	Rock physics
Thermal Expansion coefficient	9.0 e -06	1/F	default
Pressure	ECLIPSE	psi/ ft	Higgins, 2006 and Williams
Max horizontal stress coefficient	see above	dimensionless	
Min horizontal stress coefficient	see above	dimensionless	
Soil effective weight	see above	psi/ ft	
Horizontal Stress azimuth	08	degrees	see below
Vertical Stress Inclination	90	degrees	see below
Failure Criterion	Mohr-Coulomb		see below
Cohesion	1.45 e 21	psi	default
Friction angle	30	degrees	default
Dilatation angle	5	degrees	default
Tensile stress cut-off	1.45 e 21	psi	default
Material fluidity	1	dimensionless	default
Hardening/Softening coefficient	0	dimensionless	default
Permeability	ECLIPSE	mD	Geo-statistical model
Porosity	ECLIPSE	%	Geo-statistical model
Water Saturation	ECLIPSE	%	Geo-statistical model

Table 5.2: Inputs into geomechanical software.

- **Young’s modulus:** Probably the most important parameter in the whole workflow, Young’s modulus is attached to lithology in the geo-statistical modeling at the very beginning of the project. Although it is a rock property within the geo-statistical model, it is attached to lithologies with distinct ranges between sandstone and shale that are statistically significant (Casey, Personal Communication). This means that in production and mechanical modeling it is associated with porosity, permeabilities, and water saturations.
 - To reiterate, in the model, shales are zero porosity and 100% water saturation. Therefore, no flow in the production although stress change may occur due to changes in the model from above, below, or on the sides
 - In addition to this, Young’s modulus is also a parameter in horizontal effective stress changes.
 - The geo-statistical model has produced a statistical “guess” at what lies between well bores. The result is that we have produced our best guess, but Young’s modulus could vary between sand and shale at any one cell away from the wellbore, which as stated above has a large impact.
 - Numerically, Young’s modulus could vary as much as 50% between sand and shale at Rulison field (Sattler, 1991).
 - At Rulison, Young’s modulus as modeled for sandstones range from $4.04 * 10^6$ psi to $6.72 * 10^6$ psi (27.9 – 46.2 GPa). Shales range from $1.37 * 10^6$ psi to $2.70 * 10^6$ psi (9.44 GPa – 18.6 GPa). A transition facies has been modeled in between these values (Casey, Personal Communication and Casey, 2006). From MWX via Higgins, 2006.

- **Poisson's Ratio:** At Rulison field, analogues from the MWX and individual statistical studies (Casey, Personal Communication) have shown that Poisson's ratio falls in the same ranges (between .2 and .3) for sandstones and shales and does not vary with confining pressure (Sattler, 1991). Therefore, it has been populated randomly throughout the geo-statistical model, as there is not proper constraint on its value for sandstone and shale.
- This parameter has a large impact in modeling due to its presence in horizontal effective stress calculations; however, in this case it is of less importance due to its similarity between sandstone and shale and small variation.
- **Biot's Constant:** As stated in previous chapters, this parameter has a large impact on effective stress change (Hofmann et. al., 2005). It can best be illustrated by the equation below

$$\sigma'v = Sv - \alpha Pp \tag{4.8}$$

Where: $\sigma'v$ = Effective overburden stress
 Sv = Overburden stress = 2000 psi
 α = Biot's constant = 1
 Pp = Pore pressure = 1000 psi

Then:

$$\sigma'v = Sv - \alpha Pp = (2000) - (1)(1000) = 1000 \text{ psi.}$$

if we change Biot's to .7, like we have done for this study then:

$$\sigma'v = Sv - \alpha Pp = (2000) - (.7)(1000) = 1300 \text{ psi}$$

- It is now apparent that this causes a 30% increase in effective stress change. It should also be noted that this applies only to the mechanical modeling portion of the workflow

- **Thermal Expansion Coefficient:** This parameter is of importance if there are anomalously high temperatures present in the reservoir. This is not the case at Rulison field and has been left at the default level.
- **Pressure:** As discussed in this chapter, the model is extremely sensitive to pressure changes and where this pressure change occurs. Without pressure change there can be no effective stress change. This is illustrated by the equations below which are the same shown for Biot's. However, in this instance, we will choose one depth and two different gradients for pressure values (.433 which is hydrostatic and 1.0 which is used beneath the UMV in the overpressured Williams Fork).

$$\sigma'v = Sv - \alpha Pp \quad (4.8)$$

Where: $\sigma'v$ = Effective overburden stress

Sv = Overburden stress = 5000 psi

α = Biot's constant = .7

Pp = Pore pressure @ 6000 ft. (below 5000 ft. .433 psi/ft.) = 2598 psi.

Pp = Pore pressure @ 6000 ft. (below 5000 ft. 1.00 psi/ft.) = 3200 psi.

Then:

Hydrostatic: $\sigma'v = Sv - \alpha Pp = (5000) - (.7)(2598) = 3181$ psi.

Overpressure: $\sigma'v = Sv - \alpha Pp = (5000) - (.7)(3200) = 2760$ psi

- This produces a 15% change in effective stress. However, we have chosen the pressure values using constrained pressures from virgin formations in pilot wells provided by Williams Production Company and our own analysis of mini-fracture tests.
- **Maximum, Minimum, Soil Effective Weight:** Varying the boundary conditions will have a large effect on the initialization of initial conditions and initialization of horizontal strains. This was done with the best data available to us, and

varying these parameters has a large impact on the relative effective stress changes that occur within the model with production and time.

- **Horizontal Stress Azimuth and Vertical Inclination:** The horizontal stress azimuth dictates the direction of maximum horizontal stresses from North within the modeling program (VisGen manual). The vertical inclination is the angle the maximum principle stress is inclined to the vertical (VisGen manual), which in this case is the overburden and is 90 degrees.
 - Varying these parameters causes a change in the direction of maximum principle stresses and the inclination of horizontal stresses. It changes how Visage handles principle stresses. We are assuming the vertical stress is really vertical, which is valid as it can be seen from FMI analysis (Higgins, 2006).
- **Mohr-Coulomb Failure Criterion:** As discussed in section 4.4.4, the failure criterion is never reached due to the exceptionally hard nature of these rocks. Since these are hydraulically fractured, we are manipulating effective stresses. Since we use permeability modifiers to model hydraulic fractures, this is not simulated in the mechanical model. This concept is most easily shown with a simple Mohr circle diagram.

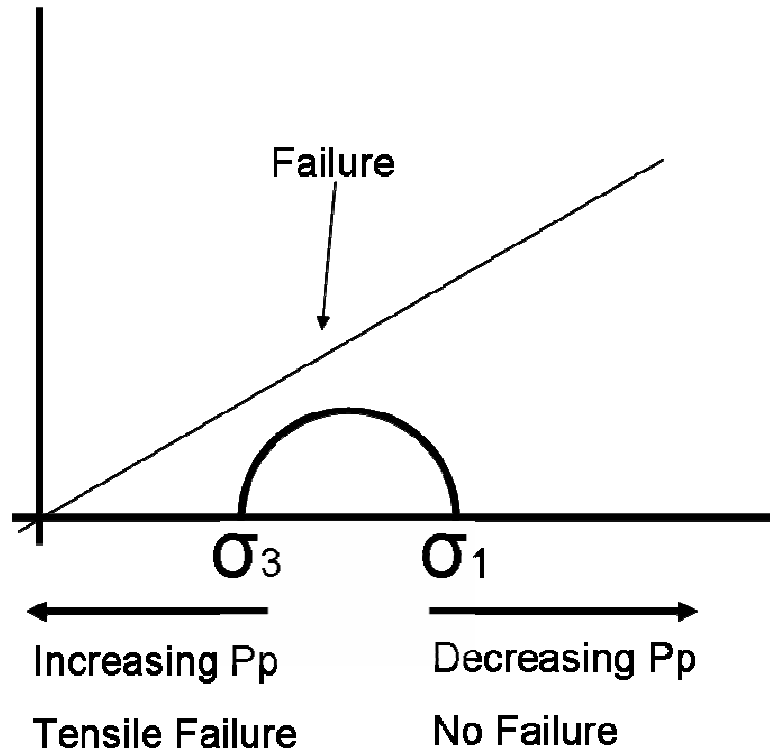


Figure 5.39: It can be seen that only when P_p is increased does the circle move toward failure (σ_1 and σ_3 maintain relative distance on x axis as total stress is not changing and are effective stresses). Then, after hydraulic fracturing, effective stress is increasing due to lower P_p from production.

- **Permeability, Porosity, and Water Saturation:** These parameters are all input within the Geo-statistical modeling step. These parameters have a large impact on where pressure change occurs and how much of it occurs. This is mostly manipulated in history matching to properly match pressures at the wellbore. In this way it affects the mechanical model, as the magnitude and amount of pressure change is controlled by permeabilities, porosities, and water saturations.
 - **Porosity-** Porosity values range from 1-25% for sandstones and transition zones and are modeled as zero for shales. These values were taken from well logs in Rulison field.

- **Permeability-** Permeabilities for the model range from .005 - .9 mD for sandstones and transition zones. Shales are modeled as effectively zero permeability. These values are taken from past MWX work and well logs.

5.8 Conclusions

This chapter has been an in depth overview of the modeling results, these results compared to seismic, and also a summary of the sensitivity of inputs into the model. I have contributed several conclusions to the ongoing work at Rulison field, and these conclusions are summarized below.

- Geomechanical modeling has shown that pressure and effective stress change correlate to areas of shear seismic change and the model has also quantified the magnitude of these changes.
- Implementing time-lapse slow shear (S22) impedance changes will allow the production company to avoid already depleting/depleted areas and to place completions in channels that are not already producing
- Varying levels of pressure and effective stress change at different depths will create far field areas of lowered pressure and minimum horizontal stress; this will make zonal isolation more important to avoid zonal fracturing of virgin and depleted zones together.
- Sensitivity analysis allows future models to be more precise and will also permit calculation of seismic time shifts with stress change, due to more accurate modeling.

- Time-lapse surveys need to be planned during times of active production drilling. The pressure drop and effective stress change that occurs in the first-year to two years of a wells production is critical in discerning flow pathways.
- Minimum horizontal effective stress changes show propagation of drainage ‘ellipse’ into the far field; this has implications for well placement and completion decisions near long producing wells.
- Changes in horizontal effective stresses show that long producing wells such as RU-1 has the potential for re-fracture re-orientations for enhanced gas recovery.
- Model sensitivity analysis shows that Young’s modulus and associated flow properties have a large impact on the location of pressure and therefore effective stress change.

CHAPTER 6

RECOMMENDATIONS AND FUTURE WORK

6.1 Introduction

Mechanical modeling is well suited for showing pressure and stress changes caused by production can correlate to a seismic response. This correlation is done through quantifying pressure and stress changes in the time intervals of time-lapse seismic monitoring. In addition to this, it gives us insight into how stresses react over long and short periods of production, how these stress magnitudes and orientations may affect re-fracturing, and just how far depletion can extend in this hard rock environment. This model has given us the tools necessary to show that time-lapse nine component seismic is capable of making operation of this field more cost effective. This is accomplished by using time-lapse seismic to make better decisions regarding completions and also for well placement.

6.2 Recommendations

Production modeling has shown that within the model, geomechanics has an impact on production in the field's future (fig. 6.1). Also, the drilling of new wells and completions of those wells can be made more efficient by using time lapse seismic to avoid depleted areas, and restructuring zonal fracture jobs to avoid depleted zones (fig. 5.36-5.38). This also means more effective perforation placement to tap into and fracture virgin zones more effectively. The 3-dimensional modeling completed here has shown that depletion can reach over 900 ft. from the wellbore with magnitudes of ~1800 psi of pressure depletion and lowered minimum horizontal stresses that cause lower fracture gradients.

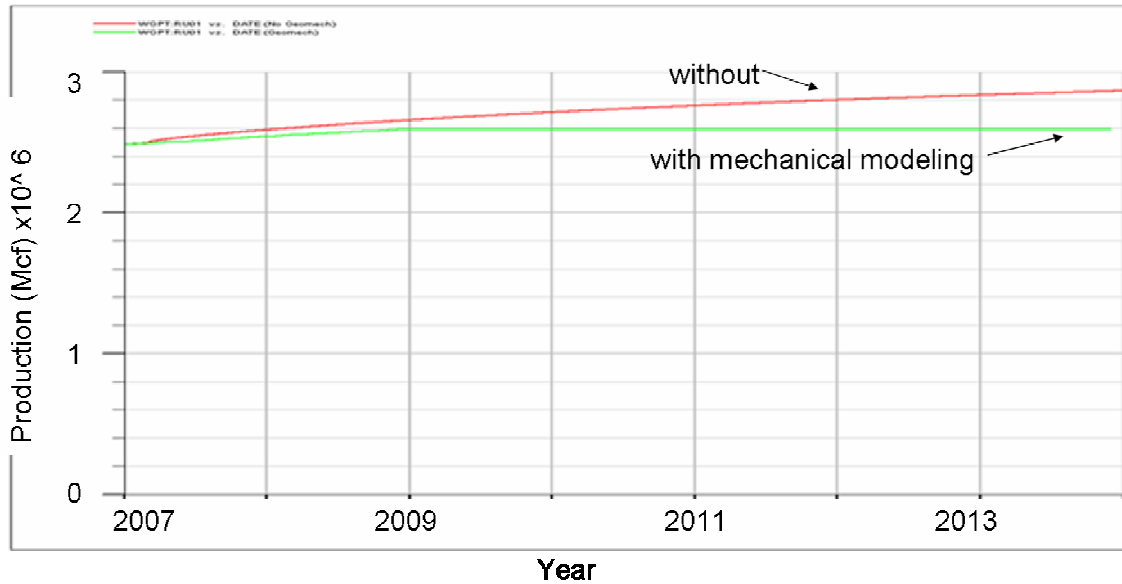


Figure 6.1: Model production response over time with two scenarios. Red line indicates production without considering geomechanics. While green line shows production with mechanical change over time. Courtesy Schlumberger DCS Denver.

It is recommended that the time lapse seismic and future modeling that is being completed in the RCP be used to help avoid already producing zones and to produce more bypassed and untapped pay.

The economic impact of these conclusions is large. If it is possible to save one, two, or possibly three fracturing stages within just one well, we have justified the expense of one seismic survey. If we can apply it to many wells, then we have not only justified the expense of multi-component seismic work, but have started to save the production company from unnecessary stimulation expenses, which over time can be quite substantial.

6.2 Future Work

The future of this work depends on creating more realistic geologic model through the integration of better statistical algorithms. This work is being done in conjunction with using time-lapse slow shear seismic as a soft constraint for new geo-

statistical models (Casey, personal communication). This will allow more realistic geologic models to be created with appropriate channels from depletion seen in time-lapse seismic. Once this is completed, the production modeling to geomechanical modeling can be performed, which will produce a better (i.e. more geologically realistic) model. This will entail building a new geostatistical model from the 2003-2006 seismic data, and then rerunning the workflow with a new history match.

From this iterative process we can make this field more economic to produce through time.

“All models are wrong, but some are useful.”

--David Johnston

REFERENCES

- Barree, R. D., Barree, V. L., Craig, D. P., 2007. Holistic Fracture Diagnostics. Society of Petroleum Engineers Rocky Mountain Oil & Gas Technology Symposium, Denver, CO. April 16-18 2007. SPE #107877.
- Bratton, T., 2007. Personal Communication.
- Casey, M., 2007. PhD Dissertation. In progress.
- Casey, M., 2007. Personal Communication.
- Casey, M., 2006. "Geo-cellular modeling of Rulison Field". Reservoir Characterization Project Fall 2006 Meeting Report. Ed. Tom Davis. 6 pgs.
- Cole, R., and Cumella, S.P., 2003, Field Trip Guidebook Stratigraphic Architecture and Reservoir Characteristics of the Mesaverde Group, Southern Piceance Basin, Colorado, *in* Peterson, K.M., Terrilyn, M.O., and Anderson, D.S., eds., Piceance Basin 2003 Guidebook: Denver, CO, Rocky Mountain Association of Geologists, p. 385-443.
- Colorado Interstate Gas. (2006). "Piceance Basin Expansion Project." Retrieved 2/4/2008, from www.cigco.com/piceance.asp.
- Cumella, S., and Ostby, D., 2003. Geology of the Basin-Centered Gas Accumulation, Piceance Basin, Colorado. Rocky Mountain Association of Geologists, 2003 Piceance Basin Guidebook.
- Fjaer, E., Holt R.M., Horstrud, P., Raaen, A.M., and Risnes, R., 1992. Petroleum Related Rock Mechanics. Amsterdam, Elsevier. Developments in Petroleum Science 33.
- Guyliev, E., 2007. Vp/Vs estimation from multicomponent seismic data for improved characterization of a tight sandstone gas reservoir, Rulison Field, Colorado. Masters Thesis. Geophysics. Golden, Colorado School of Mines.
- Hettema, M.H.H., et. al., 1998. Production-Induced Compaction of Sandstone Reservoirs: The Strong Influence of Field Stress. Society of Petroleum Engineers. SPE 50630.
- Higgins, S., 2006. Geomechanical modeling as a reservoir characterization tool at Rulison field, Piceance Basin, Colorado. Masters Thesis. Geophysics. Golden, Colorado School of Mines.
- Hofmann, R., Xu, X., Batzle, M., Prasad, M., Furre, A-K., and Pillitteri, A., 2005. "Effective Pressure or What is the Effect of Pressure?" The Leading Edge. Society of Exploration Geophysicists. December 2005. 1256-1260.

- Jaeger, J.C., Cook, N.G.W., Zimmerman, R.W. 2007. Fundamentals of Rock Mechanics. Blackwell Publishing. John Wiley and Sons, Inc., New York. 4th Edition.
- Jansen, K., 2005. Seismic Investigation of Wrench Faulting and Fracturing at Rulison Field, Colorado. Masters Thesis. Geophysics. Golden, Colorado School of Mines.
- Johnson, R. C. and Nuccio, V.F., 1986. Structural and Thermal History of the Piceance Creek Basin, Western Colorado, in Relation to Hydrocarbon Occurrence in the Mesaverde Group. AAPG Studies in Geology 73: 165-205.
- Koutsabeloulis, N.C., Heffer, K.J., and Wong, S., 1994. Numerical geomechanics in reservoir engineering. *Computer Methods and Advances in Geomechanics*, Siriwardane and Zaman eds., Balkema, Rotterdam.
- Koutsabeloulis, N. C., and Hope, S. A., 1998. Coupled stress/fluid thermal multi-phase reservoir simulation studies incorporating rock mechanics: Society of Petroleum Engineers, SPE Paper 47393, 6 p.
- Keighley, D., 2006. P-wave time-lapse seismic data interpretation at Rulison field, Piceance Basin, Colorado. Masters Thesis. Geophysics. Golden, Colorado School of Mines.
- Kusuma, M., 2005. Analysis of time-lapse P-wave seismic data from Rulison Field, Colorado. Masters Thesis. Geophysics. Golden, Colorado School of Mines.
- Kuuskra, V. A. and J. Ammer (2004). "Tight Gas Sands Development - How to Dramatically Improve Recovery Efficiency." GasTIPS 10(1): 5.
- Jansen, K. J., 2005. Seismic investigation of wrench faulting and fracturing at Rulison field, Colorado. Masters Thesis. Geophysics. Golden, Colorado School of Mines.
- Lin, G.R. and Quek, S.S. 2003. Finite Element Method: A Practical Course. Oxford Publishing. 384 pgs.
- Lorenz, J. C., 1985. Tectonic and Stress Histories of the Piceance Creek Basin and the MWX Site, from 75 Million Years ago to the Present. Springfield, VA, Sandia Report SAND84-2306, National Technical Information Service.
- Lorenz, J. C. and Finley, S.J., 1991. Regional Fractures II: Fracturing of Mesaverde Reservoirs in the Piceance Basin, Colorado. November 1991. The American Association of Petroleum Geologists 75 (11): 1738-1757.
- Lorenz, J. C., Sattler A.R., and Stein, C.L., 1989. The Effects of Depositional Environment on Petrophysical Properties of Mesaverde Reservoirs, Northwestern, CO. Society of Petroleum Engineers, SPE Paper 19583.

- Martin, M. A., and Davis, T. L., 1987. Shear-wave birefringence: A new tool for evaluating fractured reservoirs: THE LEADING EDGE., Vol. 6., No. 10., p. 22-28.
- Mattax, C.C., and Dalton, R.L., 1990, Reservoir Simulation Monograph, Vol. 13, SPE Monograph Series.
- McFall, K.S., Wicks, D.E., Kruuskraa, V.A., and Sedwick, K.B. 1986. A geologic assessment of natural gas from coal seams in the Piceance Basin, Colorado. Gas Research Institute, Topical Report. GRI-87/0060 (September 1985-September 1986), 76 p.
- Meza, R., 2007. Master's Thesis. In Progress.
- Meza, R. 2007. Personal Communication.
- Onaisi, A., Samier, P., Koutsabeloulis, N., Longuemare, P., 2002. Management of Stress Sensitive Reservoirs Using Two Coupled Stress-Reservoir Simulation Tools: ECL2VIS and ATH2VIS: Society of Petroleum Engineers, SPE Paper 78512, 13p.
- Riley, R.B., 2007. Combined micro-macro seismic monitoring of a hydraulic fracture stimulation, Rulison field, Colorado. Masters Thesis. Geophysics. Golden, Colorado School of Mines.
- Rojas, E. 2005. Elastic rock properties of tight gas sandstones for reservoir characterization at Rulison Field, Colorado. Masters Thesis. Geophysics. Golden, Colorado School of Mines.
- Rumon, M., 2006. Shearwave time-lapse monitoring of a tight gas reservoir, Rulison Field, Colorado. Masters Thesis. Geophysics. Golden, Colorado School of Mines.
- Sattler, A. R., 1991. Multiwell Experiment Core Analyses - An Overview of the Core Analysis of a Low-Permeability Sandstone Reservoir. The Log Analyst. September-October, 1991: 498-510.
- Thiercelin, M.J. and Plumb, R.A. Core-Based Prediction of Lithologic Stress Contrasts in East Texas Formations. SPE Formation Evaluation. December 1994. Original Paper in 1992 SPE 21847.
- Thomsen, L. 2002. Understanding seismic anisotropy in exploration and exploitation. Society of Exploration Geophysicists.
- Tremain, Carol M. and Tyler, R. 1997. Cleat, fracture, and stress patterns in the Piceance Basin, Colorado: Controls on coalbed methane producibility. Rocky Mountain Association of Geologists, Fractured Reservoirs: Characterizations and Modeling Guidebook.

- Vasconcelos, I. and Grechka, V., 2007. Seismic Characterization of Multiple Fracture Sets at Rulison Field, Colorado. *Geophysics*. vol. 72. no. 2. p B19-B30.
- Verbeek, E.R. and Grout, M.A., 1997. Relation Between Basement Structures and Fracture Systems in Cover Rocks, Northeastern and Southwestern Colorado Plateau, Series Title: Laccolith Complexes of Southeastern Utah. Publisher: Friedman, Jules, D. Huffman, A Curtis., USGS Ability 2158.
- Visage and VisGen reference manuals. 2007. Courtesy of Schlumberger Technology Corporation.
- Warpinski, N. R., 1989. Elastic and Viscoelastic Calculations of Stresses in Sedimentary Basins. *SPE Formation Evaluation*. December 1989. Original Paper in 1986, SPE # 15243.
- Warpinski, N. R., Branagan, P., and Wilmer, R., 1985. In-Situ Stress Measurements at U.S. DOE's Multiwell Experiment Site, Mesaverde Group, Rifle, Colorado. *Journal of Petroleum Technology*. March 1989: 527-536.
- Warpinski, N. R., Peterson, R.E., Branagan, P.T., Engler, B.P., and Wolhart, S.L., 1998. In Situ Stress and Moduli: Comparison of Values Derived from Multiple Techniques. *Society of Petroleum Engineers Annual Technical Conference and Exhibition*, New Orleans, Louisiana. September 27-30, 1998. SPE # 49190.
- Warpinski, N. R. and Teufel, L.W., 1989. In-Situ Stresses in Low-Permeability, Nonmarine Rocks. *Journal of Petroleum Technology*. April 1989: 405-414.
- Wolhart, S. L., C. E. Odegard, et al. (2005). "Microseismic Fracture Mapping Optimizes Development of Low-Permeability Sands of the Williams Fork Formation in the Piceance-Basin." *SPE International*: 13.

APPENDIX A

This appendix contains map view slices of intervals at depth. Minimum and maximum horizontal effective stress changes are shown as well effective overburden stress change (only shown once as maximum horizontal stress direction does not effect overburden since we are using principal stresses) compared to those intervals pressure changes from 2003-2006 with the maximum horizontal effective stress direction set at 98 degrees (this is the direction of present day maximum horizontal stress). For representative equations please see Ch. 4 or 5.

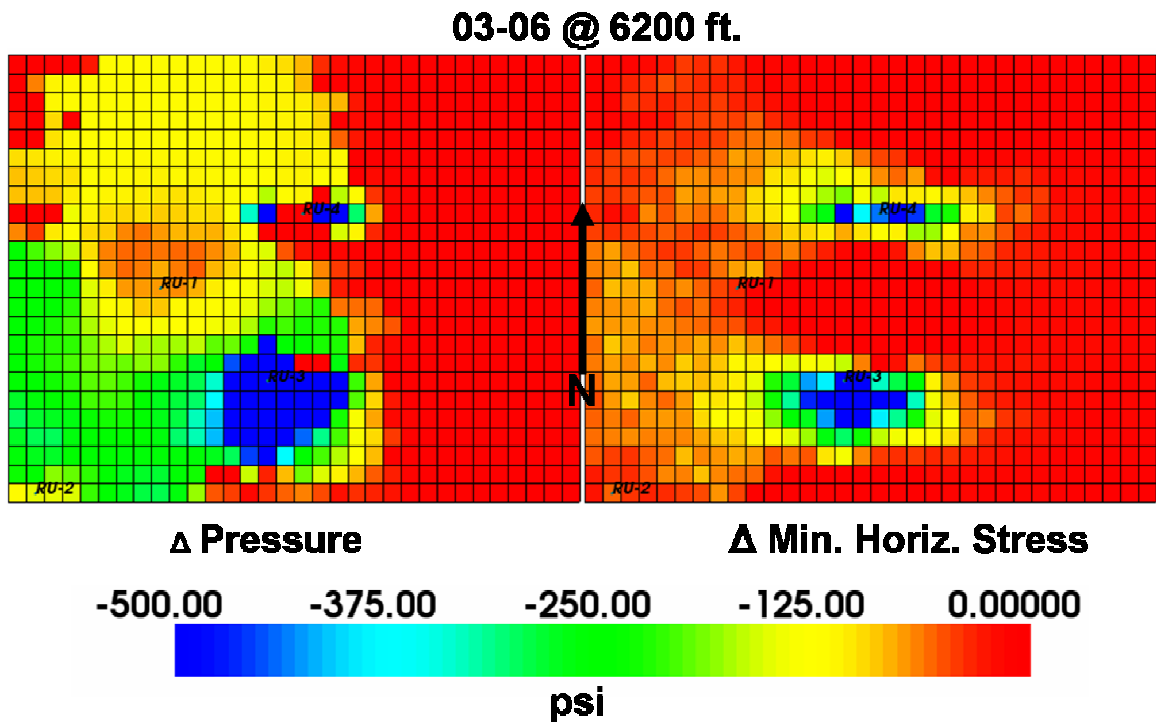


Figure A.1: Pressure compared to minimum horizontal effective stress change for 2003-2006 at 6200 ft. depth. Note direction of effective stress change.

03-06 @ 6200 ft.

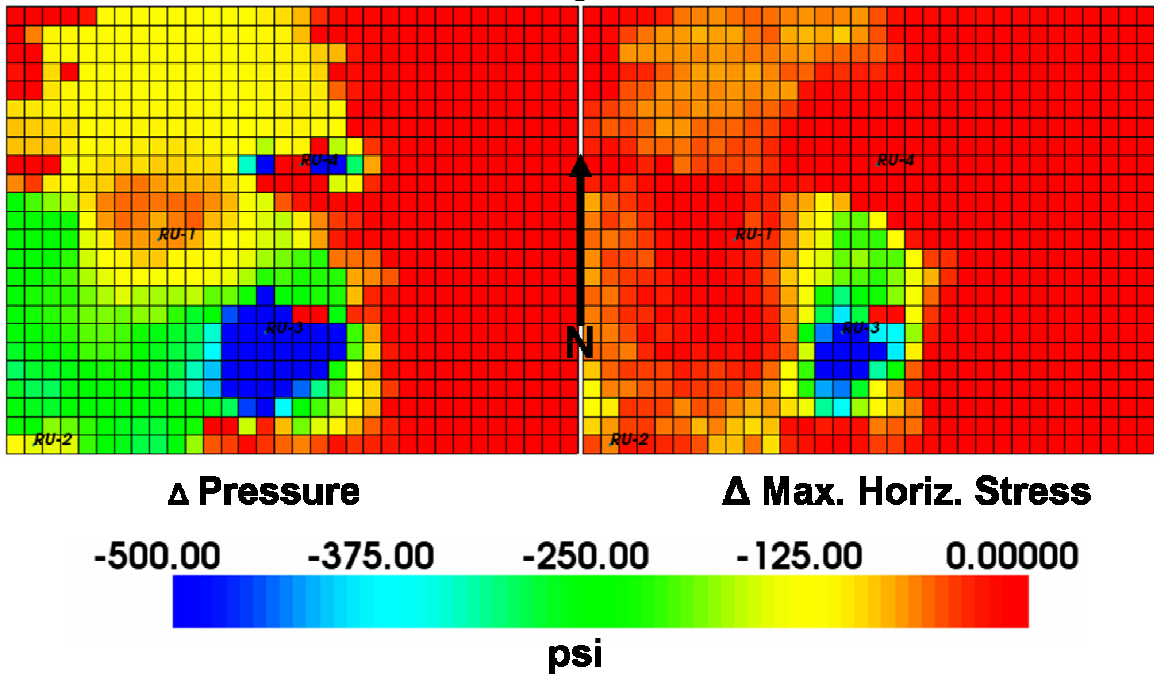


Figure A.2: Pressure compared to maximum horizontal effective stress change for 2003-2006 at 6200 ft. depth. Note direction is perpendicular to minimum horizontal effective stress change.

03-06 @ 6500 ft.

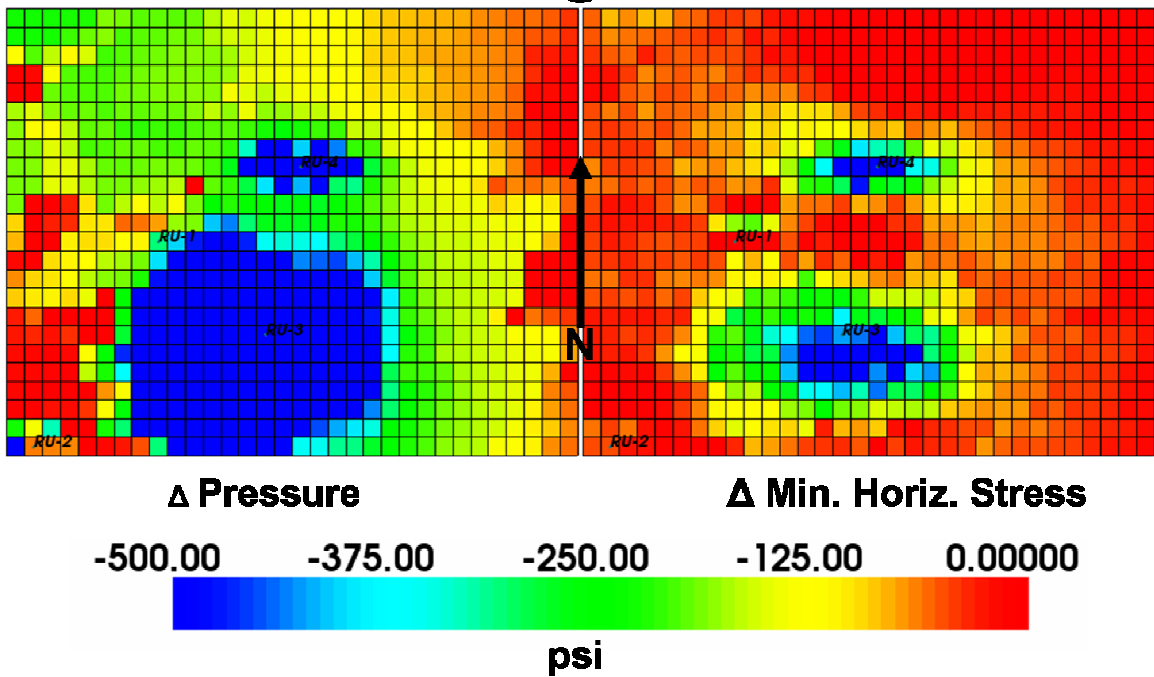


Figure A.3: Pressure compared to minimum horizontal effective stress change for 2003-2006 at 6500 ft. depth. Note direction of effective stress change.

03-06 @ 6500 ft.

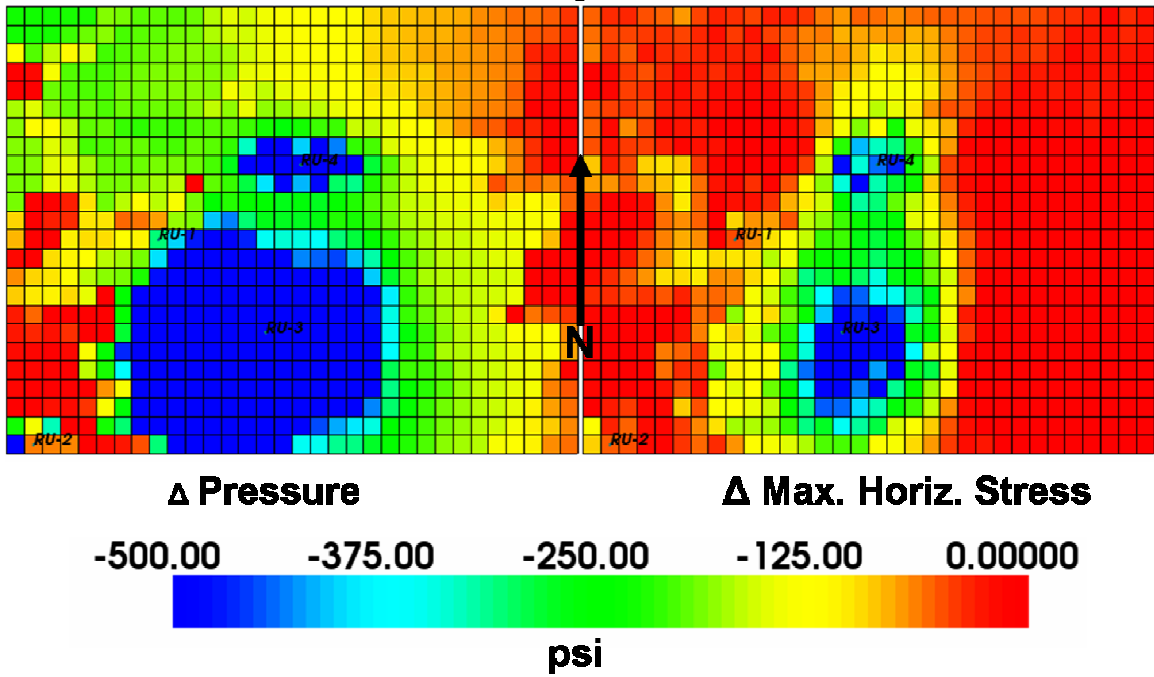


Figure A.4: Pressure compared to maximum horizontal effective stress change for 2003-2006 at 6500 ft. depth. Note direction is perpendicular to minimum horizontal effective stress change.

Shown below are the minimum, maximum, and overburden effective stress changes only in these instances they are using the shear wave seismic rotation direction of N45W or 135 degrees east of north.

03-06 @ 6200 ft.

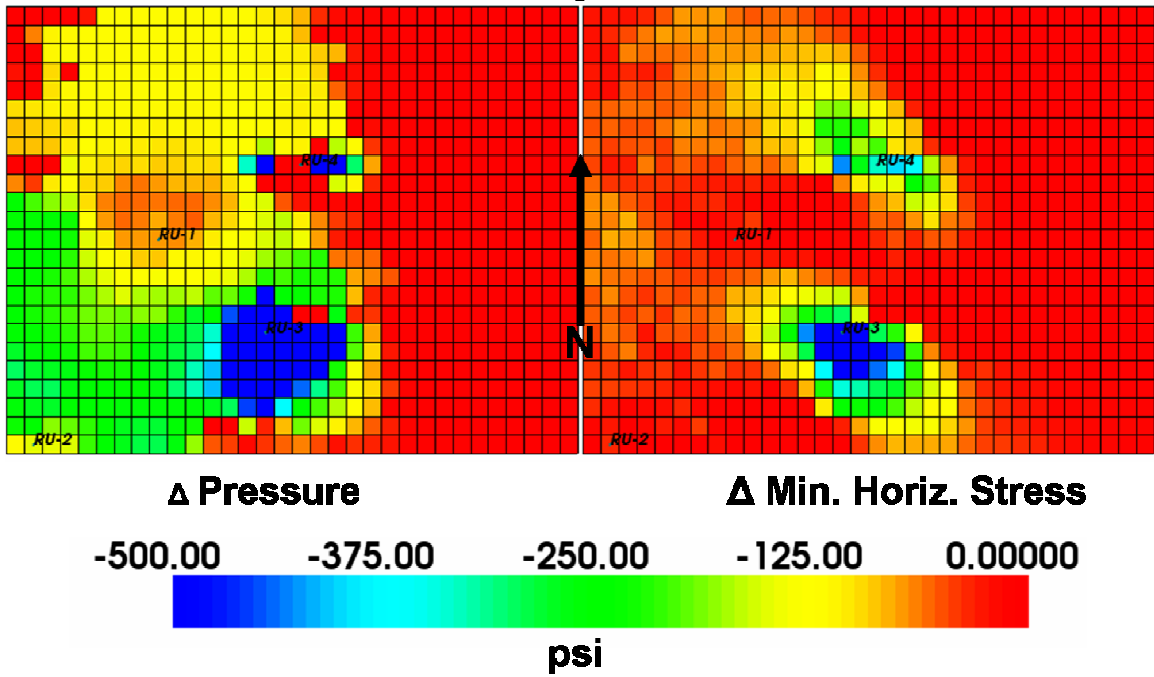


Figure A.5: Pressure compared to minimum horizontal effective stress change for 2003-2006 at 6200 ft. depth. Note direction of stress change.

03-06 @ 6200 ft.

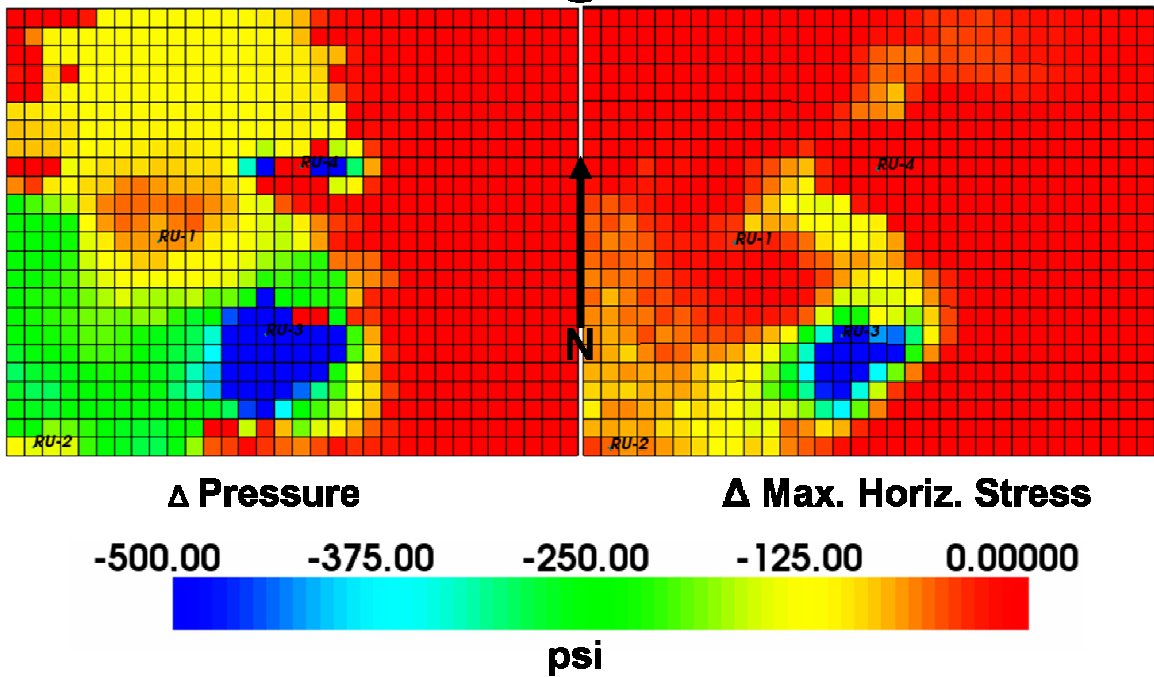


Figure A.6: Pressure compared to maximum horizontal effective stress change for 2003-2006 at 6200 ft. depth. Note direction is perpendicular to minimum horizontal effective stress change.

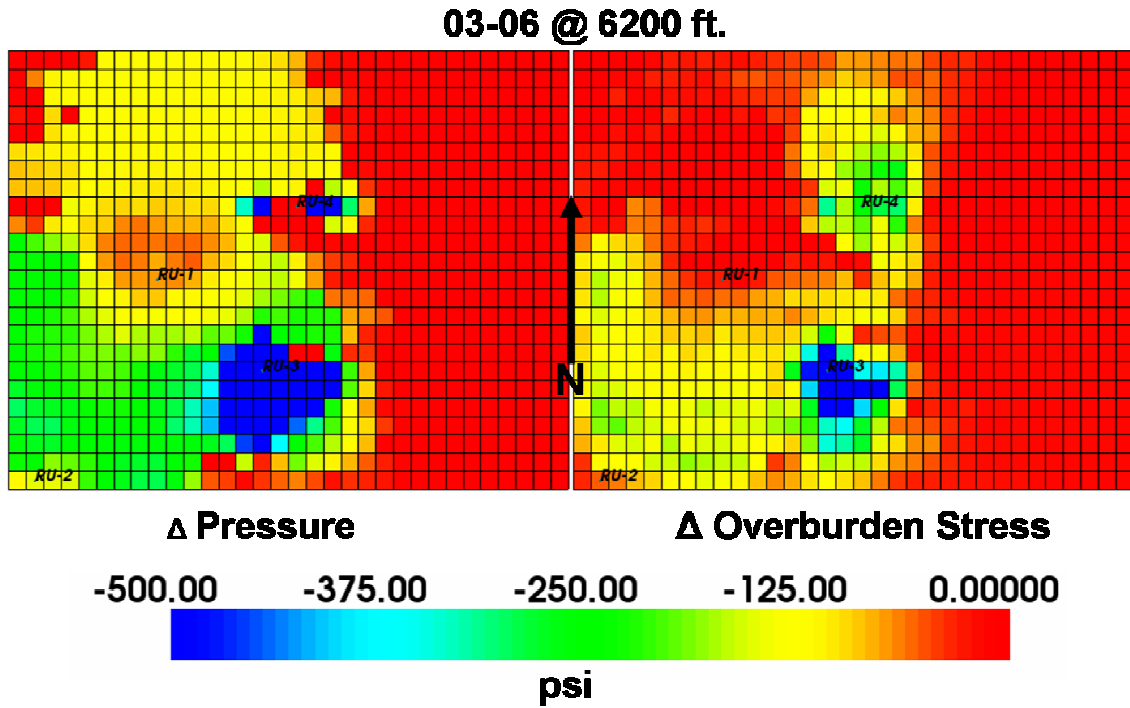


Figure A.7: Pressure compared to overburden effective stress change for 2003-2006 at 6200 ft. depth.

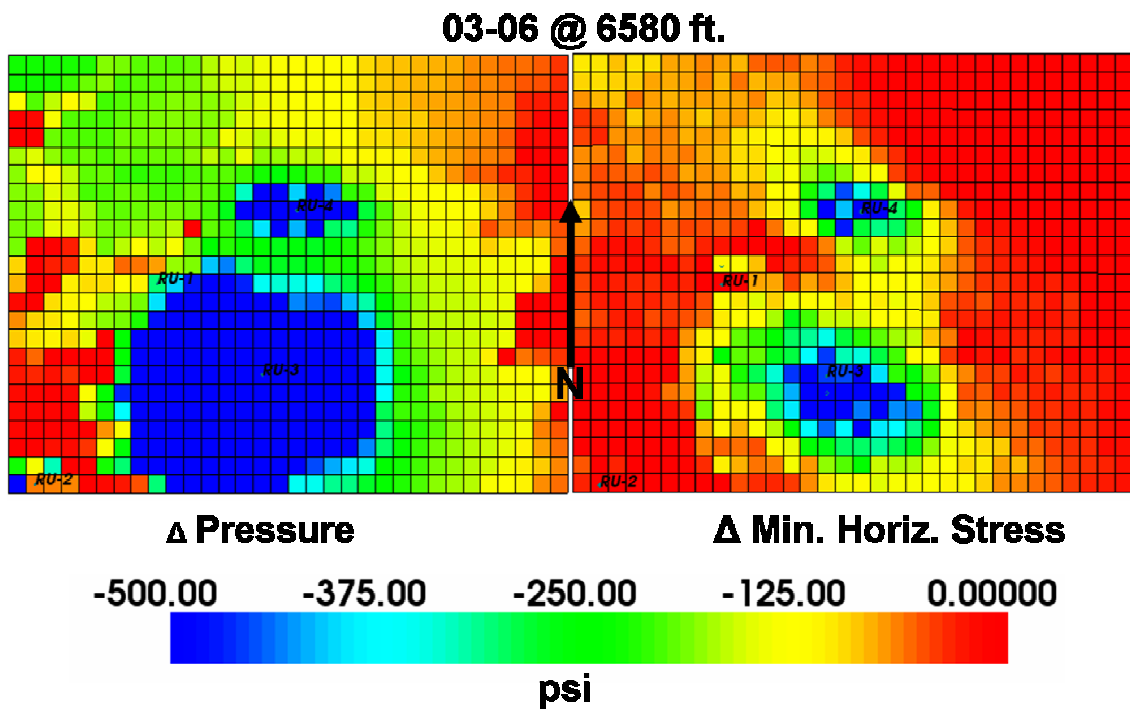


Figure A.8: Pressure compared to minimum horizontal effective stress change for 2003-2006 at 6580 ft. depth. Note direction of effective stress change.

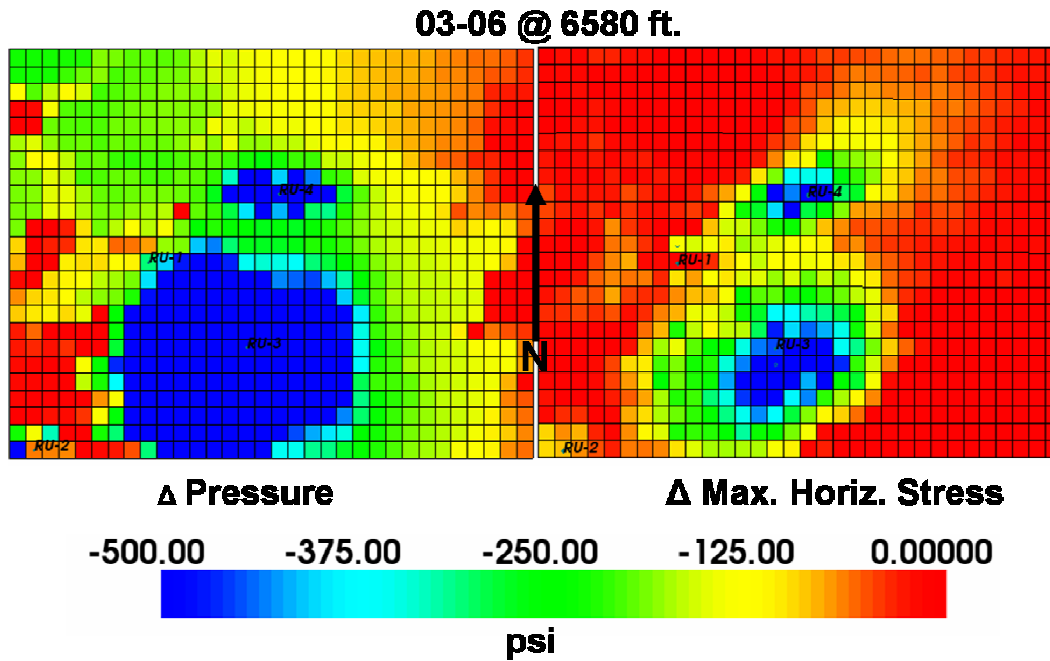


Figure A.9: Pressure compared to maximum horizontal effective stress change for 2003-2006 at 6580 ft. depth. Note direction is perpendicular to minimum horizontal effective stress change.

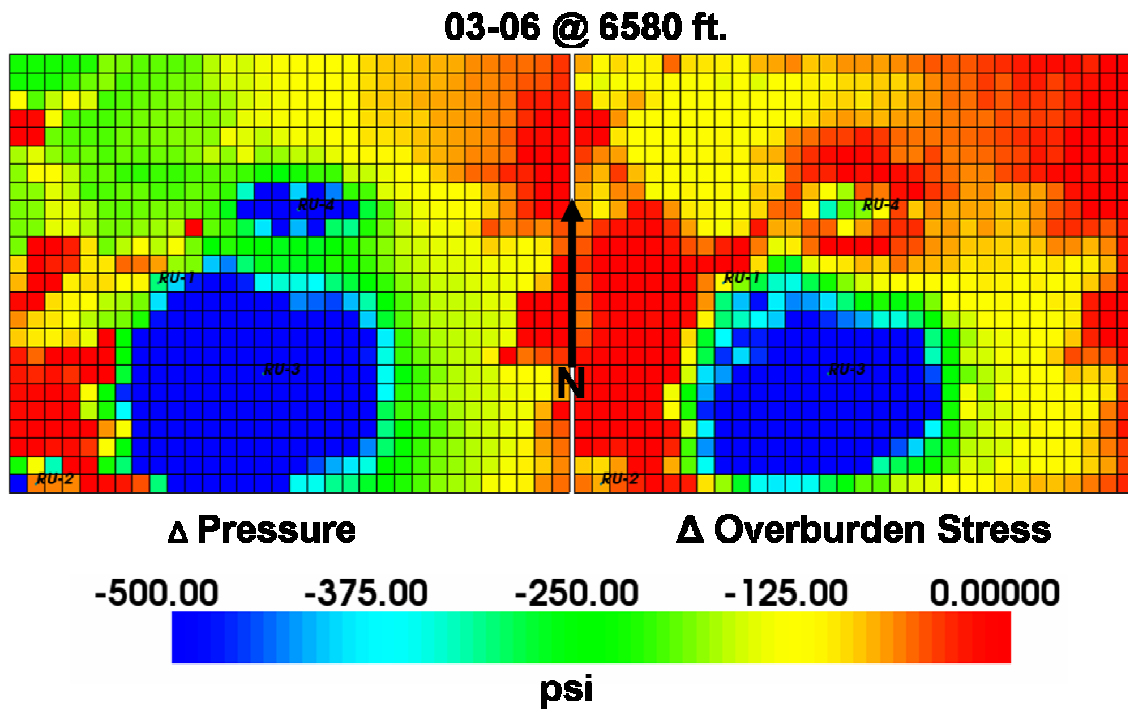


Figure A.10: Pressure compared to overburden effective stress change for 2003-2006 at 6580 ft. depth.

APPENDIX B

This appendix contains the 2003-2004 model compared to 2003-2004 time-lapse seismic results. The black cross in the seismic represents well RU-1 in the model while the green cross represents RU-2 in the model for 2003-2004.

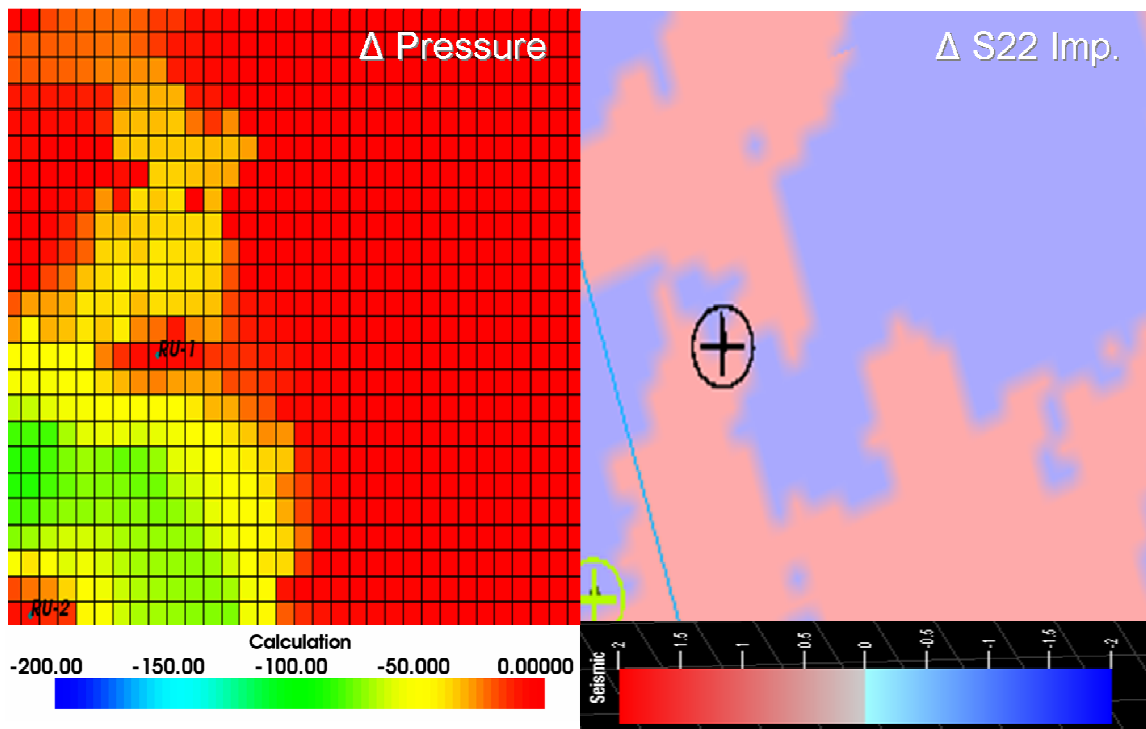


Figure B.1: Pressure change compared to S22 impedance change from 2003-2004 at 5900 ft. depth. Note low percentage changes in seismic data (~2%). Seismic is from Rumon, 2006.

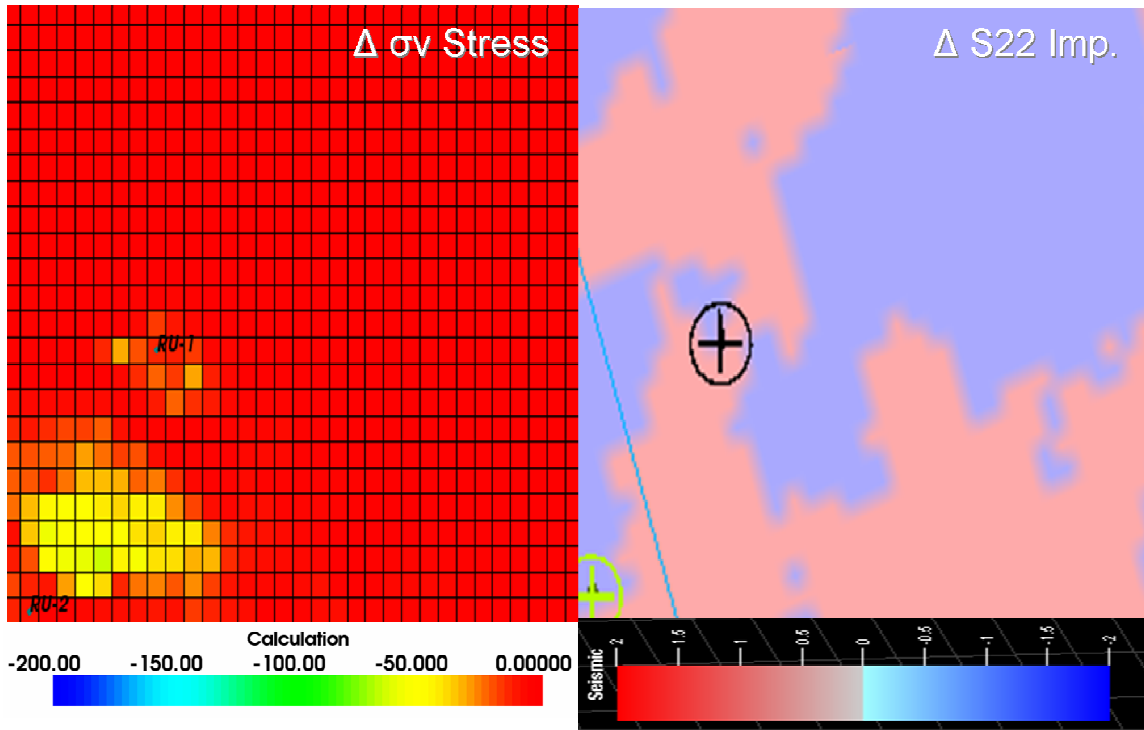


Figure B.2: Overburden stress change compared to S22 seismic impedance change from 2003-2004 at 5900 ft. depth. Seismic is from Rumon, 2006.

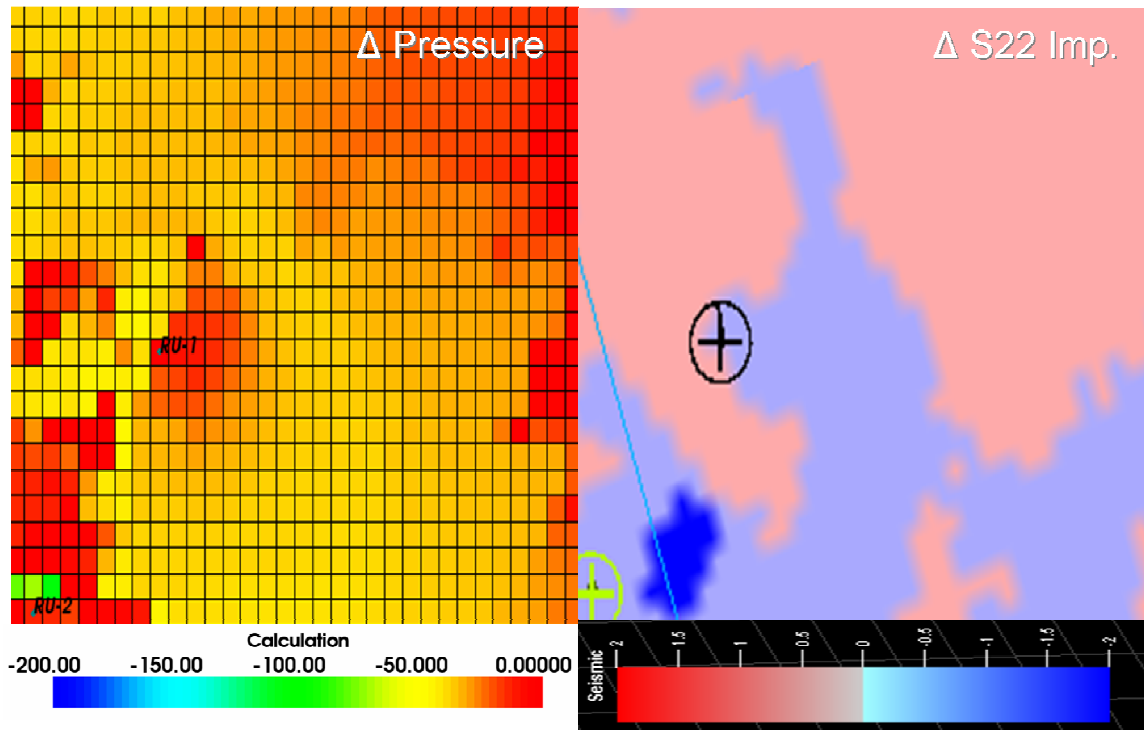


Figure B.3: Pressure change compared to S22 seismic impedance change from 2003-2004 at 6580 ft. depth. Seismic is from Rumon, 2006.

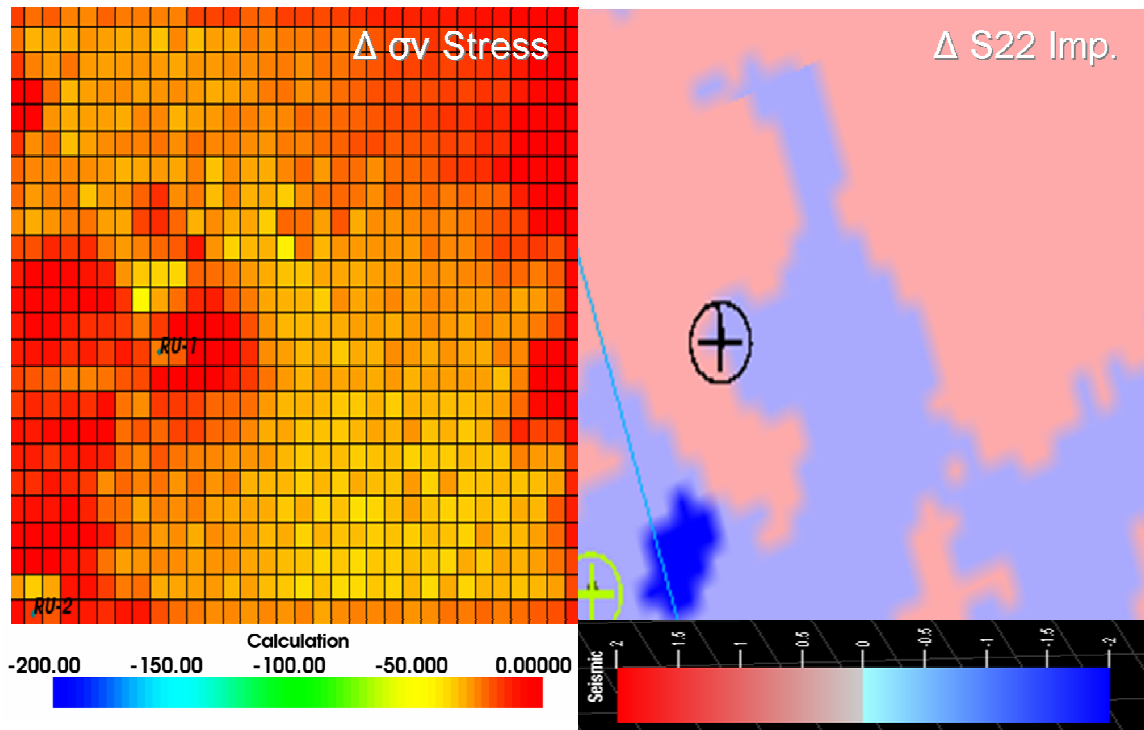


Figure B.4: Overburden stress change compared to S22 seismic impedance change from 2003-2004 at 6580 ft. depth. Seismic is from Rumon, 2006.